



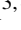
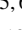

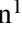




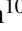







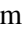
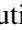

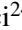








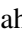
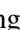


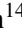
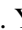


# Eruptive mass-loss less than a year before the explosion of superluminous supernovae

## I. The cases of SN 2020xga and SN 2022xgc

A. Gkini<sup>1</sup> , C. Fransson<sup>1</sup> , R. Lunnan<sup>1</sup> , S. Schulze<sup>2</sup> , F. Poidevin<sup>3,4</sup> , N. Sarin<sup>5,6</sup> , R. Könyves-Tóth<sup>7,8</sup> , J. Sollerman<sup>1</sup> , C. M. B. Omand<sup>9</sup> , S. J. Brennan<sup>1</sup> , K. R. Hinds<sup>9</sup> , J. P. Anderson<sup>10,11</sup> , M. Bronikowski<sup>12</sup> , T.-W. Chen<sup>13</sup> , R. Dekany<sup>14</sup> , M. Fraser<sup>15</sup> , C. Fremling<sup>14,16</sup> , L. Galbany<sup>17,18</sup> , A. Gal-Yam<sup>19</sup> , A. Gangopadhyay<sup>1</sup> , S. Geier<sup>3,20</sup> , E. P. Gonzalez<sup>21,22</sup> , M. Gromadzki<sup>23</sup> , S. L. Groom<sup>24</sup> , C. P. Gutiérrez<sup>18,17</sup> , D. Hiramatsu<sup>25,26</sup> , D. A. Howell<sup>21,22</sup> , Y. Hu<sup>1</sup> , C. Inserra<sup>27</sup> , M. Kopsacheili<sup>17,18</sup> , L. Lacroix<sup>28,6</sup> , F. J. Masci<sup>24</sup> , K. Matilainen<sup>29</sup> , C. McCully<sup>21</sup> , T. Moore<sup>10,30</sup> , T. E. Müller-Bravo<sup>17,18</sup> , M. Nicholl<sup>30</sup> , C. Pellegrino<sup>21,22</sup> , I. Pérez-Fournon<sup>3,4</sup> , D. A. Perley<sup>9</sup> , P. J. Pessi<sup>1</sup> , T. Petrushevskaya<sup>12</sup> , G. Pignata<sup>31</sup> , F. Ragosta<sup>32,33</sup> , A. Sahu<sup>34</sup> , A. Singh<sup>1</sup> , S. Srivastav<sup>35</sup> , J. L. Wise<sup>9</sup> , L. Yan<sup>14</sup> , and D. R. Young<sup>30</sup> 

(Affiliations can be found after the references)

### ABSTRACT

We present photometric and spectroscopic observations of SN 2020xga and SN 2022xgc, two hydrogen-poor superluminous supernovae (SLSNe-I) at  $z = 0.4296$  and  $z = 0.3103$  respectively, that show an additional set of broad Mg II absorption lines, blueshifted by a few thousands  $\text{km s}^{-1}$  with respect to the host galaxy absorption system. Previous work interpreted this as due to resonance line scattering of the SLSN continuum by rapidly expanding CSM expelled shortly before the explosion. The peak rest-frame  $g$ -band magnitude of SN 2020xga is  $-22.30 \pm 0.04$  mag and of SN 2022xgc is  $-21.97 \pm 0.05$  mag, placing them among the brightest SLSNe-I. We use high-quality spectra from ultraviolet to near-infrared wavelengths to model the Mg II line profiles and infer the properties of the CSM shells. We find that the CSM shell of SN 2020xga resides at  $\sim 1.3 \times 10^{16}$  cm moving with a maximum velocity of  $4275 \text{ km s}^{-1}$ , and the shell of SN 2022xgc is located at  $\sim 0.8 \times 10^{16}$  cm reaching up to  $4400 \text{ km s}^{-1}$ . These shells were expelled  $\sim 11$  and  $\sim 5$  months before explosion for SN 2020xga and SN 2022xgc respectively, possibly as a result of Luminous Blue Variable-like eruptions or pulsational pair instability (PPI) mass loss. We also analyze optical photometric data and model the light curves considering powering from the magnetar spin-down mechanism. The results support very energetic magnetars, approaching the mass-shedding limit, powering these SNe with ejecta masses of  $\sim 7 - 9 M_{\odot}$ . The ejecta masses inferred from the magnetar modeling are not consistent with the PPI scenario pointing towards stars  $> 50 M_{\odot}$  He-core, hence alternative scenarios such as fallback accretion are discussed. Modeling the spectral energy distribution of the host galaxy of SN 2020xga reveals a host mass of  $10^{7.8} M_{\odot}$ , a star formation rate of  $0.96_{-0.26}^{+0.47} M_{\odot} \text{ yr}^{-1}$ , and a metallicity of  $\sim 0.2 Z_{\odot}$ .

**Key words.** supernovae: general – supernovae: individual: SN 2020xga, SN 2022xgc

## 1. Introduction

Superluminous supernovae (SLSNe; Quimby et al. 2011; Gal-Yam 2012) constitute a rare class of massive star explosions (Perley et al. 2020) that reach absolute magnitudes between  $-20$  and  $-23$  mag at peak (De Cia et al. 2018; Lunnan et al. 2018a; Chen et al. 2023a). Today more than 200<sup>1</sup> SLSNe have been detected out to  $z = 2$  (Angus et al. 2019) and are frequently found in low-metallicity dwarf host galaxies with specific high star-formation rates (Neill et al. 2011; Chen et al. 2013; Lunnan et al. 2014; Leloudas et al. 2015; Angus et al. 2016; Perley et al. 2016; Chen et al. 2017; Schulze et al. 2018; Taggart & Perley 2021).

There are two types of SLSNe, which are distinguished by the presence or absence of hydrogen in their spectra (Gal-Yam 2012): hydrogen poor (Type I; SLSNe-I hereafter) and hydrogen rich (Type II; SLSNe-II hereafter). The early spectra of the majority of SLSNe-I could show a prominent blue continuum and a series of O II features at  $3500 - 5000 \text{ \AA}$  with the feature at  $4350 - 4650 \text{ \AA}$  being the most dominant (Quimby et al. 2011;

Mazzali et al. 2016; Quimby et al. 2018). Studies (Mazzali et al. 2016; Dessart 2019; Könyves-Tóth 2022; Saito et al. 2024) have shown that the O II features require either non-thermal excitation and/or temperatures higher than  $12\,000 - 14\,000 \text{ K}$ ; but in a few SLSNe-I (Nicholl et al. 2014; Gutiérrez et al. 2022; Schulze et al. 2024) this feature has not been detected in their spectra.

The high luminosities observed in SLSNe-I cannot be explained by the amount of radioactive  $^{56}\text{Ni}$  generated in the normal core-collapse process, which is the major power source of Type I SNe and thus, alternative scenarios have been proposed. A popular scenario which could potentially explain the majority of the observed properties in SLSNe-I (e.g., Inserra et al. 2013; Nicholl et al. 2017; Liu et al. 2017; Blanchard et al. 2020; Hsu et al. 2021; Chen et al. 2023b) is the spin-down of a newly formed rapidly rotating highly magnetised neutron star (NS) known as a magnetar (Ostriker & Gunn 1971; Kasen & Bildsten 2010; Woosley 2010; Vurm & Metzger 2021). Other proposed scenarios are the long-term fallback accretion of material onto a black hole (Dexter & Kasen 2013; Moriya et al. 2018), the thermonuclear explosion of  $140 - 260 M_{\odot}$  zero-age main sequence (ZAMS) metal-poor stars referred to as pair-instability

<sup>1</sup> reported in Transient Name Server

supernovae (PISNe; Barkat et al. 1967; Rakavy & Shaviv 1967; Woosley et al. 2002; Heger & Woosley 2002) and interaction of the SN ejecta with circumstellar material (CSM) formed by previously expelled material from the star (Chatzopoulos et al. 2012; Sorokina et al. 2016; Wheeler et al. 2017; Chen et al. 2023b).

The fate of the stars, their powering mechanism as well as the type of the resulting explosion are closely related to the final years of the stellar lives before the core-collapse. During their lifetime, stars can lose a substantial part of their initial mass due to stellar winds (e.g., Lucy & Solomon 1970; Lamers et al. 1999; Puls et al. 2008), binary interactions (e.g., Petrovic et al. 2005; Götzberg et al. 2017; Yoon et al. 2017; Petrović 2020; Laplace et al. 2020) or eruptive mass loss (e.g., Heger & Woosley 2002; Woosley et al. 2007; Smith & Arnett 2014; Woosley 2017; Fuller & Ro 2018; Leung et al. 2019; Renzo et al. 2020; Leung et al. 2021). Mass loss in the form of violent outbursts becomes critical at the late stages of the stellar evolution and, in extreme situations, may remove tens of solar masses. Such eruptive mass loss has been observed in  $\eta$  Carinae (Westphal & Neugebauer 1969) and it is thought to come from a group of post-main sequence stars called Luminous Blue Variables (LBV; Humphreys 1999).

Eruptive mass loss can also be achieved in the case of pulsational pair instability (PPI; Woosley et al. 2007; Woosley 2017; Leung et al. 2019) in which the formation of positron–electron pairs in the CO core of a  $75 - 140 M_{\odot}$  ZAMS metal-poor star results in explosive O-burning, and the energy released drives a series of mass ejections. The more massive the star is, the more energetic the pulses are and thus more mass will be ejected in the pulses (Renzo et al. 2020). Woosley (2017) and Renzo et al. (2020) note that the time interval between the mass ejection and the core collapse in PPI could be between a few hours to 10 000 years which along with the ejection velocity could determine the distance of the ejected material.

Eruptive mass loss, and especially PPI, can generate CSM shell(s) around the progenitor stars which potentially can be seen in the spectra of the SNe. There are a few SLSNe-I in the literature with evidence of late-time mass loss by showing late-time broad H emission (Yan et al. 2015, 2017a; Fiore et al. 2021; Purisainen et al. 2022; Gkini et al. 2024) or early forbidden emission of [O II] and [O III] (Lunnan et al. 2016; Inserra et al. 2017; Aamer et al. 2024; Schulze et al. 2024) in their spectra. This former has been explained by interaction of the ejecta with H-rich CSM located at  $\sim 10^{15} - 10^{16}$  cm (e.g., Yan et al. 2015), while the latter by the interaction with low-density matter moving at a few  $10^3$  km s $^{-1}$ . However, recently, two SLSNe-I, iPTF16eh (Lunnan et al. 2018b) and SN 2018ibb (Schulze et al. 2024) were discovered that show a unique spectroscopic feature, a second Mg II absorption system blueshifted by  $\sim 3000$  km s $^{-1}$  with respect to the Mg II absorption lines originating in the interstellar medium of the host galaxy. This feature has been associated with the photoionization of a rapidly expanding CSM shell expelled decades before the explosion. In the case of iPTF16eh, Lunnan et al. (2018b) also detected a Mg II emission line which moved from  $-1600$  km s $^{-1}$  to  $2900$  km s $^{-1}$  between 100 and 300 days after maximum light and this was attributed to a light echo from that shell. The CSM was located at  $\sim 10^{17}$  cm and matched with theoretical predictions of shell ejections due to PPI. However, the detection of these shells were both serendipitous, and so it is not known whether these properties are typical, or how common this phenomenon is.

We present results from a dedicated study using the X-shooter spectrograph (Vernet et al. 2011) on the ESO Very Large Telescope (VLT) on Paranal, Chile to search for a second

Mg II absorption system. The full sample will be presented in a follow-up paper; here we focus on the analysis of the two detections found in the X-shooter sample indicating the presence of a fast-moving CSM. An extensive dataset for SN 2020xga and SN 2022xgc enable us to extract the CSM shell properties and give insights into the late stages of the stellar evolution.

This paper is structured as follows. In Sect. 2 we present photometric and spectroscopic data for SN 2020xga and SN 2022xgc along with photometric measurements of their host galaxies, and imaging polarimetry data for SN 2022xgc. In Sect. 3 we analyze the light-curve properties of SN 2020xga and SN 2022xgc, derive their blackbody temperatures and radii, construct bolometric light curves and compare them with a homogeneous sample of SLSNe-I as well as with the photometric properties of SN 2018ibb and iPTF16eh and, model the light curves of SN 2020xga and SN 2022xgc under the assumption that they are powered by a magnetar. In Sect. 4 we present the spectroscopic sequences of SN 2020xga and SN 2022xgc, analyze the spectral properties of these two objects and compare them with those of well-studied SLSNe-I, and with SN 2018ibb and iPTF16eh. The modeling of the Mg II lines to extract information about the CSM shell is done in Sect. 5. In Sect. 6 we discuss the properties of the two host galaxies. We discuss our findings and provide possible mass-loss scenarios in Sect. 7, and summarize our results in Sect. 8.

Throughout the paper, the photometric measurements are reported in the AB system and the uncertainties are provided at  $1\sigma$  confidence. We assume a flat Lambda cold dark matter cosmology with  $H_0 = 67.4$  km s $^{-1}$  Mpc $^{-1}$ ,  $\Omega_m = 0.31$ , and  $\Omega_{\Lambda} = 0.69$  (Planck Collaboration et al. 2020).

## 2. Observations

### 2.1. Our X-shooter sample

Motivated by the discovery of iPTF16eh and SN 2018ibb, we collected a sample of 19 SLSNe with the medium-resolution X-shooter spectrograph (program IDs: 105.20PN, 106.21L3, 108.2262 and 110.247C). The triggering criteria of the program were objects that have been already classified as SLSNe-I, were observable from Paranal and have  $z > 0.11$  so that the Mg II  $\lambda\lambda 2796, 2803$  resonance lines are observable with X-shooter. Our primary objectives are to constrain the occurrence of such mass ejections in SLSNe-I and determine the distribution of the CSM properties. This paper focuses on the analysis of two detections in the X-shooter sample, SN 2020xga and SN 2022xgc, which exhibit a second narrow Mg II absorption system in their X-shooter spectra blueshifted by a few thousand km s $^{-1}$  with respect to the Mg II absorption lines originating in the interstellar medium of the host galaxy.

### 2.2. Discovery and classification

#### 2.2.1. SN 2020xga

SN 2020xga was discovered by the Panoramic Survey Telescope and Rapid Response System (Pan-STARRS1; Kaiser et al. 2010) as PS20jxm on the rise on October 4, 2020 at a  $w$ -band magnitude of 19.8 mag at right ascension, declination (J2000.0)  $03^h 46^m 39.37^s$ ,  $-11^{\circ} 14' 33.90''$  (Chambers et al. 2020). It was classified by the extended Public ESO Spectroscopic Survey for Transient Objects (ePESSTO+; Smartt et al. 2015) as a SLSN-I on November 6, 2020 (Gromadzki et al. 2020; Ihanec et al.



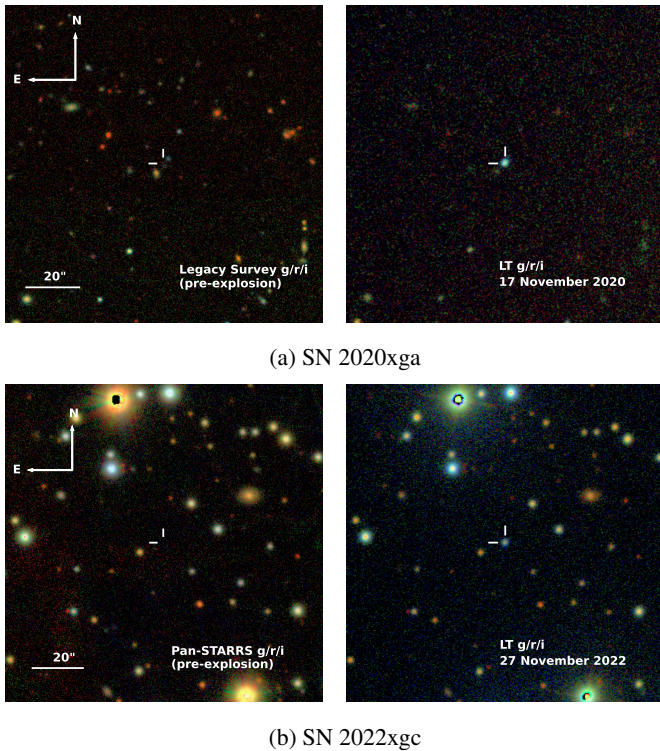


Fig. 1: Images of the fields of SN 2020xga and SN 2022xgc. a) Left: Legacy Survey DR10 image of the field of SN 2020xga before explosion. A faint host galaxy at the SN position is visible, marked by the white crosshairs. Right: *gri* composite image of the SN near peak from Liverpool Telescope (LT) b) Left: PanSTARRS image of the field of SN 2022xgc before explosion. The SN position is marked by the white crosshairs. Right: *gri* composite image of the SN near peak from the LT. All images have a size of  $2 \times 2$  arcminutes and have been combined following the algorithm in Lupton et al. (2004).

2020). An image of the field before and after the explosion is shown in Fig. 1a.

Spectroscopic follow-up showed a redshift of  $z = 0.4296$  (see Sect. 4.1) corresponding to a distance modulus of 41.93 mag. We corrected for the Milky Way (MW) extinction using the dust extinction model of Fitzpatrick (1999) based on  $R_V = 3.1$  and  $E(B - V) = 0.049$  mag (Schlafly & Finkbeiner 2011). As for the host galaxy extinction, we find that the host properties of SN 2020xga are consistent with no extinction within the uncertainties (see Sect. 6). The estimated epoch of maximum light in the rest-frame *g* band is November 19, 2020, MJD = 59 172.5 (see Sect. 3.1).

### 2.2.2. SN 2022xgc

SN 2022xgc was discovered by the Zwicky Transient Facility (ZTF; Bellm et al. 2019; Graham et al. 2019; Dekany et al. 2020) on October 9, 2022 as ZTF22abkmbob at a *g*-band magnitude of 20.8 mag at right ascension, declination (J2000.0)  $07^h 12^m 41.81^s$ ,  $+07^\circ 18' 59.95''$  (Fremling 2022). ePESSTO+ classified it as a SLSN-I on December 2, 2022 (Gromadzki et al. 2022; Poidevin et al. 2022; Grzesiak et al. 2022).

To correct for the MW extinction we again used the dust extinction model of Fitzpatrick (1999),  $R_V = 3.1$  and now with  $E(B - V) = 0.061$  mag (Schlafly & Finkbeiner 2011). We adopted

a spectroscopic redshift of  $z = 0.3103$  (Sect. 4.1) and computed the distance modulus to be 41.11 mag. Since the host of SN 2022xgc is not detected in the catalogs, we cannot derive any host properties and thus, we did not apply any host extinction. The epoch of maximum light in the rest-frame *g* band is estimated to be November 18, 2022, MJD = 59 901.9 (see Sect. 3.1). An image of the field before and after the explosion is shown in Fig. 1b.

### 2.3. Photometry

Photometric measurements of SN 2020xga and SN 2022xgc are available from sky surveys such as the Asteroid Terrestrial-impact Last Alert System (ATLAS; Tonry et al. 2020), and the ZTF survey. We retrieved forced photometry from the ATLAS forced photometry server<sup>2</sup> (Tonry et al. 2018; Smith et al. 2020; Shingles et al. 2021) for both *c* and *o* filters. The clipping and binning, with a bin size of 1 day, of the ATLAS data were done using the `plot_atlas_fp.py` python script (Young 2020). We removed the measurements with  $< 3\sigma$  significance and converted the resulting fluxes to the AB magnitude system using the 3631 Jy zeropoint. The ZTF forced point spread function (PSF)-fit photometry was requested from the Infrared Processing and Analysis Center (Masci et al. 2019) for the *gri* bands. To obtain the rest-frame light curve, we followed the ZTF data processing procedure<sup>4</sup> including baseline correction, validation of the flux uncertainties, combining measurements obtained the same night and converting the differential fluxes to the AB magnitude system. Similarly to ATLAS data, a quality cut of  $3\sigma$  was performed to the data.

In addition, both objects were monitored with the 2m Liverpool Telescope (LT; Steele et al. 2004) using the IO:O imager at the Roque de los Muchachos Observatory in the *griz* bands. The images were retrieved from the LT data archive<sup>5</sup> and were processed through a PSF photometry script developed by Hinds and Taggart et al. (in prep). Each measurement was calibrated using stars from the Pan-STARRS (Flewelling et al. 2020) catalog and a cut of  $3\sigma$  was performed.

SN 2020xga was also monitored between November 2020 and July 2021 by ePESSTO+ using the Las Cumbres Observatory in the *griz* bands. We performed photometry using the AUTOMated Photometry of Transients<sup>6</sup> pipeline developed by Brennan & Fraser (2022). The instrumental magnitude of the SN is measured through PSF fitting and the zero point in each image is calibrated with stars from the Pan-STARRS (Flewelling et al. 2020) catalog. We do not discuss the *z*-band photometry because of the poor quality of these images.

The photometric dataset of SN 2022xgc is complemented with four epochs obtained with the Rainbow Camera at the Spectral Energy Distribution Machine (SEDM; Blagorodnova et al. 2018; Rigault et al. 2019; Kim et al. 2022) at Palomar Observatory in the *gri* bands. The data were reduced with the FPipe pipeline described in Fremling et al. (2016). Finally, one epoch of photometry in the *gr* bands was obtained with the Alhambra Faint Object Spectrograph and Camera (ALFOSC) at the 2.56m

<sup>2</sup> <https://fallingstar-data.com/forcedphot/>

<sup>3</sup> <https://gist.github.com/thespacedoctor/86777fa5a9567b7939e8d84fd8c6fa76>

<sup>4</sup> [https://irsa.ipac.caltech.edu/data/ZTF/docs/ZTF\\_zfps\\_userguide.pdf](https://irsa.ipac.caltech.edu/data/ZTF/docs/ZTF_zfps_userguide.pdf)

<sup>5</sup> [https://telescope.livjm.ac.uk/cgi-bin/lt\\_search](https://telescope.livjm.ac.uk/cgi-bin/lt_search)

<sup>6</sup> <https://github.com/Astro-Sean/autophot>

Nordic Optical Telescope (NOT). For the reduction the PyNOT<sup>7</sup> data processing pipeline was utilised. For nights with multiple exposures, we computed the weighted average and we kept only the data with  $> 3\sigma$  significance.

Overall, for SN 2020xga we obtained 68 epochs of photometry spanning from  $-44$  and  $+59$  days post maximum in the *gcroiz* bands with a cadence of 1.5 days in the best-covered *r* band. For SN 2022xgc we obtained 86 photometric epochs between  $-59$  and  $+110$  days after peak in the *gcroiz* bands with an average cadence of 2 days in the *g* and *r* bands which were best covered. The photometry of each object is listed in Table A.1 and Table A.2 for SN 2020xga and SN 2022xgc, respectively.

#### 2.4. Spectroscopy

We acquired five low-resolution spectra of SN 2020xga between November 6, 2020 and December 30, 2020 and six low-resolution spectra of SN 2022xgc between December 1, 2022 and February 12, 2023 with the ESO Faint Object Spectrograph and Camera 2 (EFOSC2; Buzzoni et al. 1984) on the 3.58m ESO New Technology Telescope (NTT) at the La Silla Observatory in Chile under the ePESSTO+ program (Smartt et al. 2015). Additional medium-resolution spectra were obtained for both SN 2020xga between November 2020 and January 2021, and SN 2022xgc between December 2022 and March 2023 with the X-shooter spectrograph.

The spectroscopic data for SN 2022xgc was supplemented with three low-resolution spectra obtained with ALFOSC between November and December 2021, one spectrum obtained on November 22, 2022 with the Kast double spectrograph mounted on the Shane 3m telescope at Lick Observatory, and two spectra taken in November 2022 with the SEDM. We acquired one additional epoch of spectroscopy for SN 2020xga with the Double-Spectrograph (DBSP; Oke & Gunn 1982) mounted on Palomar 200-inch telescope on Palomar Observatory on January 07, 2021. Observations using the SEDM and DBSP were coordinated using the FRITZ data platform (van der Walt et al. 2019; Coughlin et al. 2023).

The NTT spectra were reduced with the PESSTO<sup>8</sup> pipeline. The observations were performed with grisms #11, #13, and #16 using a  $1''0$  wide slit. The integration times varied between 1500 and 5400 s for SN 2020xga and between 900 and 4800 s for SN 2022xgc. The spectra of SN 2020xga on November 16 and 17, 2020 were combined to boost the sigma-to-noise (S/N).

The X-shooter observations were performed for the ultraviolet (UV), visible (VIS), and near-infrared (NIR) arms in nodding mode using  $1''0$ ,  $0''9$ ,  $0''9$  wide slits, respectively and were reduced using the ESO X-shooter pipeline. We followed the following procedure; first the tool *astrocrappy*<sup>9</sup> was used for the removal of cosmic-rays based on the algorithm of van Dokkum (2001), then the data were processed with the X-shooter pipeline v3.6.3 and the ESO workflow engine ESOReflex (Geldoni et al. 2006; Modigliani et al. 2010). The UV and VIS-arm data were reduced in stare mode. The corrected two-dimensional spectra were co-added utilising tools developed by Selsing et al. (2019)<sup>10</sup>. To achieve proper skyline subtraction, the NIR-arm data were processed in nodding mode. The wavelength calibration of all spectra was adjusted to account for barycentric motion. The spectra of the separate arms were combined by aver-

aging the overlap areas. Since we do not expect the spectrum of a SLSN-I to evolve within 4 rest-frame days, we stitched the X-shooter spectra of SN 2020xga on January 10 and 14, 2021 to increase the S/N.

The spectroscopic data obtained with ALFOSC were reduced using the PyPEIT<sup>11</sup> pipeline (Prochaska et al. 2020a,b). The observations were obtained with a  $1''3$  wide slit and grism #4, and the exposure times were between 3344 s and 4000 s. The spectrum on November 13, 2022 was observed under cloudy conditions and thus we do not consider it. The SEDM observations had an integration time of 2250 s and were reduced using the pipeline described in Rigault et al. (2019). The first SEDM spectrum of SN 2022xgc obtained on November 14, 2022 is of insufficient quality and is not presented in the paper. The epoch observed with the DBSP instrument was taken using the D-55 dichroic beam splitter, a blue grating with 600 lines per mm blazed at 4000 Å, a red grating with 316 lines per mm blazed at 7500 Å, and a  $1''5$  wide slit. The data were reduced using the python package DBSP\_DRP4<sup>12</sup> that is primarily based on PyPEIT. Finally, the Kast observations utilised the  $2''0$  wide slit, the 600/4310 grism, and the 300/7500 grating. The Kast data were reduced following standard techniques for CCD processing and spectrum extraction (Silverman et al. 2012) utilising IRAF routines and custom Python and IDL codes<sup>13</sup>.

Each spectrum was flux calibrated against standard stars. The spectral logs for SN 2020xga and SN 2022xgc are presented in Table B.1 and Table B.2, respectively. All the spectra are uploaded on the WISEREP<sup>14</sup> archive (Yaron & Gal-Yam 2012).

#### 2.5. Polarimetry

Linear polarimetry was obtained on SN 2022xgc at two epochs after maximum light at  $+26.1$  (MJD 59928.0) days and at  $+60.1$  (MJD 59962.0) days, observer-frame. A log of the observations is given in Table C.1 in Appendix C. The polarimetry was obtained using a half wave plate in the FAPOL unit and a calcite plate mounted in the aperture wheel of the ALFOSC instrument on the NOT. The calcite plate provides the simultaneous measurement of the ordinary and the extraordinary components of two orthogonal polarized beams. The half wave plate can be rotated over 16 angle positions in steps of  $22.5^\circ$  from  $0^\circ$  to  $337.5^\circ$ . As a standard, we used 4 angle positions ( $0^\circ$ ,  $22.5^\circ$ ,  $45^\circ$ , and  $67.5^\circ$ ) to sample the linear Stokes  $Q - U$  parameters space.

The pipeline used to reduce the data is the same as the one introduced in Poidevin et al. (2022). The photometry of the ordinary and extraordinary beams was done using aperture photometry of size  $\sim 2$  to 3 times the Full-Width at Half-Maximum (FWHM) of punctual sources in the images. For multiple sequences of 4 Half-Wave Plate angles the polarization was obtained by summing-up the fluxes from the ordinary and extraordinary beams to minimize the propagation of the uncertainties. The instrumental polarization (IP) was first estimated using the unpolarized star HD 14069. The IP degree is of order 0.1% in the *R*-band, and of order 0.2% in the *V*-band (see Table C.2). These averaged Stokes  $\bar{Q}$  and  $\bar{U}$  values were subsequently removed from the Stokes parameters  $Q - U$  estimates of the polarized calibration stars HD 251204 and BD+59 389 and of SN 2022xgc. The polarized stars were used to calculate the zero polarization angle (ZPA) used to rotate the Stokes  $Q$ ,  $U$  parameters from the

<sup>7</sup> <https://github.com/jkrogager/PyNOT>

<sup>8</sup> <https://github.com/svalenti/pessto>

<sup>9</sup> <https://github.com/astropy/astrocrappy>

<sup>10</sup> [https://github.com/jselsing/XSGRB\\_reduction\\_scripts](https://github.com/jselsing/XSGRB_reduction_scripts)

<sup>11</sup> <https://pypeit.readthedocs.io/en/release/>

<sup>12</sup> [https://github.com/finagle29/dbsp\\_drp](https://github.com/finagle29/dbsp_drp)

<sup>13</sup> <https://github.com/isshivvers/TheKastShiv>

<sup>14</sup> <https://www.wiserep.org>



ALFOSC FAPOL instrument reference frame to the sky reference frame in Equatorial coordinates. The polarization angles are counted positively from North to East. When applicable, the polarization degree and polarization angle obtained at each of these steps are reported in Table C.2.

## 2.6. Host galaxy observations

We retrieved science-ready co-added images from the DESI Legacy Imaging Surveys (LS; Dey et al. 2019) Data Release (DR) 10, and archival science-ready images obtained with MegaCAM at the 3.58 m Canada-France-Hawaii Telescope (CFHT) for SN 2020xga. We measured the brightness with the aperture photometry tool presented in Schulze et al. (2018) using an aperture similar to the other images. The photometry were calibrated against stars from the Sloan Digital Sky Survey DR9 (Ahn et al. 2012) and Pan-STARRS1 (Chambers et al. 2016). The host galaxy of SN 2022xgc is not detected in any catalog and thus, we provide the upper limits of the Dark Energy Survey images obtained with the Dark Energy Camera (DECam) at the Cerro Tololo Inter-American Observatory (CTIO). Table 1 summarises the measurements in the different bands.

Table 1: Photometry of the host galaxies of SN 2020xga and SN 2022xgc.

Survey or Telescope/Instrument	Filter	Brightness (mag)
<b>SN 2020xga</b>		
LS	<i>g</i>	$23.56 \pm 0.09$
LS	<i>r</i>	$23.26 \pm 0.12$
CFHT/MegaCAM	<i>i</i>	$22.96 \pm 0.09$
LS	<i>z</i>	$22.75 \pm 0.15$
<b>SN 2022xgc</b>		
CTIO/DECam	<i>g</i>	$> 23.6$
CTIO/DECam	<i>r</i>	$> 23.4$
CTIO/DECam	<i>i</i>	$> 23.0$
CTIO/DECam	<i>z</i>	$> 22.7$
CTIO/DECam	<i>y</i>	$> 21.3$

**Notes.** All measurements are reported in the AB system and not corrected for reddening. Non-detections are reported at  $3\sigma$  confidence.

## 3. Photometry

### 3.1. General light-curve properties

To estimate the absolute magnitudes of SN 2020xga and SN 2022xgc we used  $M = m - \mu - A_{MW} - K_{\text{corr}}$  where  $m$  is the apparent magnitude,  $\mu$  is the distance modulus,  $A_{MW}$  is the extinction caused by the MW and the last term is the K-correction. For the last term we used the expression  $-2.5 \log(1+z)$  which we found to be consistent within 0.1 mag with the full K-correction using the spectra near peak, as suggested in Chen et al. (2023a) as well. This gave  $K_{\text{corr}} = -0.39 \pm 0.1$  mag for SN 2020xga and  $K_{\text{corr}} = -0.29 \pm 0.1$  mag for SN 2022xgc. The multiband light curves in apparent and absolute magnitude systems for SN 2020xga and SN 2022xgc are shown in Fig. 2.

To estimate the time of first light, we fitted a baseline to the non-detection data points and a second-order polynomial to the rising part of the light curve, with the cross-point of the two

fits being the time of first light. To estimate the uncertainty in the first-light epoch we run a Monte Carlo algorithm of randomly selected data points from a Gaussian distribution of the  $1\sigma$  uncertainties for each of the selected flux measurements. For SN 2020xga the resulting dates were MJD  $59109.8 \pm 0.2$  in the *g* band and MJD  $59110.5 \pm 1.0$  in the *r* band. We adopted a weighted average of MJD  $59109.8 \pm 0.2$  which is also before the first *c*-band detection (MJD 59110.5). The uncertainty is statistical only, but the systematic error is likely a few days. This is shown for SN 2022xgc, where this method resulted in the dates of MJD  $59836.5 \pm 0.4$  in the *g* band and MJD  $59842.2 \pm 2.6$  in the *r* band. The weighted mean of MJD  $59836.6 \pm 2.5$  is after the first three *r*-band detections which could be associated with a pre-peak bump as seen in the light curves of some SLSNe-I (e.g., Leloudas et al. 2012; Nicholl et al. 2015b; Smith et al. 2016; Vreeswijk et al. 2017; Angus et al. 2019). Since SN 2022xgc does not have stringent upper limits due to solar conjunction and the first *r*-band detections are real, we cannot exclude them and we instead took as time of the first light the first *r*-band data point MJD 59825.

To estimate the light-curve properties we used the *r*-band light curve, which falls into the rest-frame *g* band at the redshifts of SN 2020xga and SN 2022xgc (Chen et al. 2023a). We used the method from Angus et al. (2019) for the light-curve interpolation and fit a Gaussian process (GP) regression, utilizing the PYTHON package GEORGE (Ambikasaran et al. 2015) with a Matern 3/2 kernel. We used the interpolated *r*-band light curve to estimate the peak magnitude as well as to define the rise and decline timescales as a fraction of the maximum flux following Chen et al. (2023a). To estimate the rest-frame *g-r* color at peak we used the peak magnitudes inferred from the interpolated rest-frame *g*- and *r*-band light curves, K-corrected using the spectra closer to the peak. The photometric properties of SN 2020xga and SN 2022xgc obtained from this analysis are listed in Table 2. The timescales are reported in rest-frame days.

Table 2: Light curve properties of SN 2020xga and SN 2022xgc

Property	SN 2020xga	SN 2022xgc
$M_{r,\text{peak}}$ (mag)	$-22.30 \pm 0.04$	$-21.97 \pm 0.05$
Peak time (MJD)	$59172.5^{+9.4}_{-11.7}$	$59901.9^{+15.1}_{-12.0}$
$t_{1/2,\text{rise}}$ (days)	$26.2^{+6.9}_{-8.3}$	$28.2^{+9.2}_{-11.6}$
$t_{1/2,\text{decline}}$ (days)	$23.2^{+8.3}_{-6.7}$	$42.8^{+11.9}_{-9.6}$
$t_{1/e,\text{rise}}$ (days)	$32.4^{+6.9}_{-8.4}$	$33.7^{+11.6}_{-9.2}$
$t_{1/e,\text{decline}}$ (days)	$29.6^{+8.4}_{-6.8}$	$58.6^{+9.8}_{-12}$
$(g-r)_{\text{peak}}$ (mag)	$-0.23 \pm 0.05$	$-0.24 \pm 0.05$

In Fig. 3, we place the light curve properties of SN 2020xga and SN 2022xgc in the context of the homogeneous ZTF SLSNe-I sample from Chen et al. (2023a) which studied the photometric properties of 78 H-poor SLSNe-I. In the four different panels, we show the kernel density estimates (KDEs) of the ZTF sample, which are an outcome of a Monte Carlo simulation accounting for the asymmetric errors. Both SN 2020xga and SN 2022xgc are placed in the bright side of the distribution while the decline times span across the whole distribution. The rise times and the *g-r* peak magnitudes are rather average compared to the median values of the ZTF sample.

### 3.2. Bolometric light curve

To construct the bolometric light curves of SN 2020xga and SN 2022xgc, and derive the blackbody temperatures and radii,



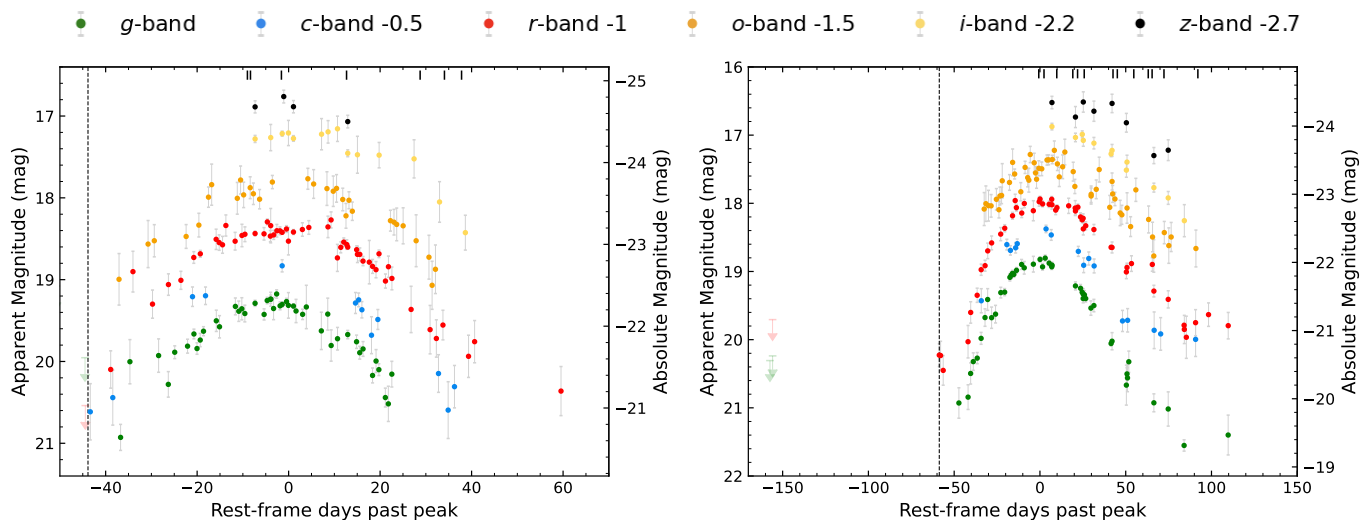


Fig. 2: Optical light curves of SN 2020xga (left panel) and SN 2022xgc (right panel). The magnitudes are corrected for MW extinction and cosmological K-correction. Upper limits are presented as downward-pointing triangles in a lighter shade. The epochs of the spectra are marked as thick lines at the top of the figure. The dashed line represent the estimated time of the first light. The x-axis is in rest-frame days with respect to the rest-frame  $g$ -band maximum.

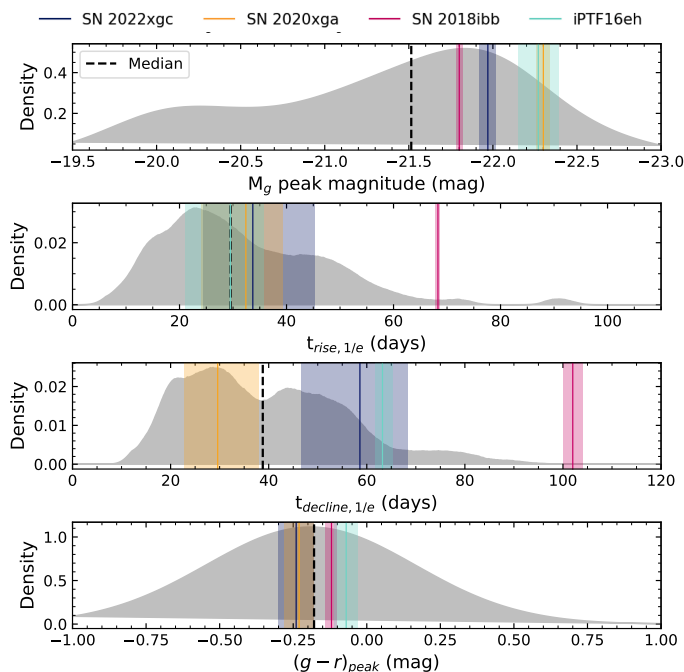


Fig. 3: Comparison of the photometric properties of SN 2020xga, SN 2022xgc, SN 2018ibb and iPTF16eh with the ZTF SLSNe-I sample (Chen et al. 2023a). Top: KDE distribution of the  $M_g$  peak magnitudes for 78 ZTF SLSNe-I. Second: KDE plot of the  $e$ -folding rise time for 69 ZTF SLSNe-I. Third:  $e$ -folding decline time distribution for 54 ZTF SLSNe-I. Bottom: Rest-frame peak  $g - r$  color distribution for 39 ZTF SLSNe-I. The vertical colored lines along with the errors (shaded regions) illustrate the positions of SN 2020xga, SN 2022xgc, SN 2018ibb and iPTF16eh and the black vertical lines the median values of the ZTF sample.

we constructed the spectral energy distributions (SEDs). We interpolated all light curves using the GP method described in

Sect. 3.1 to match the epochs with  $r$ -band observations and converted the magnitudes to spectral luminosities  $L_\lambda$  for each band at each epoch. To extract information about the photospheric temperature and radius, we fit blackbody curves to each SED. The derived temperature and radius evolution for SN 2020xga and SN 2022xgc are plotted in Fig. 4. We compared only with events of the ZTF sample characterised as normal by Chen et al. (2023a). We find that the temperatures of both objects are comparable to those of the ZTF SLSNe-I and evolve similarly to the ZTF sample, declining over time. On the other hand, while the radius evolution of SN 2020xga and SN 2022xgc follows the rising trend seen for the SLSNe-I in the ZTF sample, the photospheric radius of both objects expands to larger values than for the rest of the ZTF sample. This is why these objects are so luminous while their temperatures are typical. In SN 2020xga and SN 2020xgc the photospheric radius decreases after 25 and 50 days respectively. We caution that the quoted error bars are statistical only, and do not include any systematic effects e.g. from the fact that we are fitting to optical data only, while the peak of the blackbody is in the UV at early times.

To construct the bolometric light curves of SN 2020xga and SN 2022xgc, we started by integrating the SED using only the  $gro$  filters since the  $i$  and  $z$  light curves cover only a few epochs and the  $c$  filter is already covered by the  $g$  and  $r$  bands. To account for the missing flux in the NIR we fit a blackbody to the  $gro$  SED and integrated the blackbody tail up to  $24\,400\text{ \AA}$ , beyond which the contribution to the bolometric light curve is negligible in the photospheric phase ( $\sim 1\%$ ; Ergon et al. 2013). For the UV correction, we followed the approach of Lyman et al. (2014) to capture the effect of the line blanketing commonly encountered in SLSNe (e.g., Yan et al. 2017b). To do this, we linearly extrapolated the SED from the observed  $g$  band to  $2000\text{ \AA}$  where the luminosity is set to zero. The total bolometric luminosity is the sum of the observed  $gro$  luminosity and the UV and NIR corrections. The bolometric light curves of SN 2020xga and SN 2022xgc are shown in Fig. 5. The peak bolometric luminosity is estimated to be  $L_{\text{bol,peak}} \gtrsim 2.7 \pm 0.1 \times 10^{44}\text{ erg s}^{-1}$  for SN 2020xga and  $L_{\text{bol,peak}} \gtrsim 1.9 \pm 0.1 \times 10^{44}\text{ erg s}^{-1}$  for

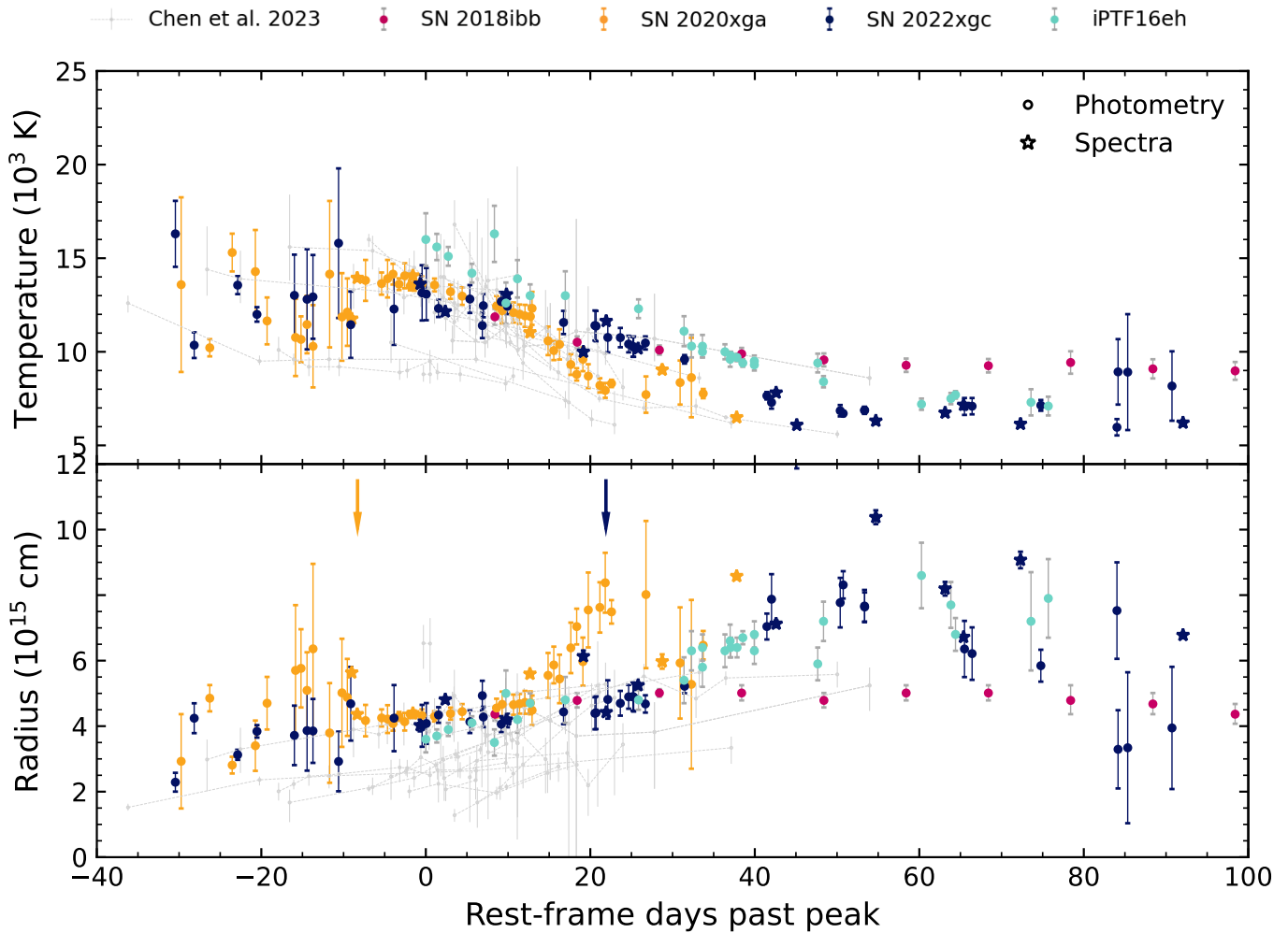


Fig. 4: Blackbody temperatures and radii of SN 2020xga, SN 2022xgc, SN 2018ibb and iPTF16eh. Top: Temperature evolution of SN 2020xga, SN 2022xgc, SN 2018ibb and iPTF16eh derived from the blackbody fits to the photometric (circle symbols) and the spectroscopic (star symbols) data. The gray background points represent the temperature evolution of the ZTF sample (Chen et al. 2023a). Bottom: Blackbody radius evolution of SN 2020xga, SN 2022xgc, SN 2018ibb and iPTF16eh utilizing photometry and spectra in comparison with the ZTF sample (grey). The arrows indicate the epochs where the X-shooter spectra of SN 2020xga and SN 2022xgc show the second Mg II absorption system.

SN 2022xgc. These values are typical for SLSNe-I being close to the median value of  $2.00^{+1.97}_{-1.44} \times 10^{44}$  erg s<sup>-1</sup> reported for 76 SLSNe-I in Chen et al. (2023a) using the *g* and *r* filters and the value of  $2.00^{+1.98}_{-1.36} \times 10^{44}$  erg s<sup>-1</sup> found in Gomez et al. (2024) studying a heterogeneous sample of 262 SLSNe-I.

To include the epochs for which we do not have complete *gro* data and therefore cannot construct the SED, we assumed a constant bolometric correction. For SN 2020xga, for the later epochs that only have *r*-band data available, we used the same ratio of the *r*-band flux to the total flux that we measured at the latest epoch with multi-band data. Similarly, for the rising part of the light curve for SN 2022xgc for which we have only *g*- and *r*-band measurements, we applied the same bolometric correction measured in the first multi-band epoch. The bolometric luminosity used is the average of the luminosities calculated for the *g* and *r* bands. The data points assuming bolometric corrections are shown as open circles in Fig. 5. We note that this approach has two main caveats since at early phases the bolometric correction progressively underestimates the UV contribution while in the later phases the IR contribution gets more significant. By inte-

grating the area below the bolometric light curves we estimated the total radiated energy to be  $E_{\text{rad}} \gtrsim 1.8 \pm 0.1 \times 10^{51}$  erg for SN 2020xga and  $E_{\text{rad}} \gtrsim 0.9 \pm 0.2 \times 10^{51}$  erg for SN 2022xgc. We note that these errors only account for the statistical errors in the fit and not for any systematic errors. These values are consistent within the uncertainties with the median  $E_{\text{rad}} = 1.3^{+1.2}_{-0.9} \times 10^{51}$  erg found in Gomez et al. (2024).

### 3.3. Photometric comparison to iPTF16eh and SN 2018ibb

In Fig. 3 we compared the light-curve properties of SN 2020xga and SN 2022xgc with the well-studied sample of SLSNe-I from the ZTF (Chen et al. 2023a). In this plot we also included the photometric properties of SN 2018ibb (Schulze et al. 2024) and iPTF16eh (Lunnan et al. 2018b). These two SLSNe-I, at  $z = 0.166$  and  $z = 0.427$  respectively, are the only other SLSNe-I in which the two Mg II absorption-line system is detected in their spectra. To determine whether the objects with this remarkable spectroscopic similarity stand apart in photometry space, we also plot the rest-frame *g*-band peak magnitudes, rise and de-

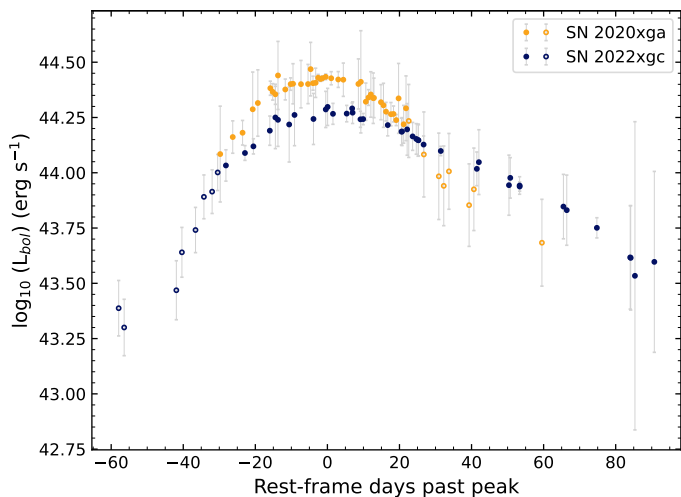


Fig. 5: Bolometric light curves of SN 2020xga and SN 2022xgc with bolometric corrections applied. The circles correspond to the derived luminosities using *gro* filters and the open circle symbols illustrate the bolometric luminosity assuming the same bolometric correction as the nearest epochs with multiband data. The errorbars represent statistical errors.

cline timescales, and  $g-r$  magnitudes at peak of SN 2018ibb and iPTF16eh in Fig. 3. We note that since there are no data available in the rest-frame  $g$  band in the rising part of iPTF16eh’s light curve, we used the rest-frame  $u$  band to estimate the rise time.

Similarly to SN 2020xga and SN 2022xgc, SN 2018ibb and iPTF16eh are placed on the bright side of the ZTF luminosity distribution. The peak absolute magnitudes of these four objects span from  $-21.8$  mag to  $-22.3$  mag with a mean of  $-22.1$  mag putting these objects among the most luminous SLSNe-I compared to the ZTF sample. The decline times of these four objects span across the whole distribution while the  $g-r$  colours at peak are close to the median value of the ZTF sample. The rise times of iPTF16eh, SN 2020xga and SN 2022xgc are consistent within the errors with the median of the sample, whereas SN 2018ibb is placed in the far slow end of the distribution as one of the longest rising SLSNe-I compared to the Chen et al. (2023a) sample.

The blackbody temperature and radius evolution of iPTF16eh and SN 2018ibb are plotted in Fig. 4. Both objects follow the temperature evolution of the ZTF sample with iPTF16eh having higher temperatures compared to the bulk of the population. The photospheric radius of SN 2018ibb remains constant for almost 100 days after maximum light, while the radius evolution of iPTF16eh is increasing with time. However, similarly to SN 2020xga and SN 2022xgc the size of the photosphere in iPTF16eh is getting larger than that of most ZTF SLSNe-I. The photospheric radius of iPTF16eh appears to decline after  $\sim 60$  days.

To better illustrate the variety in the photometric properties of these four objects, we plot the rest-frame  $g$ -band light curves in Fig. 6. The absolute magnitudes of all the objects are K-corrected and corrected for MW extinction. We see that the light curve of SN 2018ibb differs significantly compared to the other three SLSNe-I with a second Mg II system, by being very slow evolving and presenting bumps and undulations in its light curve. There are no signs of post-peak bumps or wiggles in the light curves of SN 2020xga while, the light curve of SN 2022xgc shows a possible flattening in the  $gcr$  bands starting

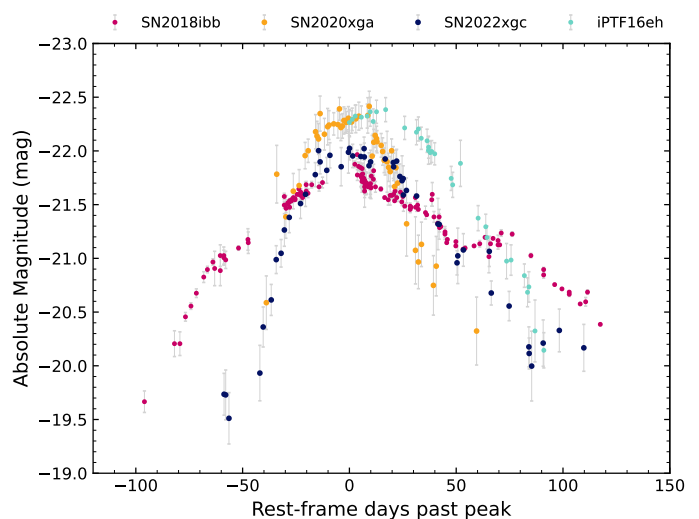


Fig. 6: Rest-frame  $g$ -band absolute magnitude light curves of SN 2020xga and SN 2022xgc in comparison with iPTF16eh and SN 2018ibb. The magnitudes are K-corrected and corrected for MW extinction. The x-axis is in rest-frame days with respect to the  $g$ -band peak, with the exception of iPTF16eh, where the  $u$  band was utilized for estimating the peak owing to the lack of data in the rising part of the  $g$ -band light curve.

$\sim 80$  days after peak (see Sect. 7). In SN 2022xgc a pre-bump in the  $r$  band was observed immediately after explosion, whereas in SN 2020xga a possible bump can be seen in the  $g$  and  $r$  band light curves at  $\sim -30$  days. All four objects are very energetic with radiated energies  $E_{\text{rad}} \gtrsim 1 \times 10^{51}$  erg  $\text{s}^{-1}$ .

### 3.4. Light-curve modeling

We modeled the observed multiband light curves of SN 2020xga and SN 2022xgc using the Bayesian Inference software package for fitting electromagnetic transients, REDBACK (Sarin et al. 2024). We input the redshift of the SLSNe (see Sect. 4.1), the *gro*i photometric observations of SN 2020xga and SN 2022xgc corrected for extinction (we excluded the  $z$  band due to the low number of datapoints) and a list of priors shown in Table 3. We explored the parameter space with the nested sampling package DYNesty (Ashton et al. 2019; Speagle 2020a).

To fit the data, we selected the versatile general magnetar-driven supernova model described in Omand & Sarin (2024) under the assumption that the light curves of SN 2020xga and SN 2022xgc are powered by the spin-down of a rapidly rotating newly formed magnetar (Ostriker & Gunn 1971; Arnett & Fu 1989; Kasen & Bildsten 2010; Chatzopoulos et al. 2012; Inerra et al. 2013). This model sets the magnetar braking index  $n$  as a variable, relaxing the assumption of a vacuum dipole spin-down mechanism and includes the dynamical evolution of the ejecta (Sarin et al. 2022) coupling it to both the explosion energy and the spin-down luminosity of the magnetar itself. We used the default priors defined in Omand & Sarin (2024) relaxing the priors for the explosion energy  $E_{\text{SN}}$  and the temperature floor  $T_{\text{floor}}$ . The opacity  $\kappa$  which was fixed at  $0.04 \text{ cm}^2 \text{ g}^{-1}$  which is a good approximation for Type Ic SNe as shown in Kleiser & Kasen (2014) (see their Fig. 3) considering that the blackbody temperature tends to overestimate the temperature of the photosphere (Dessart 2019). We note that if we set the  $\kappa$  parameter free, our results do not change significantly, suggesting that the



Table 3: Priors and posterior of the parameters fitted with REDBACK for the generalised magnetar model. The  $\mathcal{U}$  stands for uniform, and  $\mathcal{L}$  for log-uniform. The FD acronym stands for first detection and represents the date of the first real detection. The uncertainties are reported at  $1\sigma$  significance.

Parameters	Priors	Best-fit values	
		SN 2020xga	SN 2022xgc
$L_0$ (erg s $^{-1}$ )	$\mathcal{L}(10^{40}, 10^{50})$	$1.2^{+0.1}_{-0.1} \times 10^{45}$	$8.1^{+0.6}_{-0.4} \times 10^{44}$
$t_{SD}$ (s)	$\mathcal{L}(10^2, 10^8)$	$1.9^{+0.7}_{-0.5} \times 10^7$	$1.9^{+0.4}_{-0.3} \times 10^7$
$n$	$\mathcal{U}(1.5, 10)$	$1.9^{+0.3}_{-0.3}$	$5.5^{+2.3}_{-1.9}$
$f_{s6Ni}$	$\mathcal{L}(10^{-6}, 1)$	$5.1^{+49.8}_{-4.9} \times 10^{-4}$	$1.9^{+44.9}_{-1.9} \times 10^{-3}$
$M_{ej}$ ( $M_{\odot}$ )	$\mathcal{U}(0.1, 100)$	$7.0^{+0.4}_{-0.4}$	$9.4^{+0.7}_{-0.7}$
$E_{SN}$ (erg)	$\mathcal{U}(5 \times 10^{49}, 3 \times 10^{51})$	$2.97^{+0.02}_{-0.04} \times 10^{51}$	$2.4^{+0.3}_{-0.3} \times 10^{51}$
$\kappa_{\gamma}$ (cm $^2$ g $^{-1}$ )	$\mathcal{L}(10^{-4}, 10^4)$	$8.3^{+1.2}_{-1.1} \times 10^{-3}$	$3.6^{+0.9}_{-0.7} \times 10^{-3}$
$T_{floor}$ (K)	$\mathcal{U}(3 \times 10^3, 2 \times 10^4)$	$11494^{+242}_{-232}$	$6605^{+185}_{-205}$
$t_{exp}$	$\mathcal{U}(FD - 100, FD - 0.1)$	$59096.3^{+1.2}_{-1.2}$	$59824.3^{+0.4}_{-0.6}$

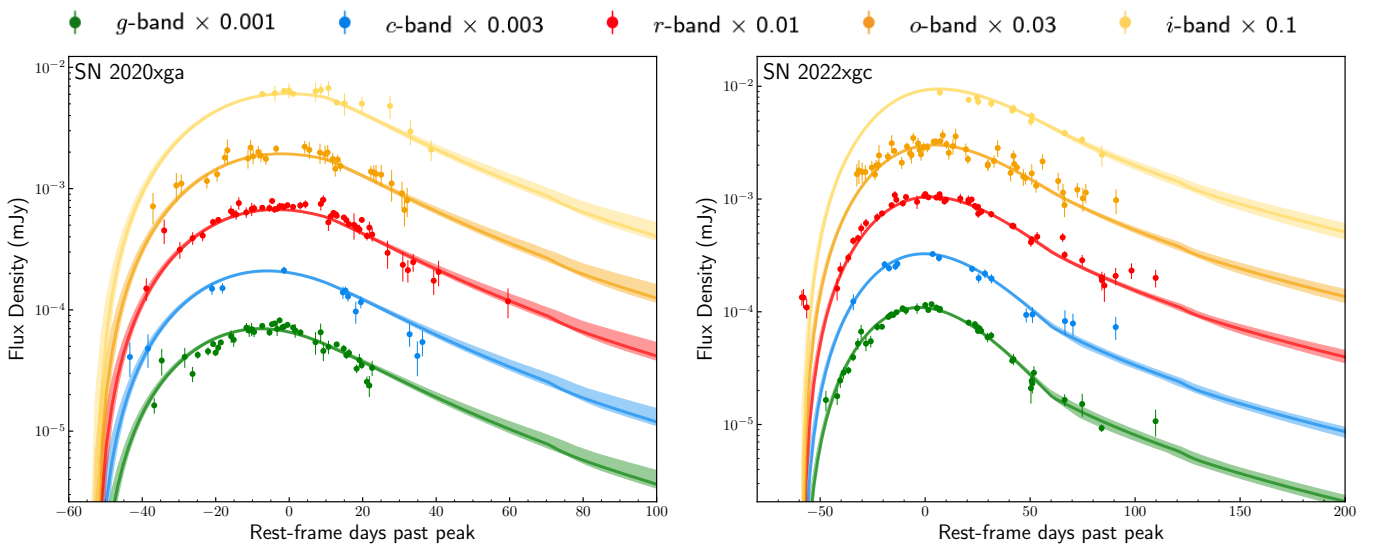


Fig. 7: Multiband light curves of SN 2020xga (left panel) and SN 2022xgc (right panel) with their resulting fits from REDBACK. The colored solid lines indicate the light curves from the model with the maximum likelihood, while the shaded areas depict the 90 percent credible interval. The x-axis is in rest-frame days with respect to the rest-frame  $g$ -band maximum.

choice of opacity plays a minimal role in our inference. However, we note that the opacity is kept constant with time and a time-dependent opacity could yield different results. This model assumes a modified SED accounting for the line blanketing in the UV part of the SLSN spectra (Chomiuk et al. 2011) similar to the one used in Nicholl et al. (2017). The REDBACK light curve fits are shown in Fig. 7, and the resulting values of the posteriors are given in Table 3. The corner plots are presented in Fig. D.1 and Fig. D.2 for SN 2020xga and SN 2022xgc, respectively (see Appendix D).

In SN 2020xga (Fig. 7; left panel), the model captures well the rise (apart from the  $i$  band, which does not have data during the rise), peak, and decline in all five filters up to 30 days, after which the model declines slower than the data. The model fails to fit the first real detection in the  $c$  band and a possible small bump at  $\sim -30$  days which is visible in the  $g$  and  $r$  bands. The latter is not unexpected since this model can explain only a smooth light curve (see discussion in Omand & Sarin 2024). Similarly, in SN 2022xgc (Fig. 7; right panel), the model fits well the SN multi-band light curve both in the rise and the decline up to  $\sim 60$  days, after which the model declines faster than the data in the  $r$  and  $c$  bands. In addition, the model does not capture the first

three data points in the  $r$  band, which, as discussed in Sect. 3.1, could potentially be a pre-bump often seen in the light curves of SLSNe-I. A possible explanation for the early bumps could be interaction with extended material (Piro 2015) or magnetar-driven shock breakout (Kasen 2017).

The general magnetar-driven supernova model uses the initial magnetar spin-down luminosity  $L_0$  and the magnetar spin-down time  $t_{SD}$  as input parameters instead of the initial magnetar spin period in ms  $P_{0,ms}(= P/10^3$  s), the magnetic field  $B_{14}(= B/10^{14}$  G) and the neutron star mass  $M_{NS}$  used in previous magnetar models (e.g., Nicholl et al. 2017). To recover these parameters we used the scalings,

$$E_{rot} = \frac{n-1}{2} L_0 t_{SD} \text{ erg} \quad (1)$$

$$E_{rot} = 2.6 \times 10^{52} P_{0,ms}^{-2} \text{ erg} \quad (2)$$

Assuming a  $1.4 M_{\odot}$  neutron star with the same equation of state as in Nicholl et al. (2017), we found the rotational energy of the magnetar  $E_{rot}$  to be  $1.1 \times 10^{52}$  erg for SN 2020xga and  $E_{rot} =$

$3.3 \times 10^{52}$  erg for SN 2022xgc, while  $P_{0,ms}$  is estimated to be  $1.6 \pm 0.1$  and  $0.9 \pm 0.2$  for SN 2020xga and SN 2022xgc, respectively. The estimated  $P_{0,ms}$  values in SN 2020xga and SN 2022xgc are close to the so-called mass-shedding limit, the limit at which the centrifugal force throws mass off the surface of the magnetar (e.g., Metzger et al. 2015; Watts et al. 2016).

The ejecta masses of  $7.0 M_{\odot}$  and  $9.3 M_{\odot}$  for SN 2020xga and SN 2022xgc respectively, resulting from the general magnetar-driven supernova model are consistent with the findings of Chen et al. (2023b), who found that the median ejecta mass is  $5.1^{+4.0}_{-2.4} M_{\odot}$ . However, we note that this comparison is limited by the different physics included in the model used in this paper and the model of Nicholl et al. (2017) used in the paper of Chen et al. (2023b). In addition, the model estimates the explosion dates  $t_{exp}$  of SN 2020xga and SN 2022xgc to be 13 and 1 days, respectively, earlier than the values found in Sect. 3.1. These small discrepancies are not unreasonable given that both SNe were luminous already at the time of the first detection and thus our approach in Sect. 3.1 constrain the time of first light rather than the explosion date.

Since the ejecta velocity  $v_{ej}$  in the general magnetar-driven supernova model is not constant and the ejecta evolve dynamically as a function of time, we calculated the diffusion timescale  $t_{diff}$

$$t_{diff} = 9.8 \times 10^5 \left( \frac{M_{ej}}{1 M_{\odot}} \right)^{1/2} \left( \frac{v_{ej}}{10^4 \text{ km s}^{-1}} \right)^{-1/2} \text{ s} \quad (3)$$

using the ejecta velocity at peak. The  $v_{ej}$  at peak derived from the most-likely model in REDBACK is  $10446 \text{ km s}^{-1}$  for SN 2020xga and  $8304 \text{ km s}^{-1}$  for SN 2022xgc and thus, the  $t_{diff}$  is estimated to be 29 days and 38 for SN 2020xga and SN 2022xgc, respectively. We note that the ejecta velocities calculated in REDBACK do not have the same physical meaning as the line velocities extracted from the spectra in Sect. 4.3. By computing the ratio of  $t_{SD}/t_{diff}$ , we could determine the fraction of the spin-down luminosity converted to kinetic energy accelerating the ejecta (Suzuki & Maeda 2021; Sarin et al. 2022). The ratios of the two timescales are 7.6 for SN 2020xga and 6.6 for SN 2022xgc. These two ratios show that the radiated and kinetic energy are dominated by magnetar spin-down, as expected for SLSNe-I (Suzuki & Maeda 2021; Omand & Sarin 2024).

### 3.5. Imaging polarimetry

The polarization degrees obtained on SN 2022xgc, and reported in Table C.2 are all very low ( $< 0.5\%$ ), and all constrained to about or less than  $2\sigma$ . The final values shown in bold (Column 9) were obtained after bias correction following the equation given in Wang et al. (1997):

$$P = (P_{obs} - \sigma_P^2/P_{obs}) \times h(P_{obs} - \sigma_P), \quad (4)$$

where  $h$  is the Heaviside function,  $P_{obs}$  is the observed polarization and  $\sigma_P$  is the  $1\sigma$  error.

The debiased measurements obtained on SN 2022xgc displayed in the last column of Table C.2 have been obtained without making any MW polarization correction. The first important point to notice is that they all show that the percentage of polarization is consistently low and does not seem to vary with time. The second important point is that these measurements are all consistent with the low level of Galactic polarization expected in that region of the sky. The Galactic extinction along the line of sight at the coordinates of SN 2022xgc, is such that

$E(B - V) = 0.061$  (Schlafly & Finkbeiner 2011). Following Serkowski et al. (1975), this means that, in case of a magnetic field perfectly lying on the plane-of-sky, the empirical upper limit on the optical degree of polarization produced by dichroic absorption by magnetically aligned Galactic dust grains, should be  $P_{max} = 9 \times E(B - V) = 0.55\%$ . A look at the measurements of the two closest known polarized stars, HD 58784 with  $P_V = 0.65 \pm 0.2\%$  and, HD 57291 with  $P_V = 0.37 \pm 0.2\%$ , in the vicinity of SN 2022xgc, all more than 2 degrees apart from its position on the plane-of-sky, support this statement. These data were retrieved from the compiled catalog of optical polarization measurements by Heiles (2000).

The polarization angles displayed in Table C.2 show polarization angles that differ from about 90 degrees between the two epochs. The constraints on the polarization angles are low S/N, but as an ultimate test, we estimated the variations of polarization degree obtained between each epoch in each filter. This was done using the values of the Stokes parameters before debiasing the data. Any IP and ZPA corrected Stokes parameter on SN 2022xgc should be the sum of a constant contribution from the MW and from the host galaxy (if any) added to a possibly variable contribution from the SN. Therefore a differential measurement between two epochs should assess the degree of variation in polarization associated to the SN. In the *R*-band the differential is,  $\Delta P(R) = 0.29 \pm 0.16\%$ , while in the *V*-band it is,  $\Delta P(V) = 0.52 \pm 0.23\%$ .

We conclude that the estimates given in Table C.2 are likely estimates of the MW polarization contribution and that any contribution that could be associated with SN 2022xgc and its host galaxy should only be a few tenths of a percent. This low level rejects any detection of jet activities. If the level of polarization associated with SN 2022xgc changed between the two epochs, it should only be a fraction of a percent, i.e., very low. This low level of variation in the polarization level rejects any strong change in the shape of the photosphere of the SN between the two epochs.

All these results seem consistent with the statistical results obtained by Pursiainen et al. (2023) on a sample of 16 SLSNe. In this work, the data obtained before maximum light indicate nearly spherical photospheres. No clear relation is found between the polarimetry and spectral phase after maximum light, and an increasing polarisation degree is measured only on a sub-sample of 4 SLSNe which have irregular light curves declines. The light curve decline of SN 2022xgc looks smooth and regular (see Figure 7, right) at the phases when polarimetry was obtained (+26.1 days and +60.1 days). If any strong CSM interaction with the photosphere of SN 2022xgc happened during these two phases, it appears that it did not affect the symmetry of the system.

## 4. Spectroscopy

### 4.1. Redshift

To estimate the precise redshifts of SN 2020xga and SN 2022xgc we examined the X-shooter spectra of SN 2020xga at  $-8.3$  days and SN 2022xgc at  $+21.9$  days after maximum light and identified emission and absorption lines from the interstellar medium and H II regions in the host galaxy. Figure 8 shows the galaxy lines that appear in the spectra of SN 2020xga and SN 2022xgc and that we used for the redshift determination.

We identified in the spectrum of SN 2020xga the galaxy's narrow absorption Fe II doublet  $\lambda\lambda 2586, 2600$  and Mg II doublet  $\lambda\lambda 2796, 2803$ , and the galaxy's narrow emission [O II] doublet

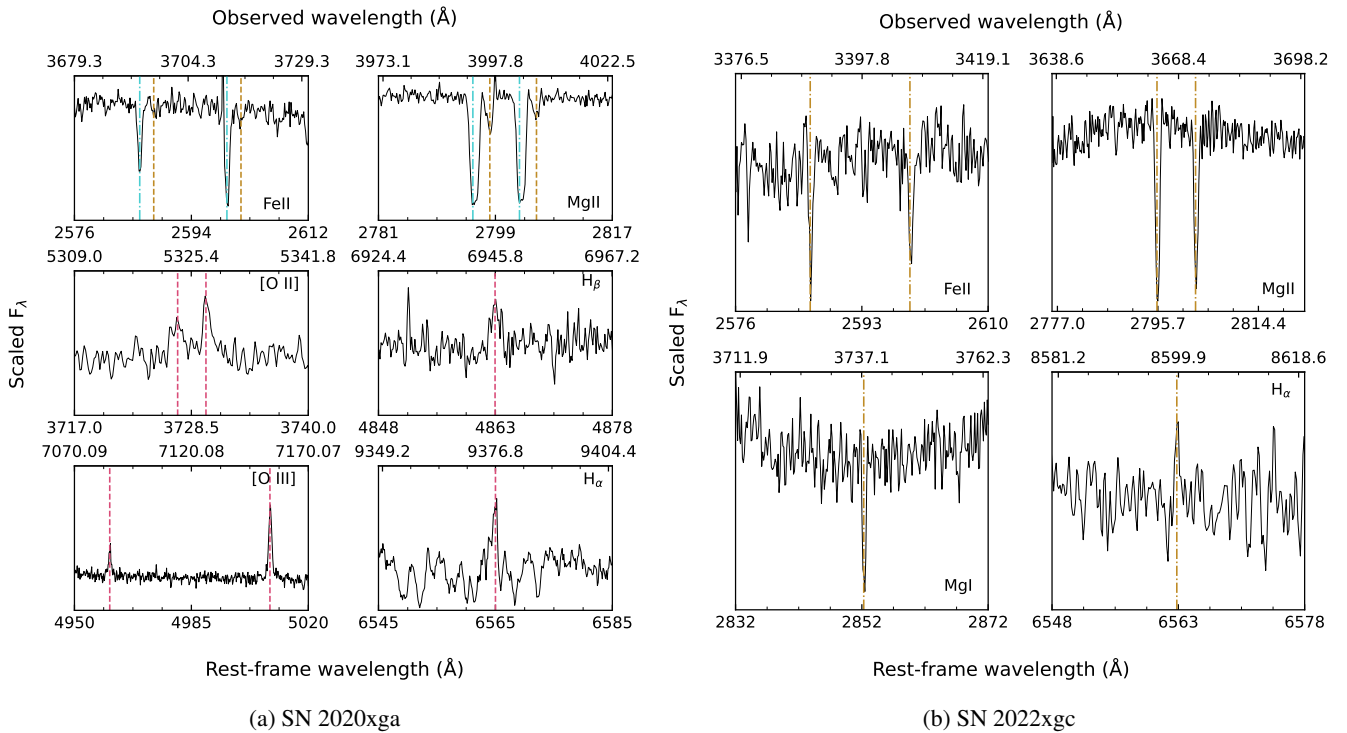


Fig. 8: Host galaxy absorption and emission lines in the X-shooter spectrum of SN 2020xga (left panel)  $-8.3$  days and SN 2022xgc (right panel)  $+21.9$  days after maximum light. The vertical lines illustrate the various redshift values of the galaxy lines. Left: In the spectrum of SN 2020xga the emission lines (red dashed line) give a consistent redshift of  $z = 0.4287$ , whereas the strong and the weak absorption lines indicate redshifts of  $z = 0.4283$  and  $z = 0.4296$ , respectively. Right: The host galaxy lines of SN 2022xgc agree on a redshift of  $z = 0.3103$ .

$\lambda\lambda 3727, 3729, H\beta \lambda 4861$ , forbidden [O III] doublet  $\lambda\lambda 4959, 5007$  and narrow  $H\alpha \lambda 6563$ . We found two galactic Fe II and Mg II absorption systems in the spectrum of SN 2020xga, with the stronger lines at a redshift of  $z = 0.4283 \pm 0.0002$  and the weaker lines at  $z = 0.4296 \pm 0.0002$ . In addition, the host's emission lines are consistent with a redshift of  $z = 0.4287 \pm 0.0001$ . Throughout the paper, we chose the redshift of SN 2020xga, as the higher value, and hence we assumed  $z = 0.4296$ . We further discuss this implication in Sect. 6.

The host galaxy lines displayed in the spectrum of SN 2022xgc are the narrow Fe II doublet  $\lambda\lambda 2586, 2600$ , the Mg II doublet  $\lambda\lambda 2796, 2803$ , the Mg I  $\lambda 2852$  and  $H\alpha \lambda 6563$ . These lines support a redshift of  $z = 0.3103 \pm 0.0001$  for SN 2022xgc.

#### 4.2. Spectroscopic sequence

Figure 9 depicts the spectral evolution from  $-9$  to  $+37.8$  rest-frame days past maximum brightness of SN 2020xga and from  $-0.7$  to  $+92.1$  rest-frame days of SN 2022xgc from  $2500 \text{ \AA}$  up to  $\sim 10\,000 \text{ \AA}$ . All spectra were taken during the photospheric phase. As the ejecta cools down, the spectra of both SN 2020xga and SN 2022xgc begin to resemble those of typical Type Ic SNe which is expected for SLSNe-I (Gal-Yam 2019a).

To identify the spectral lines in SN 2020xga and SN 2022xgc we used the medium-resolution X-shooter spectra due to their high S/N. For SN 2020xga, the spectra at  $-8.3$  and  $+37.8$  days were utilized, and for SN 2022xgc, we used those at  $+21.9$  and  $+92.1$  days. The line identification was done by comparing the spectra with well-studied SLSNe-I from the literature (e.g., Quimby et al. 2011; Inserra et al. 2013; Nicholl et al. 2015b; Quimby et al. 2018; Gal-Yam 2019b), by modeling the

earlier spectra at  $-8.3$  days and  $+21.9$  days (for SN 2020xga and SN 2022xgc, respectively) using the synthesis code SYN++ (Thomas et al. 2011) and finally by searching the National Institute of Standards and Technology (NIST; Kramida et al. 2022) atomic spectra database for lines above a certain strength, similar to what was done in Gal-Yam (2019b). Figure 10 depicts the X-shooter spectra of SN 2020xga and SN 2022xgc along with the most prominent features blueshifted by  $6000 - 8000 \text{ km s}^{-1}$  to match the absorption lines (see Sect. 4.3). The Ca H &  $\kappa$  and Mg I] lines in the spectra at  $+37.8$  days and  $+92.1$  days are shown at zero rest-frame velocity. The SYN++ modeling of the  $-8.3$  day phase spectrum of SN 2020xga and the  $+21.9$  day phase spectrum of SN 2022xgc can be found in Fig. E.1 in the Appendix, while Table E.1 collects the best-fit parameter values obtained by the modeling.

In the early spectrum of SN 2020xga, SYN++ tentatively identify the strong W-shape feature between  $3500 - 5000 \text{ \AA}$  with the O II  $\lambda 4358$  and  $\lambda 4651$  that characterise the spectra of numerous SLSNe-I. A small contribution of C II might be present at the troughs of  $4300$  and  $4550 \text{ \AA}$ . Comparison with other SLSNe-I showed that the absorption trough at  $4300 \text{ \AA}$  is most likely a blend of Fe III  $\lambda 4432$  and O II  $\lambda 4357$ . Redward of the O II lines, the Fe II  $\lambda 4923$  and  $\lambda 5169$  are present, but the Fe II  $\lambda 4923$  falls into the telluric band and the Fe II  $\lambda 5169$  is likely mixed with Fe III  $\lambda 5129$  (Liu et al. 2017). Above  $5000 \text{ \AA}$  the early spectrum of SN 2020xga does not show any obvious feature. Blueward of  $3500 \text{ \AA}$  a number of features are visible, but owing to severe blending the identification is challenging. The trough at  $2670 \text{ \AA}$  is associated with Mg II as seen in other SLSNe-I and the trough at  $\sim 2880 \text{ \AA}$  has been observed in a number of SLSNe (e.g.



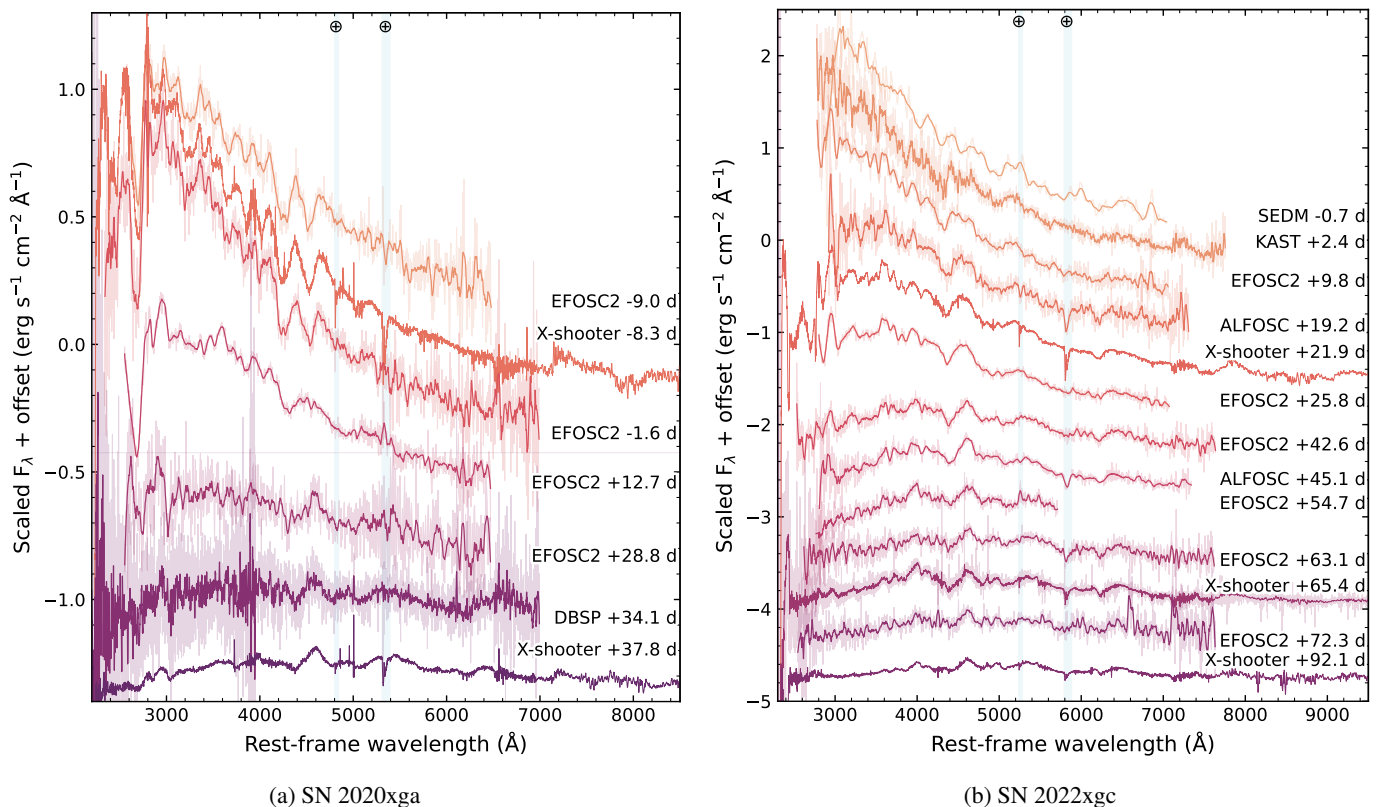


Fig. 9: Spectral sequence of SN 2020xga (left panel) from  $-9$  to  $+37.8$  rest-frame days and SN 2022xgc (right panel) from  $-0.7$  to  $+92.1$  g-band rest-frame days. An offset in flux was applied for illustration purposes. The spectroscopic measurements have undergone absolute flux calibration to align with the photometric data. The spectra are corrected for MW extinction and are smoothed using a Savitzky-Golay filter. The original data are presented in lighter colors. Regions of strong atmospheric absorption are blue-shaded.

Vreeswijk et al. 2014; Quimby et al. 2018; Gkini et al. 2024) and has been suggested by a few studies (Dessart et al. 2012; Mazzali et al. 2016; Quimby et al. 2018; Gkini et al. 2024) to have some contribution from Ti III, Fe III, Si III, C II and Mg II. Searching NIST, we discovered that the absorption at  $3200 \text{ \AA}$  could be attributed to Fe II  $\lambda 3325$  and Fe III  $\lambda 3305$ . The feature at  $3410 \text{ \AA}$  may be related with Fe II  $\lambda 3500$ .

In the spectrum of SN 2022xgc at  $+21.9$  days the major ions that are securely identified by SYN++ are Fe II, Si II and Ca II. Comparison with other SLSNe-I revealed that the absorption trough at  $2670 \text{ \AA}$  is due to Mg II. The absorption component at  $2880 \text{ \AA}$  is stronger than what is seen in SN 2020xga and similar to the one observed in the SLSN-I SN 2020zbf (Gkini et al. 2024). As previously stated, this component is likely a contribution of multiple elements, including Mg II. Searching the NIST, we identified some plausible contribution of Fe II between  $3000$  and  $3600 \text{ \AA}$  although the high level of blending makes this identification dubious. Additional Mg II  $\lambda 4481$  may be present in the absorption feature at  $4300 \text{ \AA}$ . Absorption from O II between  $3500 - 5000 \text{ \AA}$  as seen in many SLSN-I spectra around peak, is not present. Similarly to the case of SN 2020xga, we were unable to identify any line beyond  $6500 \text{ \AA}$  in the spectrum of SN 2022xgc owing to low S/N.

The spectra of SN 2020xga at  $+37.8$  days and SN 2022xgc at  $+92.1$  days resemble the spectra of a SN Ic at maximum light (Pastorello et al. 2010; Quimby et al. 2011). Both objects show Ca II  $\lambda 3966, 3934$  (though in SN 2020xga the emission

line is weak), Mg II  $\lambda 4481$ , Mg I  $\lambda 4571$ , and strong Fe II lines between  $4000$  and  $5200 \text{ \AA}$  blueshifted by  $7500 \text{ km s}^{-1}$  (see Sect. 4.3) to match the absorption component. In SN 2022xgc, the strong absorption trough at  $6230 \text{ \AA}$  is connected with Si II  $\lambda 6355$ , whereas in SN 2020xga, Si II may contribute to the weak absorption component at  $6230 \text{ \AA}$ . The contribution of the O I triplet  $\lambda 7772, 7774, 7775$  in the spectra of SN 2020xga and SN 2022xgc might be visible at  $7580 \text{ \AA}$ , however owing to the low S/N, this identification is uncertain.

### 4.3. Ejecta velocities

The ejecta velocities of SLSNe-I and their evolution can be measured from the O II absorption lines at  $3500 - 5000 \text{ \AA}$  at early phases (Quimby et al. 2018; Gal-Yam 2019b,a) and from the Fe II triplet  $\lambda 4923, 5018, 5169$  (Branch et al. 2002; Nicholl et al. 2015a; Modjaz et al. 2016; Liu et al. 2017). In SN 2020xga, the O II lines with the most noticeable characteristic, the W-shape, are present from  $-9$  to  $-1.6$  days. The absorption troughs of O II are shifted by  $-8000 \text{ km s}^{-1}$  and the velocity remains constant throughout the seven-day period. Chen et al. (2023b), studying a sample of 77 SLSNe-I, estimates the median O II velocity of the ZTF sample to be  $9700 \text{ km s}^{-1}$ . To report a dispersion in this value we bootstrapped the 41 SLSNe-I from the ZTF sample with O II velocities within  $\pm 30$  days post maximum light and propagated the measurement uncertainties with a Monte Carlo simulation. This process resulted in a median velocity of the ZTF-I sample of  $9794^{+3106}_{-2804} \text{ km s}^{-1}$ . Our estimated value of

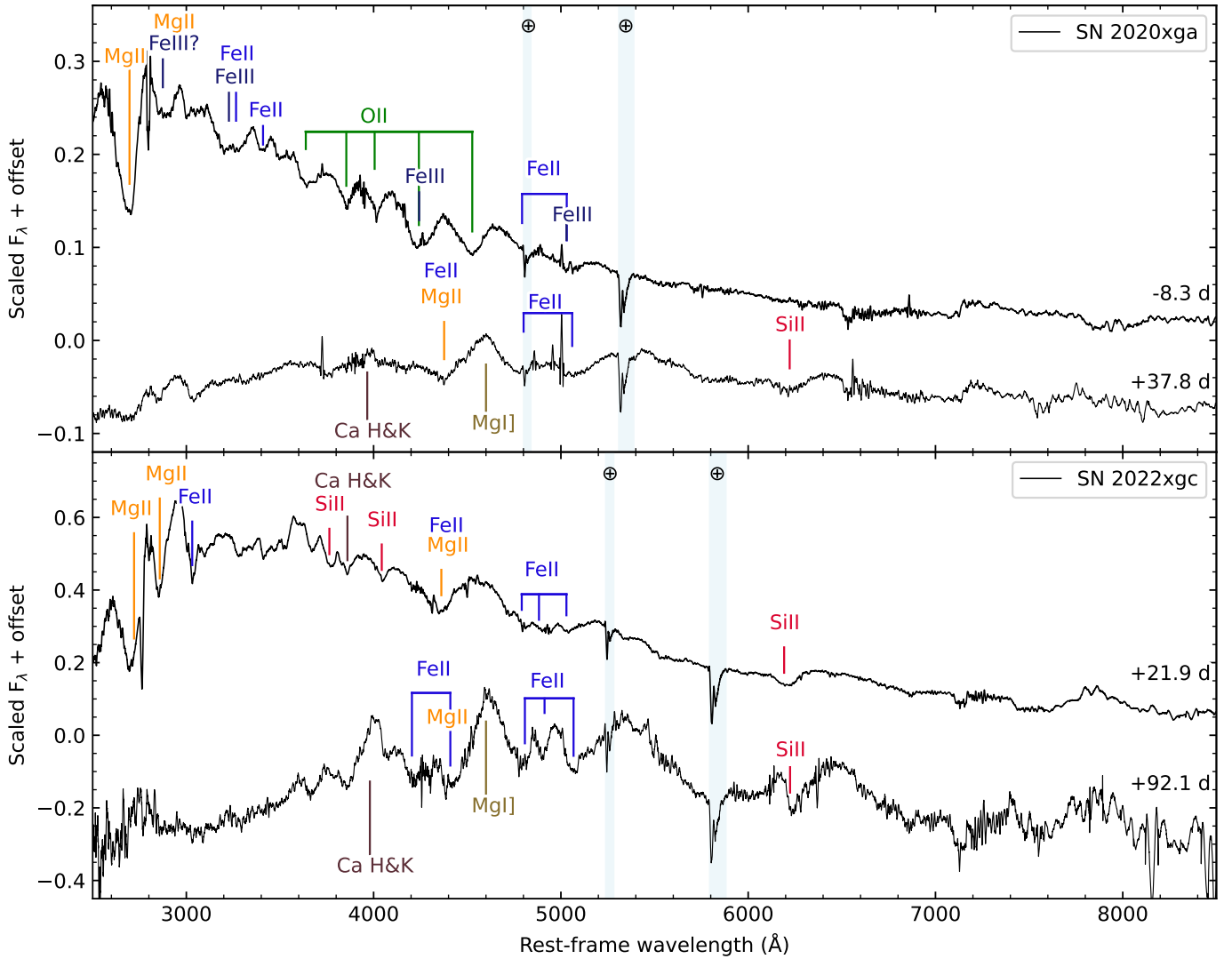


Fig. 10: X-shooter spectra of SN 2020xga (upper panel) at  $-8.3$  and  $+37.8$  days and SN 2022xgc (lower panel) at  $+21.9$  and  $+92.1$  days after maximum light. The spectra are corrected for MW extinction and are smoothed using a Savitzky-Golay filter. The original spectra are shown in lighter grey. The most conspicuous features are labeled. Uncertain line identifications are denoted with question marks. The ions beneath the spectrum are shown at  $v = 0$ , whilst those above have been shifted to match the absorption component. The light blue regions represent the telluric absorptions.

$8000 \text{ km s}^{-1}$  for SN 2020xga is lower than the median but it is in the range of the velocities of SLSNe-I. In SN 2022xgc, the O II lines are not clearly visible in the early spectra, therefore we cannot determine the ejecta velocity using the O II ion.

The second method for measuring the photospheric velocity and following its evolution is to use the Fe II triplet as tracer (Branch et al. 2002; Nicholl et al. 2015a; Modjaz et al. 2016; Liu et al. 2017). In Fig. 11, a zoomed-in view of the Fe II triplet region at  $-8.3$  and  $+37.8$  days post-maximum for SN 2020xga and at  $+21.9$ ,  $+65.4$ , and  $+92.1$  days post-maximum for SN 2022xgc is shown; we used the high-quality X-shooter spectra since the low S/N of the low-resolution spectra prevent us from tracking the velocity evolution. In SN 2020xga two absorption lines are visible that we identified as Fe II  $\lambda 4923$  and Fe II  $\lambda 5169$ . Since the Fe II  $\lambda 4923$  suffer from telluric absorption, we utilised the Fe II  $\lambda 5169$  line to estimate the photospheric velocities. In the X-shooter spectrum at  $-8.3$  days after peak, the marked absorption components match well with the Fe II triplet blueshifted by

$\sim 8000 \text{ km s}^{-1}$  despite the Fe II  $\lambda 4923$  being veiled by tellurics. We note that this value may be underestimated due to contamination with Fe III  $\lambda 5129$ . The resulting velocity from the Fe II lines is in agreement with the velocity estimated from the O II ion and the absorption components of other identified elements, e.g. Fe III. The strong features at  $4770$  and  $5045 \text{ \AA}$  in the spectrum at  $+37.8$  days suggest that the Fe II  $\lambda 4923$  and  $\lambda 5169$  may be blueshifted by  $\sim 7500 \text{ km s}^{-1}$ , which would result in a relatively constant velocity over a period of 50 days seen also in other SLSNe-I (Nicholl et al. 2013, 2015a, 2016; Liu et al. 2017).

In Fig. 11, in the spectrum of SN 2022xgc we resolved three absorption lines that we identify as Fe II  $\lambda\lambda 4924, 5018, 5169$ . At  $+21.9$  days the troughs match with a photospheric velocity of  $\sim 8100 \text{ km s}^{-1}$ , though the mismatch of the absorption at  $4940 \text{ \AA}$  can be explained by a blend of Fe II with other ions. The triplet is better resolved in the spectra at  $+65.4$  and  $+92.1$  days and the velocity decreases by  $\sim 1000 \text{ km s}^{-1}$  within 70 days.

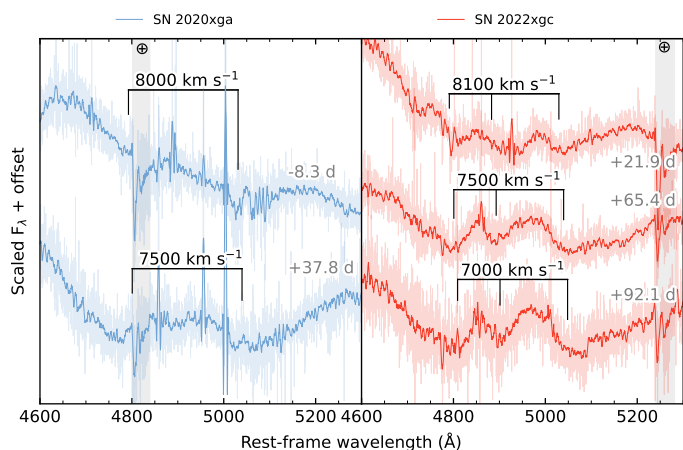


Fig. 11: Fe II triplet  $\lambda\lambda 4923, 5018, 5169$  region of SN 2020xga (left panel) at  $-8.3$  and  $+37.8$  day spectra and SN 2022xgc at  $+21.9, +65.5$  and  $+92.1$  days spectra. A normalization and an arbitrary offset has been applied for illustration purposes. The spectra have been smoothed using the Savitzky-Golay filter and the original data are shown in lighter colors. The absorption features that correspond to the blueshift of the Fe II lines are denoted along with the velocities.

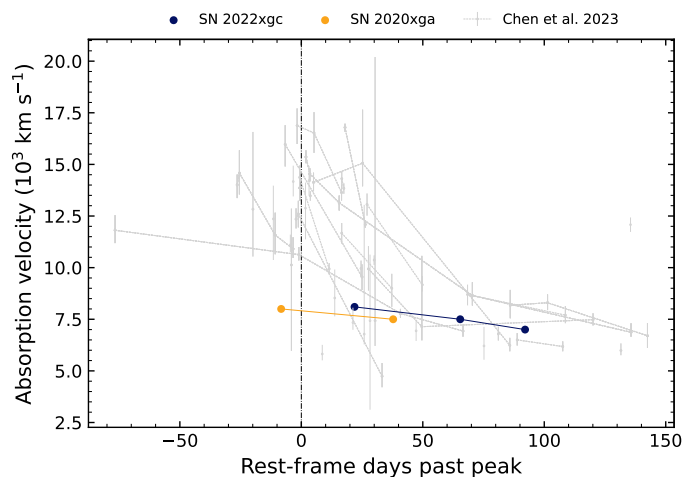


Fig. 12: Fe II ejecta velocities of SN 2020xga and SN 2022xgc as measured from the X-shooter spectra as a function of time. The velocity evolution of the ZTF SLSNe-I sample is shown in grey for comparison. The dashed-dotted vertical line illustrates the phase of the maximum light.

To compare these values with the ZTF sample, we plot in Fig. 12 the velocity evolution of 38 ZTF SLSNe-I with Fe II velocities, together with the velocity evolution of SN 2020xga and SN 2022xgc. The value of  $\sim 8000 \text{ km s}^{-1}$  measured from the pre-peak spectrum of SN 2020xga is lower than what we find in the ZTF sample, but not unprecedented since there are at least two SLSNe within  $\pm 20$  days after peak in the ZTF sample with Fe II velocities close to  $8000 \text{ km s}^{-1}$ . In SN 2022xgc, the first measurement of the photospheric velocity is derived from the spectrum at  $+21.9$  days following the peak. At this phase, the estimated value of  $8100 \text{ km s}^{-1}$  is within the velocity range of the ZTF sample at similar phases but lower than the bulk of the

population. Both objects appear to evolve slower than the ZTF sample.

#### 4.4. Comparison with other SLSNe-I

In Sect. 3.1 we compared the photometric properties of SN 2020xga and SN 2022xgc with the homogeneous ZTF sample (Chen et al. 2023a) and found that the light curve characteristics of SN 2020xga and SN 2022xgc are either average or span across the entire distribution, aside being very bright. However, SN 2020xga and SN 2022xgc display a spectroscopic signature rarely seen in SLSNe-I spectra and thus, we seek to compare the spectra of SN 2020xga and SN 2022xgc with those of typical SLSNe-I.

In Fig. 13 (left) we compare the X-shooter spectra of SN 2020xga and SN 2022xgc at  $-8.3$  and  $+37.8$ , and  $+21.9$ ,  $+65.4$  and  $+92.1$  days after peak, respectively, with a sample of well-studied SNe from the literature including PTF09cnd (Quimby et al. 2011, 2018), LSQ12dlf (Nicholl et al. 2014) and SN 2015bn (Nicholl et al. 2016). As previously indicated, the pre-peak spectrum of SN 2020xga shows a strong O II series, similar to the one found in PTF09cnd, albeit the absorption components in PTF09cnd are shifted to higher velocities compared to the ones in SN 2020xga. The O II lines are also seen in the spectrum of SN 2015bn at the same phase as the pre-peak spectrum of SN 2020xga, although they are weaker than for SN 2020xga and PTF09cnd. The O II lines are not clearly seen in the spectra of SN 2022xgc and LSQ12dlf during the early photospheric phase which could be explained by the fact that the conditions for O II excitation may not be satisfied (e.g., Mazzali et al. 2016; Dessart 2019; Könyves-Tóth 2022; Saito et al. 2024).

As the ejecta cool, the spectra of SN 2020xga and SN 2022xgc become similar to those of Type Ic SNe at maximum, as anticipated for the typical SLSNe-I. Overall, the general shape of the spectra of SN 2020xga and SN 2022xgc both pre- and post-peak are similar to the spectra of typical SLSNe-I and do not present any unusual spectral properties aside the second narrow Mg II absorption system in the UV part of the spectrum which is further discussed in Sect. 5. We note that in the spectra of SN 2020xga and SN 2022xgc more features are resolved than often seen in spectra of typical SLSNe-I, due to the high signal and good resolution of the X-shooter data.

In Fig. 13 (right), we compare the X-shooter spectra of SN 2020xga and SN 2022xgc with the spectra of SN 2018ibb and iPTF16eh at similar phases. SN 2020xga is the only object in this class that displays strong O II lines; the O II W-shape appears to be present in iPTF16eh but weaker than in SN 2020xga. In the spectra of SN 2022xgc and SN 2018ibb the Fe II triplet is resolved though the Fe II  $\lambda 5018$  in the spectrum of SN 2022xgc at  $+21.9$  days does not align with the absorption component. In contrast to SN 2020xga and iPTF16eh, which do not exhibit any obvious feature in the red part of the optical spectrum in the spectra near peak, both SN 2022xgc and SN 2018ibb show strong Si II  $\lambda 6355$ . As the temperature drops and elements from deeper inside are revealed, the spectra of all these objects become similar to those of standard Type Ic SNe. However, SN 2018ibb (Schulze et al. 2024) develops features such as [O II], [O III] and [Ca II] at the early photospheric phase that are not common for SNe. The spectroscopic peculiarity along with the outstanding light curve timescales make SN 2018ibb a unique SLSNe-I which stands out even among the SLSNe-I that display the rare signature of the second Mg II system (Schulze et al. 2024).



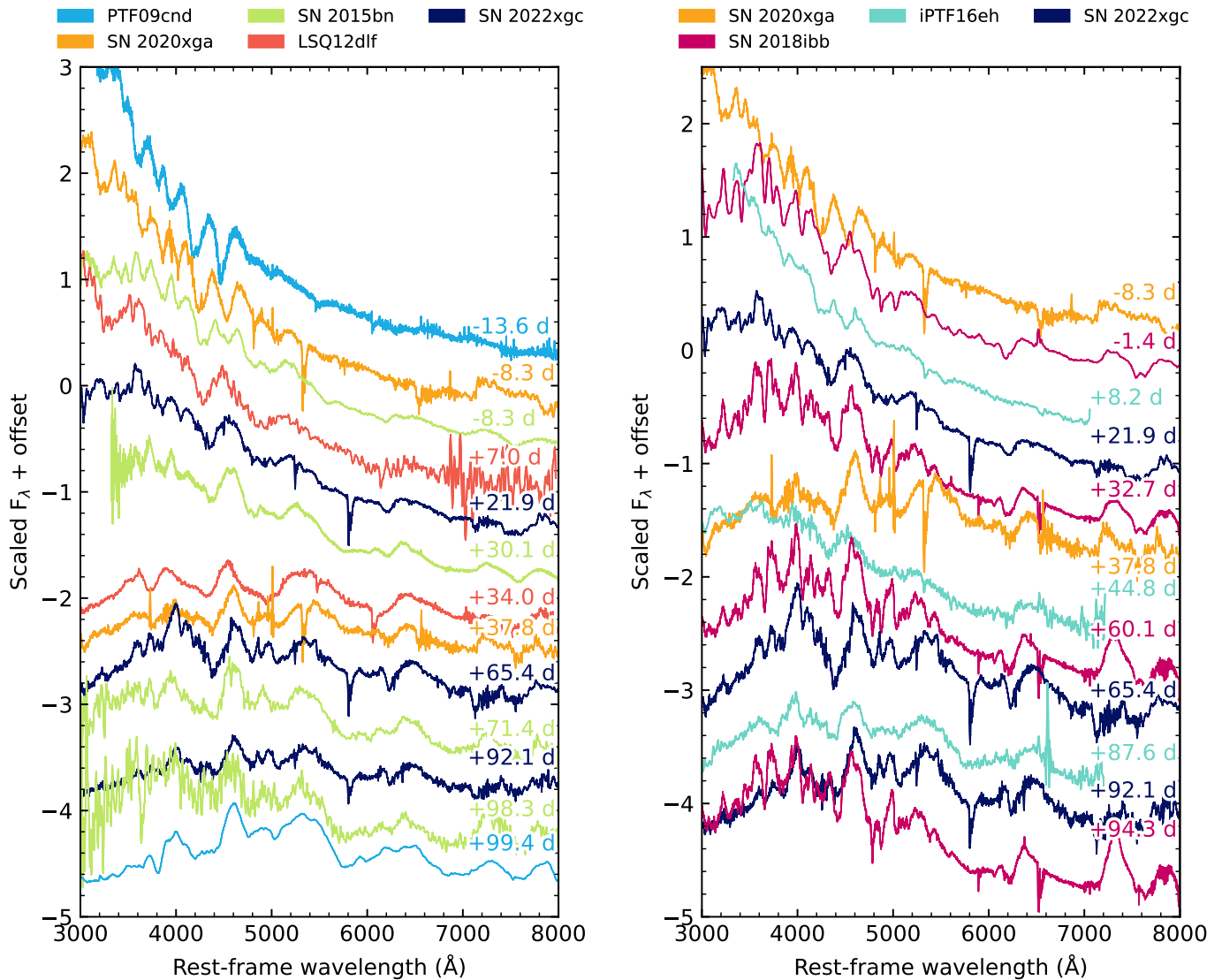


Fig. 13: Spectral comparison of SN 2020xga and SN 2022xgc with SLSNe-I from the literature. Left: Comparison of SN 2020xga and SN 2022xgc spectra with typical well-studied SLSNe-I at similar epochs. Right: SN 2020xga and SN 2022xgc spectra in comparison with SLSNe-I that display the second narrow Mg II absorption system. All spectra are corrected for MW extinction and have been smoothed using a Savitzky-Golay filter.

## 5. CSM shell around SN 2020xga and SN 2022xgc

### 5.1. Modeling of the Mg II absorption lines

The X-shooter spectra of SN 2020xga and SN 2022xgc at  $-8.3$  and  $+21.9$  days, respectively, show two Mg II absorption systems. In Fig. 14 a zoom-in region around the Mg II lines at  $\sim 2800$  Å of SN 2020xga and SN 2022xgc is presented in velocity space. The narrow Mg II systems at zero rest-frame velocity originate from the ISM of the host galaxies and are used for the determination of the SN redshift (see Sect. 4.1). The blueshifted Mg II systems are significantly broader ( $270$  km s $^{-1}$  for SN 2020xga and  $500$  km s $^{-1}$  for SN 2022xgc) than expected for the ISM in dwarf host galaxies (Krühler et al. 2015; Arabsalmani et al. 2018) but also narrower compared to the SN features ( $> 1000$  km s $^{-1}$ ) and such lines have been associated with the existence of a rapidly expanding CSM shell expelled a few years before the SN explosion in iPTF 16eh (Lunnan et al. 2018b).

To estimate the distance and the thickness of the CSM shell we modeled the line profile of the Mg II doublet using a modified Monte Carlo scattering code. While the line profile from a spherically symmetric shell for a single scattering line can be calculated analytically (Fransson 1984), the doublet nature of the Mg II lines will cause scattering from the blue component by the red component which affects the line profiles. We therefore used a Monte Carlo code to model the line profile. We assumed that the photons around  $2800$  Å produced in the SN “photosphere” are scattered in random directions from an expanding spherical shell with an inner radius of  $R_{\text{in}}$  and an outer radius of  $R_{\text{out}}$ . In reality, the background “continuum” is produced by lines from the expanding ejecta, most likely dominated by the broad Mg II lines (Sect. 4). We assumed that this continuum is given by the observed spectrum at velocities larger than that of the shell, and adjusted the background spectrum so that the total spectrum, “continuum” plus the scattered emission from the shell agreed with the observations. At the absorption of the shell, the “con-

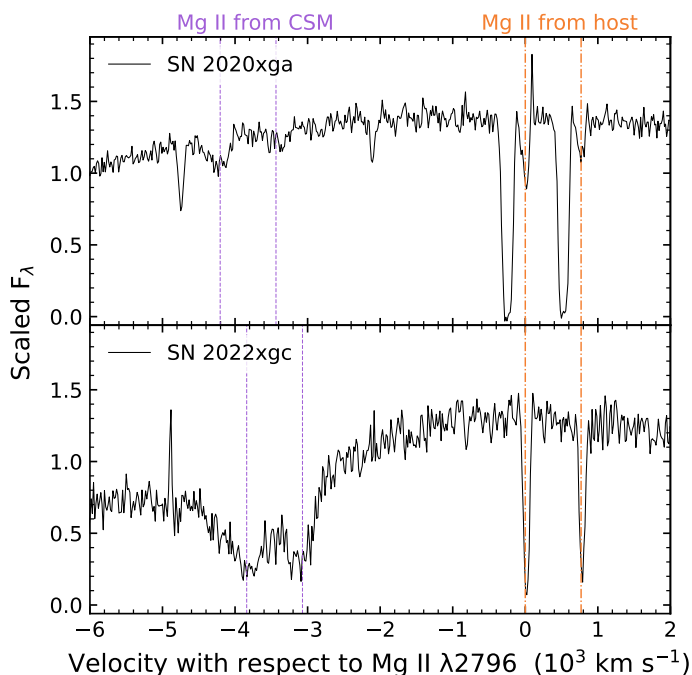


Fig. 14: X-shooter spectra of SN 2020xga at  $-8.3$  days (top panel) and SN 2022xgc at  $+21.9$  days (bottom panel). The spectra show resolved, narrow absorption lines from the host ISM (marked by the dashed, orange vertical lines) and a blueshifted absorption line system (marked by the dashed, purple vertical lines) from a CSM shell expelled shortly before the SN explosion.

tinium” flux was simply interpolated. Because there is no indication of thermal emission from the shell (contrary to the case of iPTF 16eh, Lunnan et al. 2018b) we neglected collisional excitation for the line profile.

We assumed that the expansion of the shell is homologous with  $V = V_{\max}(r/R_{\text{out}})$ , which is reasonable for a time-limited eruption, such as PPI or LBV eruptions. This configuration gives rise to the second Mg II system from the shell, which we observe as an emission and/or absorption lines on top of the SN photospheric flux. We did not include scattering by the thermal motions of the electrons, as the electron scattering depth of the shell should be small.

We assumed that the CSM is mainly characterised by an optical depth  $\tau$  of the shell. In the Sobolev approximation (Sobolev 1957) this is for a homologous expansion given by

$$\tau = \frac{g_2 \lambda^3 A_{21} n_1 t}{8\pi g_1}. \quad (5)$$

Here  $A_{21} = 2.8 \times 10^8 \text{ s}^{-1}$  is the transition rate between the upper level 2 and lower level 1,  $n_1$  is the number density in the ground state,  $\lambda$  the wavelength,  $g_1 = 2$  and  $g_2$  the statistical weights of the lower and upper levels, respectively and  $t$  the time from the eruption. For the  $2795.5 \text{ \AA}$  line  $g_2 = 4$  and for the  $2802.7 \text{ \AA}$  line  $g_2 = 2$ . The relative depth of the blue and red Mg II doublet can be used to determine the optical depth. In the optically thin limit this ratio is 2.0, decreasing as the optical depth increases.

The velocity range of the absorption from the shell gives a direct measure of the radial extent of the shell. For a homologous expansion of the shell and for a single line the minimum,  $V_{\text{blue}}$

and maximum,  $V_{\text{red}}$ , velocity of the absorption is given by

$$V_{\text{blue}} = -V_{\text{max}}$$

$$V_{\text{red}} = -V_{\text{max}} \left( \frac{R_{\text{in}}}{R_{\text{out}}} \right)^\alpha \left[ 1 - \left( \frac{R_{\text{phot}}}{R_{\text{in}}} \right)^{2\alpha} \right]^{1/2} \quad (6)$$

For homologous expansion  $\alpha = 1$  and for a constant velocity shell  $\alpha = 0$ . Determining the maximum and minimum velocities of the absorption we can therefore estimate the  $R_{\text{in}}$  and  $R_{\text{out}}$  of the shell relative to the photospheric radius. Note that the minimum velocity of the shell is *not*  $-V_{\text{red}}$ , but  $V_{\text{in}} = R_{\text{in}}/t$ . While we have here assumed homologous expansion, a shell with constant velocity only differs marginally in a slightly lower velocity unless the shell is very broad. The absorption line profile, however, differs from the homologous, lacking a flat bottom at the minimum absorption and instead being more V-shaped (see e.g. Figs. 4 and 5 in Fransson 1984). The observed absorption profiles for SN 2022xgc (Fig. 14) argue against a constant velocity shell, but is compatible with a homologous expansion. This is also the case for SN 2020xga (Fig. 14) and SN 2018ibb (see Sect. 5.2), although the S/N makes this conclusion marginal.

For homologous expansion Eq. 6 can be inverted to show that

$$\frac{R_{\text{in}}}{R_{\text{out}}} = \left[ \left( \frac{V_{\text{red}}}{V_{\text{blue}}} \right)^2 + \left( \frac{R_{\text{phot}}}{R_{\text{out}}} \right)^2 \right]^{1/2} \quad (7)$$

The relative thickness of the shell, and therefore the depth of the absorption, decreases as the radius of the shell increases. The depth of the absorption therefore provides a constraint on the radius of the shell.

Figure 15 shows the observed data for SN 2020xga and SN 2022xgc around the  $2800 \text{ \AA}$  region along with the modeled Mg II line profiles. For SN 2020xga there is good agreement between the model and the observations for  $R_{\text{in}} = 2.96 R_{\text{phot}}$  and  $R_{\text{out}} = 3.00 R_{\text{phot}}$ , where  $R_{\text{phot}}$  is the photospheric radius, and  $V_{\text{max}} = 4275 \text{ km s}^{-1}$ . Using the blackbody radius we derived in Sect. 3.2 from the given observed spectrum, we estimate that the CSM shell is located at  $1.29 \times 10^{16} \text{ cm}$  and extends to  $1.38 \times 10^{16} \text{ cm}$ . The emission from the CSM shell is weak and consistent with the SN continuum. Given the derived size of the shell and the estimated maximum velocity of  $4275 \text{ km s}^{-1}$ , the shell was expelled  $\sim 11$  months before the core-collapse, assuming a constant shell velocity as seen in the case of SN 2018ibb.

In SN 2022xgc the best fit model is for a CSM shell with properties of  $R_{\text{in}} = 1.8 R_{\text{phot}}$ ,  $R_{\text{out}} = 2.0 R_{\text{phot}}$ ,  $V_{\text{max}} = 4400 \text{ km s}^{-1}$ . This leads to a shell extending from  $\sim 7.95 \times 10^{15} \text{ cm}$  to  $\sim 8.84 \times 10^{15} \text{ cm}$ . Contrary to SN 2020xga, the emission from the CSM shell in SN 2022xgc is well above the SN continuum (dashed, red line) and contributes significantly to the shape of the output spectra around the  $2800 \text{ \AA}$  region. This is a result of the considerably broader CSM shell, which scatter a larger fraction of the photons outside the absorption lines. Utilising the maximum velocity of  $4400 \text{ km s}^{-1}$  calculated by the absorption minima of the broad Mg II lines and assuming that the shell has not been decelerated, we estimate the time of CSM ejection to be  $\sim 5$  months before the SN explosion.

The relative depth of the blue and red Mg II doublet in SN 2020xga indicate an optical depth of  $\tau \approx 0.5$ . Using  $\Delta r = (V_{\text{out}} - V_{\text{in}})t$  for a homologous shell one finds for the column density of Mg II,  $N = n_1 \Delta r$ ,

$$N = 2.2 \times 10^{14} \left( \frac{V_{\text{max}}}{10^3 \text{ km s}^{-1}} \right) \left( 1 - \frac{R_{\text{in}}}{R_{\text{out}}} \right) \tau \text{ cm}^{-2}, \quad (8)$$

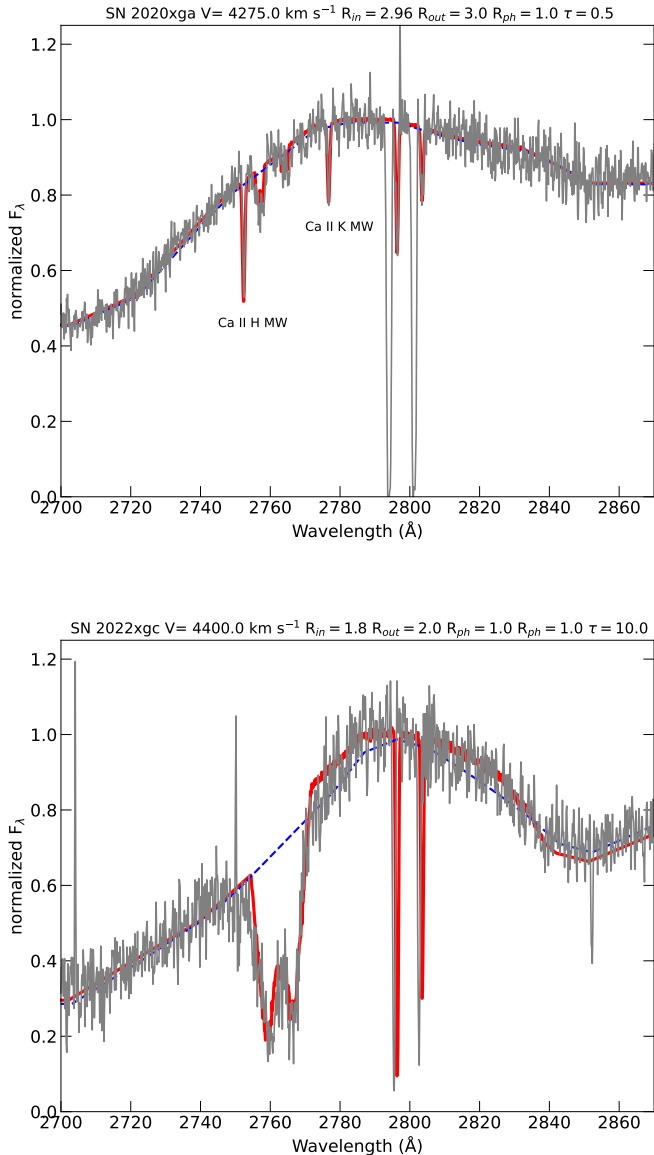


Fig. 15: Modeling on the Mg II doublets originating from the CSM shell (broad features) and the ISM of the host galaxy (narrow features) for SN 2020xga (top) and SN 2022xgc (bottom). The observed spectrum in the 2800 Å region is presented in grey and the best model fit is shown in red. The blue dashed line illustrates the SN continuum. For SN 2020xga we have marked the Ca H & K lines from the MW.

valid also for large  $\tau$ . For SN 2020xga we find  $N(\text{Mg II}) \sim 4.7 \times 10^{12} \text{cm}^{-2}$ . The uncertainty in  $\tau$ , and therefore  $N(\text{Mg II})$ , is at least a factor of two. In the case of SN 2022xgc the lines are saturated with  $\tau > 5$  and we only find a lower limit of  $N(\text{Mg II}) > 4.7 \times 10^{14} \text{cm}^{-2}$ .

In both SN 2020xga and SN 2022xgc, the X-shooter spectra obtained at later epochs are very noisy in the UV part of the spectrum that we are interested in and any potential Mg II lines from the CSM shell cannot be resolved. Thus, we are not able to track the evolution of the Mg II line profiles which could provide a hint for the geometry of the shell. We note that for this part of the analysis we used only the spectra obtained through our X-

shooter program due to the high S/N and the particular sensitivity of the instrument in the bluer wavelengths.

## 5.2. Comparison with similar SLSNe-I

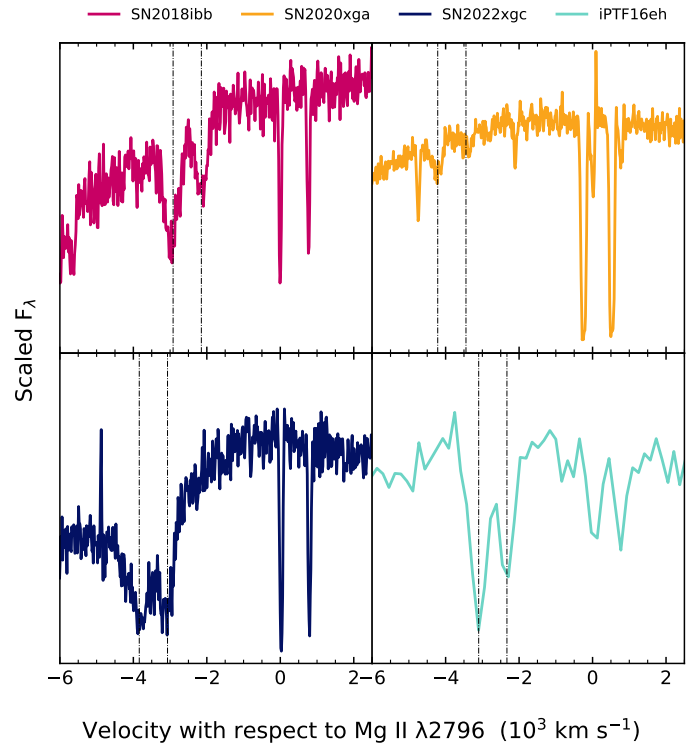


Fig. 16: Comparison of the broad Mg II lines originating from the CSM shells for SN 2020xga, SN 2022xgc, SN 2018ibb and iPTF 16eh. The spectra are corrected for MW extinction. The black vertical lines mark the velocity of the absorption minima of the secondary Mg II lines.

Figure 16 shows a zoom-in of the Mg II region of all the four objects that have shown the high velocity CSM absorption systems. The Mg II doublets originating from the CSM have various shapes and are shifted by various velocities reflecting the diversity of the CSM shells located around the SLSNe. In iPTF16eh the broad Mg II lines are blueshifted by  $3300 \text{ km s}^{-1}$  and in SN 2018ibb by  $2918 \text{ km s}^{-1}$  indicating shells moving somewhat slower but still comparable to the ones in SN 2020xga and SN 2022xgc. The Mg II doublet in SN 2020xga is shallower compared to the rest of the objects which argues for a CSM in SN 2020xga that is placed at larger radius with respect to its photosphere in comparison to the other three objects showing this signature in their spectra. On the other hand, the deep and blended Mg II lines in SN 2022xgc and iPTF16eh points towards broader CSM shells in comparison to SN 2020xga and SN 2018ibb. SN 2022xgc is the only object in which the Mg II lines are saturated and thus only a lower limit on the column density of Mg II can be calculated.

Motivated by the above analysis for SN 2020xga and SN 2022xgc, we modeled the Mg II doublet line profile of SN 2018ibb (Schulze et al. 2024) using the X-shooter spectrum at +32.7 days after maximum to quantify the properties of the CSM shell (see Fig. 17). The best fit model is for a CSM shell with  $R_{\text{in}} = 2.00 R_{\text{phot}}$ ,  $R_{\text{out}} = 2.14 R_{\text{phot}}$  and  $V_{\text{max}} = 3200 \text{ km s}^{-1}$ . Using the photospheric-radius values reported in Schulze et al.



(2024), we calculated a shell extended from  $1.00 \times 10^{16}$  cm out to  $1.07 \times 10^{16}$  cm. Similarly to SN 2022xgc, the emission from the shell contributes significantly to the spectrum of SN 2018ibb around the 2800 Å region. Using Eq. 8 we estimated the column density of Mg II in the CSM shell of SN 2018ibb to be  $N(\text{Mg II}) \sim 9.2 \times 10^{13} \text{ cm}^{-2}$ , in agreement with the value derived in Schulze et al. (2024). Finally, we estimated the time of the CSM expelling to be < 9 months before the core-collapse given the high uncertainty of the explosion date in SN 2018ibb.

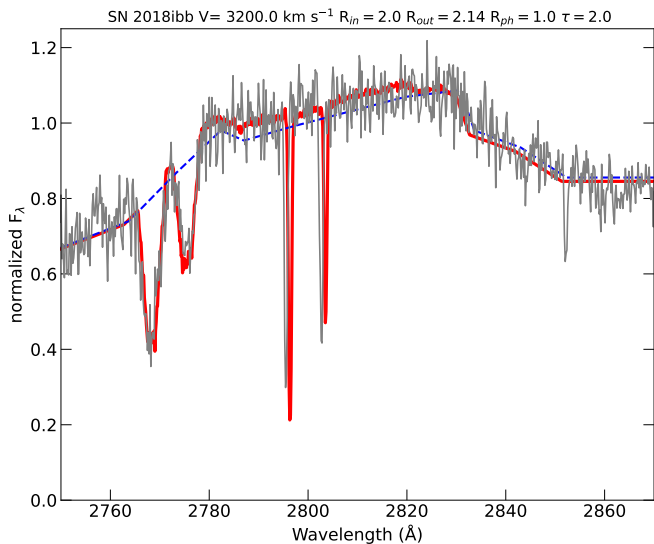


Fig. 17: Modeling on the Mg II doublets originated from the CSM shell (broad features) and the ISM of the host galaxy (narrow features) for SN 2018ibb. The observed spectrum at the 2800 Å region is presented in grey and the best model fit in red. The blue dashed line illustrates the SN continuum.

In iPTF16eh (Lunnan et al. 2018b, see their Fig. 1) an intermediate-width Mg II emission appeared at  $\sim 2800$  Å approximately 100 days after explosion and was persistent for more than 200 days. During this timescale, the line centroid was shifting from  $-1600 \text{ km s}^{-1}$  to  $2900 \text{ km s}^{-1}$  while the FWHM remained constant. This time- and wavelength-dependant emission line was associated with a resonance scattering light echo from a CSM shell. In the case of iPTF16eh, due to the low resolution spectrum, the Mg II scattered shell emission was modeled instead to estimate the size and the thickness of the CSM. Lunnan et al. (2018b) find that the shell is located at  $\sim 3.37 \times 10^{17}$  cm, extended out to  $\sim 3.55 \times 10^{17}$  cm and was expelled  $\sim 30$  years before explosion. The CSM radius of iPTF16eh is almost an order of magnitude higher than the one derived from the modeling of SN 2020xga and SN 2022xgc. The evolution of the emerging Mg II emission line in iPTF16eh was used as diagnostic for the geometry of the shell, which according to Lunnan et al. (2018b) is found to be roughly spherical. Motivated by this study, Schulze et al. (2024) analyzed the spectra of SN 2018ibb between +230 and +378 days after peak and detected Mg II in emission. However, due to heavy rebinning of the data, it is uncertain whether this emission line is connected with light echo from the CSM shell. In SN 2020xga and SN 2022xgc we do not observe any variable Mg II in emission thus we can not derive any conclusion about the geometry of the shell.

## 6. Host galaxy properties

### 6.1. Host galaxy of SN 2020xga

In Fig. 8 (left panel) two Mg II and Fe II absorption systems are resolved in the host galaxy of SN 2020xga. As discussed in Sect. 4.1, the stronger system is at  $z = 0.4283$  and the weaker one at  $z = 0.4296$ , with a velocity separation of  $\sim 260 \text{ km s}^{-1}$ . These two absorbing systems could arise either as a consequence of gas cloud motions (infall or outflows of gas) in the host galaxy or from a neighboring galaxy intervening in the line of sight (e.g. Ledoux et al. 2006; Chen 2012; Møller et al. 2013; Friis et al. 2015). Since the emission lines from the star-forming regions are centered on a redshift in between the absorption components ( $z = 0.4287$ ) and the velocity separation of  $\sim 260 \text{ km s}^{-1}$  is the typical difference in rotational velocity in a galaxy (Galbany et al. 2016), the scenario of mapping different regions of a single host galaxy is more likely (Friis et al. 2015).

The determination of the SN redshift in this case is not straightforward. Vreeswijk et al. (2014) showed that the absorbing gas responsible for the narrow lines in the spectrum of the SLSN iPTF 13ajg was produced by gas in the ISM located at least 50 pc from the SN. In addition, Friis et al. (2015), which presented a similar picture to SN 2020xga in terms of the lines of the GRB 121024A host galaxy, found that the absorbing clouds are not probing the actual GRB environment, but rather gas that has been photoionized by the GRB out to hundreds of parsecs. Although there are some distinctions between GRB and SLSN host galaxies (e.g. Vreeswijk et al. 2014; Lunnan et al. 2014; Ørum et al. 2020), both are tracers of star formation, and therefore the assumption that the SN redshift is same as the the redshift of the emission lines would not be unreasonable. Alternatively, to break the redshift degeneracy we would need high-resolution imaging and spectroscopy of the host galaxy to resolve the morphology of the galaxy and to infer the SN location and measure the redshift of that location. However, since analysing the host environment of SN 2020xga is out of the scope of this paper and the redshift values are different only in the third digit, we take as the redshift of the SN the highest value. We note that considering the redshift of the emission lines or the strong Mg II system would not affect our analysis and would not change significantly the results inferred from the CSM modeling.

### 6.2. Stellar population synthesis modeling

To infer the mass and star-formation rate of the host of SN 2020xga we model the observed spectral energy distribution built from the broad-band photometry (Table 1) and the measured emission lines (Table 4) with the software package PROSPECTOR (Johnson et al. 2021) version 1.1.<sup>15</sup> We assume a Chabrier IMF (Chabrier 2003) and approximate the star formation history [SFH] by a linearly increasing SFH at early times followed by an exponential decline at late times (functional form  $t \times \exp(-t/t_{1/e})$ , where  $t$  is the age of the SFH episode and  $t_{1/e}$  is the  $e$ -folding timescale). The model is attenuated with the Calzetti model (Calzetti et al. 2000). The priors of the model pa-

<sup>15</sup> PROSPECTOR USES THE FLEXIBLE STELLAR POPULATION SYNTHESIS [FSPS] CODE (Conroy et al. 2009) to generate the underlying physical model and PYTHON-FSPS (Foreman-Mackey et al. 2014) to interface with FSPS in PYTHON. The FSPS CODE ALSO ACCOUNTS FOR THE CONTRIBUTION FROM THE DIFFUSE GAS BASED ON THE CLOUDY MODELS FROM (Byler et al. 2017). WE USE THE DYNAMIC NESTED SAMPLING PACKAGE DYNESTY (Speagle 2020b) TO SAMPLE THE POSTERIOR PROBABILITY.

rameters are set identical to those used by Schulze et al. (2021). The observed SED is adequately described by a galaxy model with a stellar mass of  $\log M_*/M_\odot = 7.95^{+0.25}_{-0.26}$  and star-formation rate (SFR) of  $0.96^{+0.47}_{-0.26} M_\odot \text{ yr}^{-1}$  (grey curve in Fig. 18), leading to a specific SFR of  $10^{-8} \text{ yr}^{-1}$ . The values derived from the modeling of SN 2020xga are consistent with what is seen in the host galaxies of other SLSNe-I (Perley et al. 2016; Angus et al. 2019; Schulze et al. 2021).

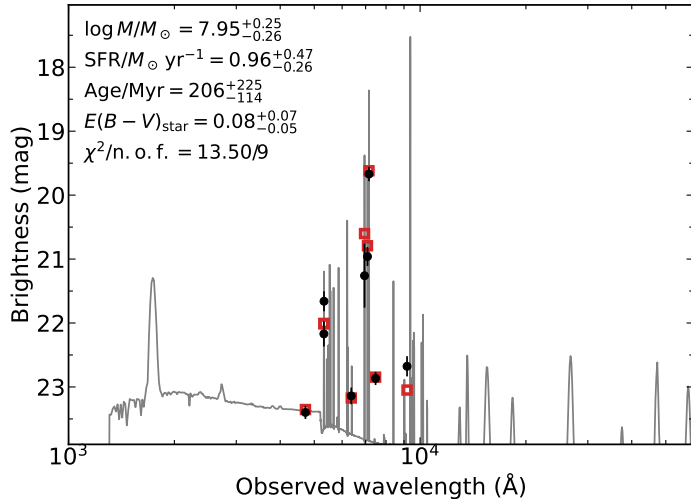


Fig. 18: Spectral energy distribution (SED) of the host galaxy of SN 2020xga (black data points). The solid line displays the best-fitting model of the SED. The red squares represent the model-predicted magnitudes. The fitting parameters are shown in the upper-left corner. The abbreviation ‘n.o.f.’ stands for the number of filters.

### 6.3. Emission line diagnostics

Using the narrow emission lines from the galaxy present in the X-shooter spectra of SN 2020xga at +37.8 days and SN 2022xgc at +21.9 days, we can derive some properties of the two SLSN hosts regarding their metallicity, star-formation rate and host galaxy extinction. After calibrating the spectra to the photometry and correcting for MW extinction, we measured the fluxes of the emission lines utilizing the python package LiME (Fernández et al. 2024). The resulting flux values are listed in Table 4.

Table 4: Observed host galaxy emission line fluxes of SN 2020xga and SN 2022xgc (corrected for MW extinction). For lines detected with a significance of  $< 3\sigma$ , we also report the  $< 3\sigma$  upper limits.

Line	SN 2020xga	SN 2022xgc
	Flux ( $10^{-17} \text{ erg s}^{-1} \text{ cm}^{-2}$ )	Flux ( $10^{-17} \text{ erg s}^{-1} \text{ cm}^{-2}$ )
[S II] $\lambda 6732$	$0.91 \pm 0.27$	–
[S II] $\lambda 6718$	$0.64 \pm 0.23 (< 0.69)$	–
[N II] $\lambda 6584$	$< 1.23$	–
H $\alpha$ $\lambda 6563$	$4.29 \pm 0.48$	$0.37 \pm 0.12$
[O III] $\lambda 5007$	$7.42 \pm 0.30$	–
[O III] $\lambda 4959$	$2.31 \pm 0.23$	–
H $\beta$ $\lambda 4861$	$1.87 \pm 0.70 (< 2.1)$	–
[O II] $\lambda 3729$	$3.06 \pm 0.30$	–
[O II] $\lambda 3727$	$1.91 \pm 0.28$	–

We used the Balmer decrement to measure the host galaxy extinction of SN 2020xga and found a value of  $H\alpha/H\beta = 2.3 \pm 0.9$ , which is consistent within the uncertainty with the theoretical ratio of 2.87 for no extinction (assuming Case B recombination and a temperature of 10,000 K; Osterbrock & Ferland 2006); thus we did not apply any host galaxy extinction correction to the SN 2020xga photometry. In the spectrum of SN 2022xgc only the H $\alpha$  line was detected, thus we cannot estimate the extinction of SN 2022xgc’s host.

The star-formation rate (SFR) can be derived from the luminosity of H $\alpha$  emission line using the Kennicutt (1998) relation and the relation from Madau & Dickinson (2014) to convert from the Salpeter to the Chabrier IMF in the Kennicutt (1998). This gives a SFR of  $0.24 \pm 0.03 M_\odot \text{ yr}^{-1}$  for SN 2020xga and  $0.009 \pm 0.003 M_\odot \text{ yr}^{-1}$  for SN 2022xgc assuming zero host extinction. The value for SN 2020xga is lower than what is inferred from the SED modeling but not unprecedented compared to what is seen among SLSN host galaxies, while the value for SN 2022xgc points toward a ultra-faint dwarf galaxy (e.g. Perley et al. 2016; Angus et al. 2016).

Since we do not detect the auroral line [O III]  $\lambda 4363$  in the spectrum of SN 2020xga, we are limited to strong-line metallicity diagnostics, such as R23, O3N2 or N2 (Pagel et al. 1979; Pettini & Pagel 2004; see discussion in Kewley & Ellison 2008). The O3N2 and N2 indexes require the [N II] line flux which evaded detection. Thus, we used the R23 index with the calibrations of Jiang et al. (2019), and the non-detection of [N II] to break the degeneracy. We calculated for SN 2020xga  $12 + \log(\text{O}/\text{H}) = 7.96^{+0.22}_{-0.18}$  dex. Taking the solar value to be  $12 + \log(\text{O}/\text{H})_\odot = 8.69$  dex (Asplund et al. 2021), this corresponds to a metallicity  $Z = 0.2 Z_\odot$ . The metallicity of SN 2020xga is in agreement with the values reported for other SLSN-I host galaxies ( $< 0.5 Z_\odot$ ; e.g., Lunnan et al. 2014; Leloudas et al. 2015; Perley et al. 2016; Chen et al. 2017; Schulze et al. 2018). We do not derive any metallicity measurement for the host of SN 2022xgc due to the lack of detection of emission lines originating from the host galaxy in the spectrum of SN 2022xgc.

## 7. Discussion

### 7.1. What is the origin of the CSM?

In Sect. 5 we modeled the broad Mg II lines in the spectra of SN 2022xgc and SN 2020xga originating from CSM shells located around the SNe. The question that we need to address is what process led to the ejection of the material that generated the CSM at this distance. Our findings indicate that this material was expelled less than a year before the core collapse in the final stages of stellar evolution, supporting a scenario of eruptive mass loss, since line-driven winds have much longer timescales than the evolutionary timescales at the post-MS phase.

One scenario to explain the detected CSM shells is the giant eruptions of LBV stars. The best observed example is the ‘‘Great Eruption’’ of  $\eta$  Carinae in 1843 in which  $12 - 20 M_\odot$  (or more; Smith et al. 2003) of material was ejected within a decade, moving at velocities between  $650 - 6000 \text{ km s}^{-1}$  (Davidson et al. 2001; Currie et al. 2002; Smith 2002; Smith & Morse 2004; Smith 2008). The geometry of ejecta-nebulae in LBV eruptions can be very anisotropic, as observed in  $\eta$  Carinae. Although the causes of LBV eruptions are still unknown, several theories have been proposed (e.g. Davidson 1987; Owocki et al. 2004; Smith et al. 2003; Smith 2006, 2008; Woosley 2017; Akashi & Kashi 2020; Cheng et al. 2024).

For iPTF16eh, Lunnan et al. (2018b) did not exclude an LBV-like eruption as a possibility for the formation of the CSM shell located around the SN. However, the spherically detached shell seen in iPTF16eh is not consistent with the asymmetric CSM structure may be expected in this type of eruption (see Fig. 1 in Smith 2008). Since in the spectra of SN 2022xgc and SN 2020xga the shell velocities of  $\sim 4000 \text{ km s}^{-1}$  are consistent with an LBV-related eruption and the geometry of the shells cannot be constrained (see Sect. 5), previous massive ejection like that in an LBV cannot be ruled out.

The LBV eruptions have also been discussed that could be driven by the PPI mechanism (Woosley 2017), which occurs for a He core in the mass range of  $30 - 65 M_{\odot}$  (Woosley et al. 2007). For the PPI, the primary parameter determining the duration between the shell ejections and the ultimate core collapse, as well as the expelled mass and their kinetic energy, is the mass of the He core  $M_{\text{He}}$  (Woosley 2017; Leung et al. 2019; Marchant et al. 2019). The time interval could range from a few hours up to 10 000 years. For  $M_{\text{He}} < 40 - 42 M_{\odot}$ , the energy released is insufficient to unbind significant amounts of material, resulting in multiple weak pulses (Woosley 2017; Renzo et al. 2020), whereas for  $M_{\text{He}} > 50 M_{\odot}$ , the time delay between strong pulses becomes long, forming shells at distances greater than the photospheric radius of the SN (Woosley 2017).

For SN 2020xga the CSM was estimated to be expelled  $\sim 11$  months before the SN explosion. This value corresponds to that of a pure He core of  $51 M_{\odot}$  with no rotation and zero metallicity in the study of Woosley (2017). Exploring the models of Woosley (2017) for the blue supergiant progenitors developed using the KEPLER code (Weaver et al. 1978; Weaver & Woosley 1993; Woosley et al. 2002), we found that the model best describing the observed CSM properties of SN 2020xga is the B105 model, with a remaining H envelope of  $10.8 M_{\odot}$ . The model ejected  $14.7 M_{\odot}$ , including the H envelope, with a kinetic energy of  $0.6 \times 10^{51} \text{ erg}$ . Assuming that the material in the B105 model has been ejected in one strong pulse  $\sim 2$  years before core-collapse, at the time of the detection, the shell is moving at  $\sim 2700 \text{ km s}^{-1}$  at a radius of about  $1.8 \times 10^{16} \text{ cm}$ . The shell velocity derived from Woosley (2017) model is substantially lower than our prediction, but its distance is comparable to our estimated value for SN 2020xga. The model B100, on the other hand, has slightly higher velocity, but at the moment of detection, the shell is four times closer to the SN than in our model.

The discrepancy between the observed properties and the Woosley (2017) models may be due to our assumption that the material was ejected in a single pulse which is unlikely for these stellar masses (see Table 1 in Woosley 2017 and Marchant et al. 2019). However, assuming that the models must have at least one pulse on a time-scale equivalent to the ejection time of the CSM shell we observed, we could set a lower limit on the stellar mass. Thus, in SN 2020xga given that the shell was ejected  $\sim 11$  months before the core collapse, the mass of the progenitor should be  $> 51 M_{\odot}$  for zero metallicity, within this framework. The lower limit corresponds to the case in which the CSM was formed in the first pulses. An upper limit is harder to set because it is closely related to the energetics of the PPI, the number of pulses and the timescales between the pulses; however, if restricted by the PPI regime it must be  $< 62 M_{\odot}$ .

A similar comparison can be done with the H-free low metallicity models developed by Marchant et al. (2019) with the MESA software (Paxton et al. 2011, 2013, 2015, 2018). In this study, the limit goes down to  $47 M_{\odot}$  presumably due to the fact that the models of Marchant et al. (2019) consider mass loss by stellar winds. This value is consistent with the modeling of Renzo

et al. (2020) (see their Table C1), and the shell velocities resulting from their simulations can be similar to the ones found in the spectrum of SN 2020xga.

A comparable analysis for SN 2022xgc indicates that the predicted ejection timeframe of  $\sim 5$  months corresponds to the model with  $> 50 M_{\odot}$  of pure He core (Woosley 2017) for zero metallicity, and  $> 46 M_{\odot}$  when low metallicity is taken into consideration. However, given the variations in the shell velocities in SN 2020xga and SN 2022xgc and therefore in the energetics, the properties of the progenitor stars of SN 2020xga and SN 2022xgc are likely to be different. According to Renzo et al. (2020), even a difference of only  $0.2 M_{\odot}$  across the models may result in distinct PPI characteristics.

As discussed in Leung et al. (2019), there are substantial quantitative differences for the same He core mass between the models of Woosley (2017), Marchant et al. (2019) and by extension Renzo et al. (2020), including ejected masses and time intervals between the pulses which can be traced back to the treatment of shocks and convection. We note that none of the aforementioned models have been constructed to match the observable properties of SN 2020xga and SN 2022xgc and that tuning is required to obtain better estimates for the shell properties; however a qualitative comparison could provide some limits for the mass of the progenitor star which undergoes PPI before the final SN explosion.

The discussion of SN 2018ibb in the context of PPI is challenging as it is considered the best candidate of a PISN (Schulze et al. 2024). PISN can be the end fate for stars with He cores between  $65 - 130 M_{\odot}$  (Heger & Woosley 2002), where the energy produced by the pair creation obliterates the entire star. There are no models of PI SNe which also show eruptions similar to the PPI SNe, although this needs further investigations. However, Schulze et al. (2024) supports the presence of a CSM shell surrounding SN 2018ibb based on the spectroscopic signs of interaction between the ejecta and the shell. The presence of CSM in SN 2018ibb was also supported by our modeling in Sect. 5. The formation of CSM shells has been discussed by Schulze et al. (2024) in the context of an LBV-like eruption analogous to the one in  $\eta$  Carinae.

To strengthen the hypothesis of eruptive mass loss in SN 2020xga and SN 2022xgc, we analyzed the available ATLAS and ZTF forced photometry between 400 days pre-explosion and the time of explosion, paying particular attention to the estimated timeframes of the mass ejections to see if there is any detection. In SN 2022xgc the time of eruption falls into the gap owing to the solar conjunction, therefore we cannot detect any light from the putative blast. In the case of SN 2020xga, we were unable to find any meaningful detection at  $\sim 10$  months before explosion, but merely upper limits, implying that the eruption was probably fainter than the detection limits. Strotjohann et al. (2021) searched systematically for precursor eruptions hundreds of days before the explosion in a sample of SNe at  $z < 0.14$ . Their sample include one SLSN-II with  $z \approx 0.20$  in which a precursor is detected; however, Strotjohann et al. (2021) mentioned that at this progenitor distance the activity is more likely associated with AGN rather than stellar flares. Thus, it is not surprising that we do not detect any activity in the light curve prior to the explosion of SN 2020xga and SN 2022xgc given the distances of these two objects ( $z = 0.4296$  and  $z = 0.3103$ ).

The analysis of the four SLSNe that exhibit the broad Mg II absorption system, revealing the existence of a CSM shell expelled less than a year before the core collapse, has demonstrated that determining the expelling mechanism is challenging because various mechanisms could result in the formation



of CSM at such distances. One possible hint to distinguish the various eruptive mass-loss mechanisms could be to constrain the geometry of the CSM shells. In the future, improved modeling of the very final moments of massive stars will be necessary to comprehend the star's late activity and the mechanisms that lead to the formation of the CSM shells.

### 7.2. When will the ejecta interact with the CSM shell?

As discussed throughout the paper, the second Mg II absorption system in the spectra of SN 2020xga and SN 2022xgc is explained by resonance-line scattering of the SLSN background photospheric emission by a rapidly expanding CSM shell located at a few  $10^{16}$  cm. Thus, it would be interesting to estimate the timescale in which the ejecta will catch up with the fast moving material, which may offer an opportunity to observe the signatures of the CSM interaction.

The way of calculating the time of interaction  $t_{\text{int}}$  is by assuming that the inner radius of the shell is equal to the distance covered by the outer layer of ejecta. This is given by

$$t_{\text{int}} = \frac{V_{\text{in}} t_{\text{erup}}}{V_{\text{ej,max}} - V_{\text{in}}} \quad (9)$$

where  $V_{\text{ej,max}}$  is the velocity of the outer layer of the ejecta,  $t_{\text{erup}}$  is the time of eruption before explosion and  $V_{\text{in}}$  is the minimum velocity of the shell (see definition in Sect. 5). From the spectra of SN 2020xga, we measure a maximum ejecta velocity of  $\sim 13000$  km s $^{-1}$  using the O II lines. Using the predicted value for  $R_{\text{in}}$  in Sect. 5 for the spectra at  $-8.3$  days, we calculated the  $V_{\text{in}} = 3994$  km s $^{-1}$ . Thus, from Eq. 9 we computed that the ejecta will collide with the CSM  $\sim 150$  days after explosion and  $\sim 105$  days after maximum, provided that the rise of the light curve from the first light is 44 days. We do not have any spectroscopic or photometric observation at the time of collision to detect any possible interaction signature in SN 2020xga.

Following the same technique for SN 2022xgc, and measuring a maximum velocity of  $11500$  km s $^{-1}$  from the Fe II triplet and  $V_{\text{in}} = 3955$  km s $^{-1}$ , we estimated a collision time of  $\sim 80$  days after the explosion. Given that the rise from the time of first light is 59 days, the ejecta will interact with the CSM  $\sim 20$  days after maximum. This suggests that when we obtained the X-shooter spectra  $+21.9$  days after peak, the ejecta had more likely already begun interacting with the CSM shell. In addition, in Fig. 4 the blackbody radius of SN 2022xgc at  $+55$  days after peak is  $1 \times 10^{16}$  cm, similar to the the radius of the CSM, strengthening the hypothesis that the ejecta have interacted with the CSM at the time of our observations. We do not see any emerging emission line in the spectra of SN 2022xgc which could have offered information on the CSM interaction; however, this could be due to the fact that the spectral lines are highly sensitive to the density profiles of the ejecta and the CSM (e.g., Fransson 1984; Chevalier & Fransson 2017; Chatzopoulos et al. 2012). Furthermore, the polarimetry of SN 2022xgc does not reveal any evidence of asymmetry that may come from the interaction of the ejecta with the CSM shell, which we anticipate to have happened during the period of time covered by the polarimetry ( $+26.1$  days and  $+60.1$  days after peak). The effect of the CSM interaction might start becoming visible at around 80 post-peak days at which the light curve of SN 2022xgc (see Fig. 2) shows a potential flattening in the *gcr* filters.

Motivated by the above discussion for SN 2020xga and SN 2022xgc, we conducted the same calculations for

SN 2018ibb to check whether our predicted values are consistent with the timescales stated in Schulze et al. (2024). Using the maximum velocity reported in Schulze et al. (2024) of  $12500$  km s $^{-1}$  and the estimated  $R_{\text{in}}$ , we found that the ejecta of SN 2018ibb is predicted to interact with the CSM  $\sim 90$  days after explosion. The rise time of the SN 2018ibb is  $> 93$  days, implying the interaction occurred at sometime during the rise. The light curve of SN 2018ibb shows bumps and undulations in various bands post peak. Furthermore, the [Ca II] emission line, which was already present in the spectrum of SN 2018ibb at  $-1.4$  days, and the [O II] and [O III] emission lines appear approximately  $+30$  days after maximum light, has been associated with the CSM shell. These timescales agree with our predicted interaction time. We should highlight that the computed time of interaction should be taken with caution since it is highly dependent on the (uncertain) maximum velocity and the explosion date.

### 7.3. What is the composition and the mass of the CSM shells?

The determination of the chemical composition of the CSM shells in SN 2020xga and SN 2022xgc is hampered by a lack of observations. In SN 2020xga we do not have observational data at our estimated time of interaction, while for SN 2022xgc even though we found that the ejecta had already started interacting with the CSM shell at the time we obtained the spectra, there are no spectroscopic interaction signatures such as narrow emission lines. This does not necessarily imply that the CSM of SN 2022xgc is H-, He-, and O-free; rather, the evidence of interaction has yet to be revealed.

The Mg II doublet lines that we observed from the CSM are one of the few resonance lines of abundant elements in the observed part of the spectrum along with the Ca II  $\lambda\lambda 3968.5, 4226.7$ , the Na I  $\lambda\lambda 5890.0, 5895.9$  and the K I  $\lambda\lambda 7664.9, 7699.0$  (Morton 2003). Due to the fact that Na I and K I have a low ionization potential, and Ca is less abundant and has a lower ionization potential than Mg, these lines are ionized by the SN continuum. Thus, it is not surprising that we observe only the Mg II doublet from the CSM. The far-UV rest frame below  $\sim 2000$  Å contains a large number of resonance lines, as well as intercombination lines, of abundant ions, like C II-IV, N II-V, O I-IV, which could be used for a more constraining abundance determination. This would, however, require either observations with HST or a SLSN at considerably higher redshift.

Assuming that the CSM shell of SN 2020xga and SN 2022xgc are H-dominated and using the same method as in Lunnan et al. (2018b), we could put an upper limit on the H mass of the shell by utilizing the luminosity of H $\alpha$ . We assumed that the CSM H $\alpha$  peak is blueshifted from the host H $\alpha$  by the velocity of the CSM measured from the Mg II doublet and that the line profile of the CSM H $\alpha$  is similar to the estimated Mg II emission one extended to the maximum velocity of the CSM Mg II absorption. We found that  $L_{\text{H}\alpha} < 1.8 \times 10^{38}$  erg s $^{-1}$  and  $L_{\text{H}\alpha} < 1.2 \times 10^{39}$  erg s $^{-1}$  for SN 2020xga and SN 2022xgc respectively. This yields a limit of  $M_{\text{shell}} < 0.03 f^{0.5} M_{\odot}$  for SN 2020xga and  $M_{\text{shell}} < 0.02 f^{0.5} M_{\odot}$  for SN 2022xgc where  $f$  is the filling factor. These CSM masses are substantially lower than the values for ejected masses expected in Woosley (2017), Marchant et al. (2019), and Renzo et al. (2020), indicating that the shell is most likely not dominated by H and that the H envelope must have been lost before this eruption. This is also evident in SN 2018ibb in which the absence of H and He lines throughout the entire spectral evolution of SN 2018ibb and the existence

of O lines suggests that the CSM shell must be O-dominated and any H and He must reside at much larger radii (Schulze et al. 2024).

#### 7.4. What powers SN 2020xga and SN 2022xgc?

In Sect. 3.4 we modeled the light curves of SN 2020xga and SN 2022xgc with the REDBACK software, assuming they are powered by a magnetar. The modeling resulted in very rapidly-spinning magnetars (1.6 and 0.9 ms, respectively) with ejecta masses of 7 – 9  $M_{\odot}$ , consistent with what is seen in SLSNe-I (Chen et al. 2023b; Gomez et al. 2024). However, the spin period in the case of SN 2020xga and SN 2022xgc approaches the mass-shedding limit (Watts et al. 2016) which suggest that in order to explain the very high luminosities observed in SN 2020xga and SN 2022xgc with the magnetar model, the magnetar must produce energy near to its upper limits without being destabilized.

A remaining question is how a star more massive than  $\sim 50 M_{\odot}$  can explode with  $\sim 9 M_{\odot}$  of ejecta. The stars massive enough to satisfy the PPI conditions form Fe cores, which tend to collapse rather than explode (e.g., Heger & Woosley 2002). However, Woosley et al. (2007) discuss a possibility in which a massive star (with initial mass of  $\sim 95 M_{\odot}$ ) with mild rotation and magnetic torques may have enough angular momentum in its Fe core to form a neutron star with a period of 2 ms. Furthermore, Woosley (2017) investigated the explosions of numerous PPI models, including the model of a  $50 M_{\odot}$  He-core, and discovered that the light curve produced is compatible with observations of some of the brightest SLSNe-I and therefore, in accordance with the observables of SN 2020xga and SN 2022xgc. In the case of the formation of a neutron star, Lunnan et al. (2018b) argue that the magnetic field must be  $> 10^{15}$  G initially to allow the star to explode, but then it must decay to  $< 10^{14}$  G to power the light curve for longer timescales. This scenario would require a high level of fine-tuning in the rotation of the star since it is expected to have a key part in the star’s final death and consequently in the SN explosion.

Alternative scenarios include SN 2020xga and SN 2022xgc being PPISNe or powered by fallback accretion into a black hole. The observed radiated energies of  $> 1.8 \times 10^{51}$  erg and  $> 0.9 \times 10^{51}$  erg for SN 2020xga and SN 2022xgc respectively, cannot be reproduced by the PPISN scenario because the maximum energy of the pure PPISN models is  $\sim 5 \times 10^{50}$  erg unless there is a contribution from a magnetar (Woosley 2017). The latter scenario proposes that the star only partially explodes, resulting in a weak SN explosion and fallback accretion on the equatorial plane (e.g., Dexter & Kasen 2013; Woosley 2017; Moriya et al. 2018). While the fallback material is accreted onto the black hole, the resulting outflows can come in the form of disk winds or jets and they may interact with previously ejected material, causing a significant impact in the SLSN-I light curves. The fallback scenario would lead to high degree of polarization that we do not detect (see Sect 3.5 for SN 2022xgc). However, given the low ejecta mass estimated from the relatively short rise times of the light curves of SN 2020xga and SN 2022xgc, the fallback accretion scenario cannot be disregarded as a plausible powering mechanism.

Determining the powering mechanism of the light curves of SLSNe-I is still an open question and especially in the high mass ranges in which the “explodability” is highly uncertain (e.g., Ertl et al. 2016; Coughlin et al. 2018; see discussion in Renzo et al. 2020). Our observations put limitations on any progenitor model by requiring a significant mass ejections less than a few years before explosion.

## 8. Conclusions

In this work, we provide optical observations of the H-poor SLSNe-I SN 2020xga and SN 2022xgc covering  $-44$  to  $+59$  and  $-59$  to  $+110$  days after maximum light, respectively. Our key findings are as follows:

- SN 2020xga and SN 2022xgc are among the most luminous SLSNe-I with  $M_g = -22.3$  mag and  $M_g = -22.0$  mag, respectively.
- The spectra of SN 2020xga and SN 2022xgc show a second Mg II absorption system coming from CSM surrounding the SNe, but are otherwise similar to the spectra of normal SLSNe-I.
- The modeling of the narrow Mg II resulted in a CSM shell for SN 2020xga located at  $\sim 1.3 \times 10^{16}$  cm and for SN 2022xgc located at  $\sim 0.8 \times 10^{16}$  cm moving at maximum velocity of  $4275 \text{ km s}^{-1}$  and  $4400 \text{ km s}^{-1}$ , respectively.
- The CSM shells of SN 2020xga and SN 2022xgc were expelled less than a year before core-collapse as a result of eruptive-mass loss in the form of LBV-like eruptions or PPI.
- The light curve modeling of SN 2020xga and SN 2022xgc is consistent with magnetar-powered SNe with an ejecta mass of about  $\sim 7 - 9 M_{\odot}$  with magnetars near the mass-shedding limit.
- The PPI scenario suggests He cores  $> 50 M_{\odot}$ , incompatible with the findings of the light curve modeling, hence alternatives such as fallback accretion are discussed.
- The host galaxy properties of SN 2020xga and SN 2022xgc are similar to typical SLSN-I host galaxies and point towards dwarf galaxies.

In this paper we focused on the extensive analysis of the two objects that show the spectroscopic signature of the presence of a CSM shell expelled less than a year before the core collapse. The analysis of the whole X-shooter high-quality spectral sample constraining the fraction of SLSNe that show evidence of eruptive mass loss and establishing observational limitations, will be addressed in a future work. The discovery of these objects can provide an insight into the late stages of stellar evolution as well as a better knowledge of the SLSN-I progenitors.

*Acknowledgements.* Based on observations obtained with the Samuel Oschin Telescope 48-inch and the 60-inch Telescope at the Palomar Observatory as part of the Zwicky Transient Facility project. ZTF is supported by the National Science Foundation under Grants No. AST-1440341 and AST-2034437 and a collaboration including Caltech, IPAC, the Weizmann Institute of Science, the Oskar Klein Center at Stockholm University, the University of Maryland, Deutsches Elektronen-Synchrotron and Humboldt University, the TANGO Consortium of Taiwan, the University of Wisconsin at Milwaukee, Trinity College Dublin, Lawrence Livermore National Laboratories, IN2P3, University of Warwick, Ruhr University Bochum, Northwestern University and former partners the University of Washington, Los Alamos National Laboratories, and Lawrence Berkeley National Laboratories. Operations are conducted by COO, IPAC, and UW. SED Machine is based upon work supported by the National Science Foundation under Grant No. 1106171. The ZTF forced-photometry service was funded under the Heising-Simons Foundation grant #12540303 (PI: Graham). The Gordon and Betty Moore Foundation, through both the Data-Driven Investigator Program and a dedicated grant, provided critical funding for SkyPortal. Based on observations collected at the European Organisation for Astronomical Research in the Southern Hemisphere, Chile, as part of ePESSTO+ (the advanced Public ESO Spectroscopic Survey for Transient Objects Survey). ePESSTO+ observations were obtained under ESO programs ID 106.216C and 108.220C. Some of the observations with the Las Cumbres Observatory data have been obtained via OPTICON proposals and as part of the Global Supernova Project. The OPTICON project has received funding from the European Union’s Horizon 2020 research and innovation programme under grant agreement No 730890. This work has made use of data from the Asteroid Terrestrial-impact Last Alert System (ATLAS) project. ATLAS is primarily funded to search for near earth asteroids through NASA grants NN12AR55G, 80NSSC18K0284, and 80NSSC18K1575; byproducts of the NEO search include images and catalogs

from the survey area. The ATLAS science products have been made possible through the contributions of the University of Hawaii Institute for Astronomy, the Queen's University Belfast, the Space Telescope Science Institute, and the South African Astronomical Observatory. Partially based on observations made with the Nordic Optical Telescope, owned in collaboration by the University of Turku and Aarhus University, and operated jointly by Aarhus University, the University of Turku and the University of Oslo, representing Denmark, Finland and Norway, the University of Iceland and Stockholm University at the Observatorio del Roque de los Muchachos, La Palma, Spain, of the Instituto de Astrofísica de Canarias. The Liverpool Telescope is operated on the island of La Palma by Liverpool John Moores University in the Spanish Observatorio del Roque de los Muchachos of the Instituto de Astrofísica de Canarias with financial support from the UK Science and Technology Facilities Council. Based on observations made with the Italian Telescopio Nazionale Galileo (TNG) operated on the island of La Palma by the Fundación Galileo Galilei of the INAF (Istituto Nazionale di Astrofisica) at the Spanish Observatorio del Roque de los Muchachos of the Instituto de Astrofísica de Canarias. RL is supported by the European Research Council (ERC) under the European Union's Horizon Europe research and innovation programme (grant agreement No. 10104229 - TransPIre). FP acknowledges support from the Spanish Ministerio de Ciencia, Innovación y Universidades (MICINN) under grant numbers PID2022-141915NB-C21. SS is partially supported by LBNL Subcontract 7707915. NS is supported by the Knut and Alice Wallenberg foundation through the "Gravity Meets Light" project. RKT is supported by the NKFIH/OTKA FK-134432 and the NKFIH/OTKA K-142534 grant of the National Research, Development and Innovation (NRDI) Office of Hungary. MN is supported by the European Research Council (ERC) under the European Union's Horizon 2020 research and innovation programme (grant agreement No. 948381) and by UK Space Agency Grant No. ST/Y000692/1. JPA is supported by ANID, Millennium Science Initiative, ICN12\_009. T.E.M.B. acknowledges financial support from the Spanish Ministerio de Ciencia e Innovación (MCIN), the Agencia Estatal de Investigación (AEI) 10.13039/501100011033, and the European Union Next Generation EU/PRTR funds under the 2021 Juan de la Cierva program FJC2021-047124-I and the PID2020-115253GA-I00 HOSTFLOWS project, from Centro Superior de Investigaciones Científicas (CSIC) under the PIE project 20215AT016, and the program Unidad de Excelencia María de Maeztu CEX2020-001058-M. MB and TP acknowledge the financial support from the Slovenian Research Agency (grants I0-0033, P1-0031, J1-8136, J1-2460 and Z1-1853) and the Young Researchers program. MK acknowledges financial support from MICINN (Spain) through the programme Juan de la Cierva-Incorporación [JC2022-049447-I] and from AGAUR, CSIC, MCIN and AEI 10.13039/501100011033 under projects PID2023-151307NB-I00, PIE 20215AT016, CEX2020-001058-M, and 2021-SGR-01270. CPG acknowledges financial support from the Secretary of Universities and Research (Government of Catalonia) and by the Horizon 2020 Research and Innovation Programme of the European Union under the Marie Skłodowska-Curie and the Beatriu de Pinós 2021 BP 00168 programme, from the Spanish Ministerio de Ciencia e Innovación (MCIN) and the Agencia Estatal de Investigación (AEI) 10.13039/501100011033 under the PID2020-115253GA-I00 HOSTFLOWS project, and the program Unidad de Excelencia María de Maeztu CEX2020-001058-M. L.G. acknowledges financial support from AGAUR, CSIC, MCIN and AEI 10.13039/501100011033 under projects PID2023-151307NB-I00, PIE 20215AT016, CEX2020-001058-M, and 2021-SGR-01270. T.-W.C. acknowledges the Yushan Fellow Program by the Ministry of Education, Taiwan for the financial support (MOE-111-YSFMS-0008-001-P1). MF is supported by a Royal Society - Science Foundation Ireland University Research Fellowship. This work makes use of data from the Las Cumbres Observatory global network of telescopes. The LCO group is supported by NSF grants AST-1911151 and AST-1911225. IPF acknowledges financial support from the Spanish Agencia Estatal de Investigación del Ministerio de Ciencia e Innovación (AEI-MCINN) under grant PID2022-137779OB-C44. AS acknowledges the Warwick Astrophysics PhD prize scholarship made possible thanks to a generous philanthropic donation.

## References

Aamer, A., Nicholl, M., Jerkstrand, A., et al. 2024, *MNRAS*, 527, 11970  
 Ahn, C. P., Alexandroff, R., Allende Prieto, C., et al. 2012, *ApJS*, 203, 21  
 Akashi, M. & Kashi, A. 2020, *MNRAS*, 494, 3186  
 Ambikasaran, S., Foreman-Mackey, D., Greengard, L., Hogg, D. W., & O'Neil, M. 2015, *IEEE Transactions on Pattern Analysis and Machine Intelligence*, 38, 252  
 Angus, C. R., Levan, A. J., Perley, D. A., et al. 2016, *MNRAS*, 458, 84  
 Angus, C. R., Smith, M., Sullivan, M., et al. 2019, *MNRAS*, 487, 2215  
 Arabsalmani, M., Möller, P., Perley, D. A., et al. 2018, *MNRAS*, 473, 3312  
 Arnett, W. D. & Fu, A. 1989, *ApJ*, 340, 396  
 Ashton, G., Hübner, M., Lasky, P. D., et al. 2019, *ApJS*, 241, 27  
 Asplund, M., Amarsi, A. M., & Grevesse, N. 2021, *A&A*, 653, A141

Barkat, Z., Rakavy, G., & Sack, N. 1967, *Phys. Rev. Lett.*, 18, 379  
 Bellm, E. C., Kulkarni, S. R., Graham, M. J., et al. 2019, *PASP*, 131, 018002  
 Blagorodnova, N., Neill, J. D., Walters, R., et al. 2018, *PASP*, 130, 035003  
 Blanchard, P. K., Berger, E., Nicholl, M., & Villar, V. A. 2020, *ApJ*, 897, 114  
 Branch, D., Benetti, S., Kasen, D., et al. 2002, *ApJ*, 566, 1005  
 Brennan, S. J. & Fraser, M. 2022, *A&A*, 667, A62  
 Buzzoni, B., Delabre, B., Dekker, H., et al. 1984, *The Messenger*, 38, 9  
 Byler, N., Dalcanton, J. J., Conroy, C., & Johnson, B. D. 2017, *ApJ*, 840, 44  
 Calzetti, D., Armus, L., Bohlin, R. C., et al. 2000, *ApJ*, 533, 682  
 Chabrier, G. 2003, *PASP*, 115, 763  
 Chambers, K. C., Boer, T. D., Bulger, J., et al. 2020, *Transient Name Server Discovery Report*, 2020-3164, 1  
 Chambers, K. C., Magnier, E. A., Metcalfe, N., et al. 2016, *arXiv e-prints*, arXiv:1612.05560  
 Chatzopoulos, E., Wheeler, J. C., & Vinko, J. 2012, *ApJ*, 746, 121  
 Chen, H.-W. 2012, *MNRAS*, 419, 3039  
 Chen, T.-W., Smartt, S. J., Bresolin, F., et al. 2013, *ApJ*, 763, L28  
 Chen, T.-W., Smartt, S. J., Yates, R. M., et al. 2017, *MNRAS*, 470, 3566  
 Chen, Z. H., Yan, L., Kangas, T., et al. 2023a, *ApJ*, 943, 41  
 Chen, Z. H., Yan, L., Kangas, T., et al. 2023b, *ApJ*, 943, 42  
 Cheng, S. J., Goldberg, J. A., Cantiello, M., et al. 2024, *arXiv e-prints*, arXiv:2405.12274  
 Chevalier, R. A. & Fransson, C. 2017, in *Handbook of Supernovae*, ed. A. W. Alsabti & P. Murdin, 875  
 Chomiuk, L., Chornock, R., Soderberg, A. M., et al. 2011, *ApJ*, 743, 114  
 Conroy, C., Gunn, J. E., & White, M. 2009, *ApJ*, 699, 486  
 Coughlin, E. R., Quataert, E., Fernández, R., & Kasen, D. 2018, *MNRAS*, 477, 1225  
 Coughlin, M. W., Bloom, J. S., Nir, G., et al. 2023, *ApJS*, 267, 31  
 Currie, D. G., Dorland, B. N., & Kaufer, A. 2002, *A&A*, 389, L65  
 Davidson, K. 1987, *ApJ*, 317, 760  
 Davidson, K., Smith, N., Gull, T. R., Ishibashi, K., & Hillier, D. J. 2001, *AJ*, 121, 1569  
 De Cia, A., Gal-Yam, A., Rubin, A., et al. 2018, *ApJ*, 860, 100  
 Dekany, R., Smith, R. M., Riddle, R., et al. 2020, *PASP*, 132, 038001  
 Dessart, L. 2019, *A&A*, 621, A141  
 Dessart, L., Hillier, D. J., Waldman, R., Livne, E., & Blondin, S. 2012, *MNRAS*, 426, L76  
 Dexter, J. & Kasen, D. 2013, *ApJ*, 772, 30  
 Dey, A., Schlegel, D. J., Lang, D., et al. 2019, *AJ*, 157, 168  
 Ergon, M., Sollerman, J., Pursimo, T., et al. 2013, *The Astronomer's Telegram*, 4912, 1  
 Ertl, T., Janka, H. T., Woosley, S. E., Sukhbold, T., & Ugliano, M. 2016, *ApJ*, 818, 124  
 Fernández, V., Amorín, R., Firpo, V., & Morisset, C. 2024, *arXiv e-prints*, arXiv:2405.15072  
 Fiore, A., Chen, T. W., Jerkstrand, A., et al. 2021, *MNRAS*, 502, 2120  
 Fitzpatrick, E. L. 1999, *PASP*, 111, 63  
 Flewelling, H. A., Magnier, E. A., Chambers, K. C., et al. 2020, *ApJS*, 251, 7  
 Foreman-Mackey, D., Sick, J., & Johnson, B. 2014, *Python-Fsps: Python Bindings To Fsps (V0.1.1)*  
 Fransson, C. 1984, *A&A*, 132, 115  
 Fremling, C. 2022, *Transient Name Server Discovery Report*, 2022-2935, 1  
 Fremling, C., Sollerman, J., Taddia, F., et al. 2016, *A&A*, 593, A68  
 Friis, M., De Cia, A., Krühler, T., et al. 2015, *MNRAS*, 451, 167  
 Fuller, J. & Ro, S. 2018, *MNRAS*, 476, 1853  
 Gal-Yam, A. 2012, *Science*, 337, 927  
 Gal-Yam, A. 2019a, *ApJ*, 882, 102  
 Gal-Yam, A. 2019b, *ARA&A*, 57, 305  
 Galbany, L., Anderson, J. P., Rosales-Ortega, F. F., et al. 2016, *MNRAS*, 455, 4087  
 Gkini, A., Lunnan, R., Schulze, S., et al. 2024, *A&A*, 685, A20  
 Goldoni, P., Royer, F., François, P., et al. 2006, in *Society of Photo-Optical Instrumentation Engineers (SPIE) Conference Series*, Vol. 6269, *Society of Photo-Optical Instrumentation Engineers (SPIE) Conference Series*, ed. I. S. McLean & M. Iye, 62692K  
 Gomez, S., Nicholl, M., Berger, E., et al. 2024, *The Type I Superluminous Supernova Catalog I: Light Curve Properties, Models, and Catalog Description*  
 Göteborg, Y., de Mink, S. E., & Groh, J. H. 2017, *A&A*, 608, A11  
 Graham, M. J., Kulkarni, S. R., Bellm, E. C., et al. 2019, *PASP*, 131, 078001  
 Gromadzki, M., Grzesiak, K., Kravtsov, T., et al. 2022, *Transient Name Server AstroNote*, 253, 1  
 Gromadzki, M., Ihanec, N., Moran, S., & Yaron, O. 2020, *Transient Name Server Classification Report*, 2020-3372, 1  
 Grzesiak, K., Gromadzki, M., Kravtsov, T., et al. 2022, *Transient Name Server AstroNote*, 255, 1  
 Gutiérrez, C. P., Pastorello, A., Bersten, M., et al. 2022, *MNRAS*, 517, 2056  
 Heger, A. & Woosley, S. E. 2002, *ApJ*, 567, 532  
 Heiles, C. 2000, *AJ*, 119, 923  
 Hsu, B., Hosseinzadeh, G., & Berger, E. 2021, *ApJ*, 921, 180



- Humphreys, R. M. 1999, in *IAU Colloq. 169: Variable and Non-spherical Stellar Winds in Luminous Hot Stars*, ed. B. Wolf, O. Stahl, & A. W. Fullerton, Vol. 523, 243
- Ihanec, N., Gromadzki, M., Moran, S., et al. 2020, *Transient Name Server AstroNote*, 220, 1
- Insera, C., Nicholl, M., Chen, T. W., et al. 2017, *MNRAS*, 468, 4642
- Insera, C., Smartt, S. J., Jerkstrand, A., et al. 2013, *ApJ*, 770, 128
- Jiang, T., Malhotra, S., Rhoads, J. E., & Yang, H. 2019, *ApJ*, 872, 145
- Johnson, B. D., Leja, J., Conroy, C., & Speagle, J. S. 2021, *ApJS*, 254, 22
- Kaiser, N., Burgett, W., Chambers, K., et al. 2010, in *Society of Photo-Optical Instrumentation Engineers (SPIE) Conference Series*, Vol. 7733, *Ground-based and Airborne Telescopes III*, ed. L. M. Stepp, R. Gilmozzi, & H. J. Hall, 77330E
- Kasen, D. 2017, in *Handbook of Supernovae*, ed. A. W. Alsabti & P. Murdin, 939
- Kasen, D. & Bildsten, L. 2010, *ApJ*, 717, 245
- Kennicutt, Robert C., J. 1998, *ApJ*, 498, 541
- Kewley, L. J. & Ellison, S. L. 2008, *ApJ*, 681, 1183
- Kim, Y. L., Rigault, M., Neill, J. D., et al. 2022, *PASP*, 134, 024505
- Kleiser, I. K. W. & Kasen, D. 2014, *MNRAS*, 438, 318
- Könyves-Tóth, R. 2022, *ApJ*, 940, 69
- Kramida, A., Yu. Ralchenko, Reader, J., & and NIST ASD Team. 2022, *NIST Atomic Spectra Database (ver. 5.10)*, [Online]. Available: <https://physics.nist.gov/asd> [2023, March 29]. National Institute of Standards and Technology, Gaithersburg, MD.
- Krühler, T., Malesani, D., Fynbo, J. P. U., et al. 2015, *A&A*, 581, A125
- Lamers, H. J. G. L. M., Haser, S., de Koter, A., & Leitherer, C. 1999, *ApJ*, 516, 872
- Laplace, E., Göteborg, Y., de Mink, S. E., Justham, S., & Farmer, R. 2020, *A&A*, 637, A6
- Ledoux, C., Petitjean, P., Fynbo, J. P. U., Møller, P., & Srianand, R. 2006, *A&A*, 457, 71
- Leloudas, G., Chatzopoulos, E., Dilday, B., et al. 2012, *A&A*, 541, A129
- Leloudas, G., Schulze, S., Krühler, T., et al. 2015, *MNRAS*, 449, 917
- Leung, S.-C., Nomoto, K., & Blinnikov, S. 2019, *ApJ*, 887, 72
- Leung, S.-C., Wu, S., & Fuller, J. 2021, *ApJ*, 923, 41
- Liu, Y.-Q., Modjaz, M., & Bianco, F. B. 2017, *ApJ*, 845, 85
- Lucy, L. B. & Solomon, P. M. 1970, *ApJ*, 159, 879
- Lunnan, R., Chornock, R., Berger, E., et al. 2018a, *ApJ*, 852, 81
- Lunnan, R., Chornock, R., Berger, E., et al. 2014, *ApJ*, 787, 138
- Lunnan, R., Chornock, R., Berger, E., et al. 2016, *ApJ*, 831, 144
- Lunnan, R., Fransson, C., Vreeswijk, P. M., et al. 2018b, *Nature Astronomy*, 2, 887
- Lupton, R., Blanton, M. R., Fekete, G., et al. 2004, *PASP*, 116, 133
- Lyman, J. D., Bersier, D., & James, P. A. 2014, *MNRAS*, 437, 3848
- Madau, P. & Dickinson, M. 2014, *ARA&A*, 52, 415
- Marchant, P., Renzo, M., Farmer, R., et al. 2019, *ApJ*, 882, 36
- Masci, F. J., Laher, R. R., Rusholme, B., et al. 2019, *PASP*, 131, 018003
- Mazzali, P. A., Sullivan, M., Pian, E., Greiner, J., & Kann, D. A. 2016, *MNRAS*, 458, 3455
- Metzger, B. D., Margalit, B., Kasen, D., & Quataert, E. 2015, *MNRAS*, 454, 3311
- Modigliani, A., Goldoni, P., Royer, F., et al. 2010, in *Society of Photo-Optical Instrumentation Engineers (SPIE) Conference Series*, Vol. 7737, *Observatory Operations: Strategies, Processes, and Systems III*, ed. D. R. Silva, A. B. Peck, & B. T. Soifer, 773728
- Modjaz, M., Liu, Y. Q., Bianco, F. B., & Graur, O. 2016, *ApJ*, 832, 108
- Møller, P., Fynbo, J. P. U., Ledoux, C., & Nilsson, K. K. 2013, *MNRAS*, 430, 2680
- Moriya, T. J., Nicholl, M., & Guillochon, J. 2018, *ApJ*, 867, 113
- Morton, D. C. 2003, *ApJS*, 149, 205
- Neill, J. D., Sullivan, M., Gal-Yam, A., et al. 2011, *ApJ*, 727, 15
- Nicholl, M., Berger, E., Smartt, S. J., et al. 2016, *ApJ*, 826, 39
- Nicholl, M., Guillochon, J., & Berger, E. 2017, *ApJ*, 850, 55
- Nicholl, M., Smartt, S. J., Jerkstrand, A., et al. 2014, *MNRAS*, 444, 2096
- Nicholl, M., Smartt, S. J., Jerkstrand, A., et al. 2013, *Nature*, 502, 346
- Nicholl, M., Smartt, S. J., Jerkstrand, A., et al. 2015a, *MNRAS*, 452, 3869
- Nicholl, M., Smartt, S. J., Jerkstrand, A., et al. 2015b, *ApJ*, 807, L18
- Oke, J. B. & Gunn, J. E. 1982, *PASP*, 94, 586
- Omand, C. M. B. & Sarin, N. 2024, *MNRAS*, 527, 6455
- Ørum, S. V., Ivens, D. L., Strandberg, P., et al. 2020, *A&A*, 643, A47
- Osterbrock, D. E. & Ferland, G. J. 2006, *Astrophysics of gaseous nebulae and active galactic nuclei*
- Ostriker, J. P. & Gunn, J. E. 1971, *ApJ*, 164, L95
- Owoccki, S. P., Gayley, K. G., & Shaviv, N. J. 2004, *ApJ*, 616, 525
- Pagel, B. E. J., Edmunds, M. G., Blackwell, D. E., Chun, M. S., & Smith, G. 1979, *MNRAS*, 189, 95
- Pastorello, A., Smartt, S. J., Botticella, M. T., et al. 2010, *ApJ*, 724, L16
- Paxton, B., Bildsten, L., Dotter, A., et al. 2011, *ApJS*, 192, 3
- Paxton, B., Cantiello, M., Arras, P., et al. 2013, *ApJS*, 208, 4
- Paxton, B., Marchant, P., Schwab, J., et al. 2015, *ApJS*, 220, 15
- Paxton, B., Schwab, J., Bauer, E. B., et al. 2018, *ApJS*, 234, 34
- Perley, D. A., Fremling, C., Sollerman, J., et al. 2020, *ApJ*, 904, 35
- Perley, D. A., Quimby, R. M., Yan, L., et al. 2016, *ApJ*, 830, 13
- Petrović, J. 2020, *Serbian Astronomical Journal*, 201, 1
- Petrović, J., Langer, N., & van der Hucht, K. A. 2005, *A&A*, 435, 1013
- Pettini, M. & Pagel, B. E. J. 2004, *MNRAS*, 348, L59
- Piro, A. L. 2015, *ApJ*, 808, L51
- Planck Collaboration, Aghanim, N., Akrami, Y., et al. 2020, *A&A*, 641, A6
- Poidevin, F., Pérez-Fournon, I., Delgado-González, Z., et al. 2022, *Transient Name Server Classification Report*, 2022-3523, 1
- Prochaska, J., Hennawi, J., Westfall, K., et al. 2020a, *The Journal of Open Source Software*, 5, 2308
- Prochaska, J. X., Hennawi, J., Cooke, R., et al. 2020b, *pypeit/PypeIt: Release 1.0.0*
- Puls, J., Vink, J. S., & Najarro, F. 2008, *A&A Rev.*, 16, 209
- Pursiainen, M., Leloudas, G., Cikota, A., et al. 2023, *A&A*, 674, A81
- Pursiainen, M., Leloudas, G., Paraskeva, E., et al. 2022, *A&A*, 666, A30
- Quimby, R. M., De Cia, A., Gal-Yam, A., et al. 2018, *ApJ*, 855, 2
- Quimby, R. M., Kulkarni, S. R., Kasliwal, M. M., et al. 2011, *Nature*, 474, 487
- Rakavy, G. & Shaviv, G. 1967, *ApJ*, 148, 803
- Renzo, M., Farmer, R., Justham, S., et al. 2020, *A&A*, 640, A56
- Rigault, M., Neill, J. D., Blagorodnova, N., et al. 2019, *A&A*, 627, A115
- Saito, S., Tanaka, M., Mazzali, P. A., Hachinger, S., & Hotokezaka, K. 2024, *ApJ*, 967, 13
- Sarin, N., Hübner, M., Omand, C. M. B., et al. 2024, *MNRAS*, 531, 1203
- Sarin, N., Omand, C. M. B., Margalit, B., & Jones, D. I. 2022, *MNRAS*, 516, 4949
- Schlaflly, E. F. & Finkbeiner, D. P. 2011, *ApJ*, 737, 103
- Schulze, S., Fransson, C., Kozyreva, A., et al. 2024, *A&A*, 683, A223
- Schulze, S., Krühler, T., Leloudas, G., et al. 2018, *MNRAS*, 473, 1258
- Schulze, S., Yaron, O., Sollerman, J., et al. 2021, *ApJS*, 255, 29
- Selsing, J., Malesani, D., Goldoni, P., et al. 2019, *A&A*, 623, A92
- Serkowski, K., Mathewson, D. S., & Ford, V. L. 1975, *ApJ*, 196, 261
- Shingles, L., Smith, K. W., Young, D. R., et al. 2021, *Transient Name Server AstroNote*, 7, 1
- Silverman, J. M., Foley, R. J., Filippenko, A. V., et al. 2012, *MNRAS*, 425, 1789
- Smartt, S. J., Valenti, S., Fraser, M., et al. 2015, *A&A*, 579, A40
- Smith, K. W., Smartt, S. J., Young, D. R., et al. 2020, *PASP*, 132, 085002
- Smith, M., Sullivan, M., D'Andrea, C. B., et al. 2016, *ApJ*, 818, L8
- Smith, N. 2002, *MNRAS*, 337, 1252
- Smith, N. 2006, *ApJ*, 644, 1151
- Smith, N. 2008, *Nature*, 455, 201
- Smith, N. & Arnett, W. D. 2014, *ApJ*, 785, 82
- Smith, N., Gehrz, R. D., Hinz, P. M., et al. 2003, *AJ*, 125, 1458
- Smith, N. & Morse, J. A. 2004, *ApJ*, 605, 854
- Sobolev, V. V. 1957, *Soviet Ast.*, 1, 678
- Sorokina, E., Blinnikov, S., Nomoto, K., Quimby, R., & Tolstov, A. 2016, *ApJ*, 829, 17
- Speagle, J. S. 2020a, *MNRAS*, 493, 3132
- Speagle, J. S. 2020b, *MNRAS*, 493, 3132
- Steele, I. A., Smith, R. J., Rees, P. C., et al. 2004, in *Society of Photo-Optical Instrumentation Engineers (SPIE) Conference Series*, Vol. 5489, *Ground-based Telescopes*, ed. J. Oschmann, Jacobus M., 679-692
- Strotjohann, N. L., Ofek, E. O., Gal-Yam, A., et al. 2021, *ApJ*, 907, 99
- Suzuki, A. & Maeda, K. 2021, *ApJ*, 908, 217
- Taggart, K. & Perley, D. A. 2021, *MNRAS*, 503, 3931
- Thomas, R. C., Nugent, P. E., & Meza, J. C. 2011, *PASP*, 123, 237
- Tonry, J., Denneau, L., Heinze, A., et al. 2020, *Transient Name Server Discovery Report*, 2020-3392, 1
- Tonry, J. L., Denneau, L., Heinze, A. N., et al. 2018, *Publications of the Astronomical Society of the Pacific*, 130, 064505
- van der Walt, S., Crellin-Quick, A., & Bloom, J. 2019, *The Journal of Open Source Software*, 4, 1247
- van Dokkum, P. G. 2001, *PASP*, 113, 1420
- Vernet, J., Dekker, H., D'Odorico, S., et al. 2011, *A&A*, 536, A105
- Vreeswijk, P. M., Leloudas, G., Gal-Yam, A., et al. 2017, *ApJ*, 835, 58
- Vreeswijk, P. M., Savaglio, S., Gal-Yam, A., et al. 2014, *ApJ*, 797, 24
- Vurm, I. & Metzger, B. D. 2021, *ApJ*, 917, 77
- Wang, L., Wheeler, J. C., & Höflich, P. 1997, *ApJ*, 476, L27
- Watts, A. L., Andersson, N., Chakrabarty, D., et al. 2016, *Reviews of Modern Physics*, 88, 021001
- Weaver, T. A. & Woosley, S. E. 1993, *Phys. Rep.*, 227, 65
- Weaver, T. A., Zimmerman, G. B., & Woosley, S. E. 1978, *ApJ*, 225, 1021
- Westphal, J. A. & Neugebauer, G. 1969, *ApJ*, 156, L45
- Wheeler, J. C., Chatzopoulos, E., Vinkó, J., & Tuminello, R. 2017, *ApJ*, 851, L14
- Woosley, S. E. 2010, *ApJ*, 719, L204
- Woosley, S. E. 2017, *ApJ*, 836, 244
- Woosley, S. E., Blinnikov, S., & Heger, A. 2007, *Nature*, 450, 390

- Woosley, S. E., Heger, A., & Weaver, T. A. 2002, *Reviews of Modern Physics*, 74, 1015
- Yan, L., Lunnan, R., Perley, D. A., et al. 2017a, *ApJ*, 848, 6
- Yan, L., Quimby, R., Gal-Yam, A., et al. 2017b, *ApJ*, 840, 57
- Yan, L., Quimby, R., Ofek, E., et al. 2015, *ApJ*, 814, 108
- Yaron, O. & Gal-Yam, A. 2012, *PASP*, 124, 668
- Yoon, S.-C., Dessart, L., & Clocchiatti, A. 2017, *ApJ*, 840, 10
- Young, D. R. 2020, *plot\_atlas\_fp.py*
- 
- <sup>1</sup> The Oskar Klein Centre, Department of Astronomy, Stockholm University, Albanova University Center, 106 91 Stockholm, Sweden
- <sup>2</sup> Center for Interdisciplinary Exploration and Research in Astrophysics (CIERA), Northwestern University, 1800 Sherman Ave, Evanston, IL 60201, USA
- <sup>3</sup> Instituto de Astrofísica de Canarias, Vía Láctea, 38205 La Laguna, Tenerife, Spain
- <sup>4</sup> Universidad de La Laguna, Departamento de Astrofísica, 38206 La Laguna, Tenerife, Spain
- <sup>5</sup> The Oskar Klein Centre, Department of Physics, Stockholm University, Albanova University Center, SE-106 91 Stockholm, Sweden
- <sup>6</sup> Nordita, Stockholm University and KTH Royal Institute of Technology, Hannes Alfvéns väg 12, 106 91, Stockholm, Sweden
- <sup>7</sup> Konkoly Observatory, Research Center for Astronomy and Earth Sciences, H-1121 Budapest Konkoly Th. M. út 15-17., Hungary; MTA Centre of Excellence
- <sup>8</sup> Department of Experimental Physics, Institute of Physics, University of Szeged, Dóm tér 9, Szeged, 6720 Hungary
- <sup>9</sup> Astrophysics Research Institute, Liverpool John Moores University, Liverpool Science Park, 146 Brownlow Hill, Liverpool L3 5RF, UK
- <sup>10</sup> European Southern Observatory, Alonso de Córdova 3107, Casilla 19, Santiago, Chile
- <sup>11</sup> Millennium Institute of Astrophysics MAS, Nuncio Monsenor Sotero Sanz 100, Off.104, Providencia, Santiago, Chile
- <sup>12</sup> Center for Astrophysics and Cosmology, University of Nova Gorica, Vipavska 11c, 5270 Ajdovščina, Slovenia
- <sup>13</sup> Graduate Institute of Astronomy, National Central University, 300 Jhongda Road, 32001 Jhongli, Taiwan
- <sup>14</sup> Caltech Optical Observatories, California Institute of Technology, Pasadena, CA 91125, USA
- <sup>15</sup> School of Physics, University College Dublin, LMI Main Building, Beech Hill Road, Dublin 4, D04 P7W1
- <sup>16</sup> Division of Physics, Mathematics and Astronomy, California Institute of Technology, Pasadena, CA 91125, USA
- <sup>17</sup> Institute of Space Sciences (ICE, CSIC), Campus UAB, Carrer de Can Magrans, s/n, E-08193 Barcelona, Spain
- <sup>18</sup> Institut d'Estudis Espacials de Catalunya (IEEC), 08860 Castelldefels (Barcelona), Spain
- <sup>19</sup> Department of Particle Physics and Astrophysics, Weizmann Institute of Science, 234 Herzl St, 76100 Rehovot, Israel
- <sup>20</sup> GRANTECAN, Cuesta de San José s/n, 38712 Breña Baja, La Palma, Spain
- <sup>21</sup> Las Cumbres Observatory, 6740 Cortona Dr. Suite 102, Goleta, CA, 93117, USA
- <sup>22</sup> Department of Physics, University of California, Santa Barbara, CA 93106-9530, USA
- <sup>23</sup> Astronomical Observatory, University of Warsaw, Al. Ujazdowskie 4, 00-478 Warszawa, Poland
- <sup>24</sup> IPAC, California Institute of Technology, 1200 E. California Blvd, Pasadena, CA 91125, USA
- <sup>25</sup> Center for Astrophysics, Harvard & Smithsonian, 60 Garden Street, Cambridge, MA 02138-1516, USA
- <sup>26</sup> The NSF AI Institute for Artificial Intelligence and Fundamental Interactions, USA
- <sup>27</sup> Cardiff Hub for Astrophysics Research and Technology, School of Physics & Astronomy, Cardiff University, Queens Buildings, The Parade, Cardiff, CF24 3AA, UK
- <sup>28</sup> LPNHE, CNRS/IN2P3, Sorbonne Université, Université Paris-Cité, Laboratoire de Physique Nucléaire et de Hautes Énergies, 75005 Paris, France
- <sup>29</sup> Department of Physics and Astronomy, University of Turku, 20014 Turku, Finland
- <sup>30</sup> Astrophysics Research Centre, School of Mathematics and Physics, Queens University Belfast, Belfast BT7 1NN, UK
- <sup>31</sup> Instituto de Alta Investigación, Universidad de Tarapacá, Casilla 7D, Arica, Chile
- <sup>32</sup> Dipartimento di Fisica “Ettore Pancini”, Università di Napoli Federico II, Via Cinthia 9, 80126 Naples, Italy
- <sup>33</sup> INAF - Osservatorio Astronomico di Capodimonte, Via Moiariello 16, I-80131 Naples, Italy
- <sup>34</sup> Department of Physics, University of Warwick, Gibbet Hill Road, Coventry CV4 7AL, UK
- <sup>35</sup> Astrophysics sub-Department, Department of Physics, University of Oxford, Keble Road, Oxford, OX1 3RH, UK

## Appendix A: Photometric data

Table A.1: continued.

Table A.1: Photometric data of SN 2020xga.

MJD	Phase <sup>d</sup> (days)	Filter	Magnitude (mag)	Instrument	MJD	Phase <sup>d</sup> (days)	Filter	Magnitude (mag)	Instrument
59110.5	-43.4	<i>c</i>	21.12 ± 0.34	ATLAS	59168.8	-2.6	<i>g</i>	19.18 ± 0.05	ZTF
59116.9	-38.9	<i>r</i>	21.00 ± 0.23	ZTF	59168.8	-2.6	<i>r</i>	19.30 ± 0.08	ZTF
59117.6	-38.4	<i>c</i>	20.94 ± 0.34	ATLAS	59169.8	-1.9	<i>r</i>	19.30 ± 0.05	ZTF
59119.5	-37.1	<i>o</i>	20.50 ± 0.31	ATLAS	59169.8	-1.9	<i>g</i>	19.32 ± 0.05	ZTF
59120.0	-36.7	<i>g</i>	20.93 ± 0.16	ZTF	59170.5	-1.4	<i>c</i>	19.33 ± 0.07	ATLAS
59122.9	-34.7	<i>g</i>	20.00 ± 0.27	ZTF	59170.5	-1.4	<i>g</i>	19.30 ± 0.03	LT
59123.9	-34.0	<i>r</i>	19.80 ± 0.25	ZTF	59170.5	-1.4	<i>r</i>	19.32 ± 0.02	LT
59128.6	-30.7	<i>o</i>	20.06 ± 0.29	ATLAS	59170.5	-1.4	<i>i</i>	19.42 ± 0.03	LT
59130.0	-29.8	<i>r</i>	20.20 ± 0.17	ZTF	59171.0	-1.1	<i>z</i>	19.46 ± 0.08	LT
59130.5	-29.4	<i>o</i>	20.02 ± 0.20	ATLAS	59171.8	-0.5	<i>r</i>	19.28 ± 0.04	ZTF
59131.9	-28.4	<i>g</i>	19.93 ± 0.20	ZTF	59171.8	-0.5	<i>g</i>	19.27 ± 0.04	ZTF
59134.9	-26.3	<i>g</i>	20.28 ± 0.16	ZTF	59172.4	-0.0	<i>i</i>	19.41 ± 0.15	LCO
59134.9	-26.3	<i>r</i>	19.96 ± 0.13	ZTF	59174.0	1.1	<i>g</i>	19.32 ± 0.03	LT
59136.9	-24.9	<i>g</i>	19.89 ± 0.08	ZTF	59174.0	1.1	<i>r</i>	19.32 ± 0.03	LT
59138.8	-23.5	<i>r</i>	19.91 ± 0.11	ZTF	59174.0	1.1	<i>i</i>	19.47 ± 0.03	LT
59140.5	-22.4	<i>o</i>	19.97 ± 0.15	ATLAS	59174.0	1.1	<i>z</i>	19.59 ± 0.08	LT
59140.9	-22.1	<i>g</i>	19.81 ± 0.08	ZTF	59174.8	1.6	<i>g</i>	19.38 ± 0.14	ZTF
59142.5	-21.0	<i>c</i>	19.71 ± 0.12	ATLAS	59176.8	3.0	<i>r</i>	19.29 ± 0.08	ZTF
59142.9	-20.7	<i>r</i>	19.63 ± 0.07	ZTF	59176.9	3.1	<i>g</i>	19.42 ± 0.06	ZTF
59142.9	-20.7	<i>g</i>	19.66 ± 0.06	ZTF	59178.5	4.2	<i>o</i>	19.27 ± 0.13	ATLAS
59143.9	-20.0	<i>g</i>	19.84 ± 0.07	ZTF	59178.8	4.4	<i>r</i>	19.26 ± 0.08	ZTF
59144.4	-19.6	<i>o</i>	19.83 ± 0.14	ATLAS	59180.3	5.5	<i>o</i>	19.33 ± 0.18	ATLAS
59144.9	-19.3	<i>g</i>	19.74 ± 0.08	ZTF	59182.7	7.2	<i>g</i>	19.63 ± 0.23	ZTF
59144.9	-19.3	<i>r</i>	19.58 ± 0.04	ZTF	59182.8	7.2	<i>i</i>	19.42 ± 0.19	ZTF
59145.9	-18.6	<i>g</i>	19.63 ± 0.06	ZTF	59184.5	8.4	<i>o</i>	19.39 ± 0.21	ATLAS
59146.5	-18.2	<i>c</i>	19.70 ± 0.11	ATLAS	59184.7	8.6	<i>g</i>	19.42 ± 0.20	ZTF
59147.5	-17.5	<i>o</i>	19.49 ± 0.12	ATLAS	59184.8	8.6	<i>r</i>	19.26 ± 0.13	ZTF
59148.4	-16.8	<i>o</i>	19.34 ± 0.25	ATLAS	59184.8	8.6	<i>i</i>	19.39 ± 0.14	ZTF
59149.8	-15.8	<i>r</i>	19.41 ± 0.12	ZTF	59185.8	9.3	<i>r</i>	19.17 ± 0.10	ZTF
59149.9	-15.8	<i>g</i>	19.50 ± 0.13	ZTF	59185.8	9.3	<i>g</i>	19.80 ± 0.19	ZTF
59150.8	-15.2	<i>r</i>	19.45 ± 0.09	ZTF	59186.4	9.8	<i>o</i>	19.42 ± 0.19	ATLAS
59150.9	-15.1	<i>g</i>	19.58 ± 0.14	ZTF	59187.5	10.5	<i>o</i>	19.38 ± 0.17	ATLAS
59151.8	-14.4	<i>r</i>	19.47 ± 0.10	ZTF	59187.7	10.7	<i>r</i>	19.63 ± 0.16	ZTF
59152.9	-13.7	<i>r</i>	19.24 ± 0.13	ZTF	59187.8	10.7	<i>i</i>	19.36 ± 0.15	ZTF
59155.8	-11.7	<i>r</i>	19.43 ± 0.11	ZTF	59187.8	10.7	<i>g</i>	19.72 ± 0.14	ZTF
59155.9	-11.6	<i>g</i>	19.33 ± 0.10	ZTF	59188.8	11.4	<i>r</i>	19.50 ± 0.07	ZTF
59156.5	-11.2	<i>o</i>	19.51 ± 0.19	ATLAS	59189.4	11.8	<i>o</i>	19.52 ± 0.14	ATLAS
59156.9	-10.9	<i>g</i>	19.39 ± 0.12	ZTF	59189.7	12.1	<i>r</i>	19.44 ± 0.05	ZTF
59157.5	-10.5	<i>o</i>	19.28 ± 0.17	ATLAS	59190.4	12.5	<i>o</i>	19.72 ± 0.15	ATLAS
59157.9	-10.2	<i>g</i>	19.36 ± 0.14	ZTF	59190.7	12.7	<i>r</i>	19.47 ± 0.06	ZTF
59157.9	-10.2	<i>r</i>	19.36 ± 0.14	ZTF	59191.0	12.9	<i>g</i>	19.67 ± 0.05	LT
59158.4	-9.8	<i>o</i>	19.46 ± 0.16	ATLAS	59191.0	12.9	<i>r</i>	19.50 ± 0.03	LT
59158.8	-9.6	<i>g</i>	19.41 ± 0.10	ZTF	59191.0	12.9	<i>i</i>	19.66 ± 0.04	LT
59158.9	-9.5	<i>r</i>	19.34 ± 0.09	ZTF	59191.0	12.9	<i>z</i>	19.77 ± 0.08	LT
59160.5	-8.4	<i>o</i>	19.38 ± 0.13	ATLAS	59191.4	13.2	<i>o</i>	19.53 ± 0.10	ATLAS
59161.5	-7.7	<i>o</i>	19.45 ± 0.13	ATLAS	59192.4	13.9	<i>o</i>	19.66 ± 0.11	ATLAS
59162.0	-7.3	<i>g</i>	19.29 ± 0.04	LT	59193.4	14.6	<i>c</i>	19.79 ± 0.13	ATLAS
59162.0	-7.3	<i>r</i>	19.34 ± 0.03	LT	59193.7	14.9	<i>g</i>	19.76 ± 0.08	ZTF
59162.0	-7.3	<i>i</i>	19.48 ± 0.04	LT	59193.8	14.9	<i>r</i>	19.53 ± 0.05	ZTF
59162.0	-7.3	<i>z</i>	19.59 ± 0.07	LT	59194.0	15.0	<i>i</i>	19.67 ± 0.23	LCO
59163.4	-6.3	<i>o</i>	19.52 ± 0.12	ATLAS	59194.4	15.3	<i>c</i>	19.75 ± 0.08	ATLAS
59164.8	-5.4	<i>r</i>	19.34 ± 0.08	ZTF	59194.7	15.5	<i>g</i>	19.89 ± 0.08	ZTF
59164.8	-5.4	<i>g</i>	19.42 ± 0.07	ZTF	59194.8	15.6	<i>r</i>	19.59 ± 0.08	ZTF
59165.8	-4.7	<i>g</i>	19.26 ± 0.04	ZTF	59195.4	16.0	<i>c</i>	19.87 ± 0.10	ATLAS
59165.9	-4.7	<i>r</i>	19.19 ± 0.04	ZTF	59195.7	16.3	<i>r</i>	19.67 ± 0.06	ZTF
59166.8	-4.0	<i>r</i>	19.37 ± 0.07	ZTF	59195.8	16.3	<i>g</i>	19.85 ± 0.09	ZTF
59166.9	-3.9	<i>g</i>	19.24 ± 0.05	ZTF	59197.7	17.6	<i>r</i>	19.69 ± 0.26	ZTF
59166.9	-3.9	<i>i</i>	19.46 ± 0.16	LCO	59198.4	18.1	<i>c</i>	20.18 ± 0.23	ATLAS
59167.4	-3.6	<i>o</i>	19.31 ± 0.08	ATLAS	59198.7	18.4	<i>r</i>	19.74 ± 0.08	ZTF
59167.8	-3.3	<i>g</i>	19.35 ± 0.14	ZTF	59198.7	18.4	<i>g</i>	20.17 ± 0.09	ZTF
59167.8	-3.3	<i>r</i>	19.35 ± 0.06	ZTF	59199.8	19.1	<i>r</i>	19.78 ± 0.10	ZTF
					59199.8	19.1	<i>g</i>	20.00 ± 0.14	ZTF
					59200.4	19.5	<i>c</i>	19.99 ± 0.12	ATLAS
					59200.7	19.7	<i>g</i>	20.10 ± 0.07	ZTF
					59200.7	19.8	<i>r</i>	19.58 ± 0.05	ZTF
					59200.8	19.8	<i>i</i>	19.68 ± 0.16	ZTF



Table A.1: continued.

MJD	Phase <sup>d</sup> (days)	Filter	Magnitude (mag)	Instrument
59202.7	21.1	<i>g</i>	20.44 ± 0.12	ZTF
59202.8	21.2	<i>r</i>	19.92 ± 0.09	ZTF
59203.7	21.8	<i>g</i>	20.52 ± 0.22	ZTF
59203.7	21.8	<i>r</i>	19.74 ± 0.13	ZTF
59204.3	22.3	<i>o</i>	19.78 ± 0.13	ATLAS
59204.8	22.6	<i>g</i>	20.16 ± 0.16	ZTF
59204.8	22.6	<i>r</i>	19.89 ± 0.14	ZTF
59205.4	23.0	<i>o</i>	19.80 ± 0.16	ATLAS
59206.3	23.6	<i>o</i>	19.82 ± 0.20	ATLAS
59208.3	25.0	<i>o</i>	19.84 ± 0.22	ATLAS
59210.8	26.8	<i>r</i>	20.26 ± 0.28	ZTF
59211.7	27.4	<i>i</i>	19.72 ± 0.23	ZTF
59212.4	27.9	<i>o</i>	20.02 ± 0.32	ATLAS
59216.4	30.7	<i>o</i>	20.23 ± 0.27	ATLAS
59216.7	30.9	<i>r</i>	20.51 ± 0.30	ZTF
59217.3	31.4	<i>o</i>	20.57 ± 0.29	ATLAS
59218.4	32.1	<i>o</i>	20.37 ± 0.30	ATLAS
59218.7	32.3	<i>r</i>	20.62 ± 0.23	ZTF
59219.3	32.8	<i>c</i>	20.65 ± 0.23	ATLAS
59219.7	33.0	<i>i</i>	20.25 ± 0.25	ZTF
59220.7	33.7	<i>r</i>	20.45 ± 0.18	ZTF
59222.4	34.9	<i>c</i>	21.09 ± 0.35	ATLAS
59224.3	36.3	<i>c</i>	20.81 ± 0.26	ATLAS
59227.7	38.6	<i>i</i>	20.63 ± 0.21	ZTF
59228.7	39.3	<i>r</i>	20.84 ± 0.26	ZTF
59230.6	40.7	<i>r</i>	20.66 ± 0.26	ZTF
59257.6	59.5	<i>r</i>	21.26 ± 0.30	ZTF
59969.7	557.6	<i>i</i>	20.95 ± 0.16	ZTF

**Notes.** The photometry is reported on the AB system and is not corrected for reddening. This table is available in machine readable form. Multiple exposures on any given night are averaged to give the values presented here.<sup>(a)</sup> Rest-frame relative to the g-band maximum (MJD 59172.5).

Table A.2: Photometric data of SN 2022xgc.

MJD	Phase <sup>d</sup> (days)	Filter	Magnitude (mag)	Instrument
59825.0	-58.7	<i>r</i>	21.13 ± 0.17	ZTF
59826.0	-57.9	<i>r</i>	21.13 ± 0.21	ZTF
59828.0	-56.4	<i>r</i>	21.35 ± 0.22	ZTF
59840.0	-47.2	<i>g</i>	20.93 ± 0.22	ZTF
59847.0	-41.9	<i>r</i>	20.93 ± 0.24	ZTF
59847.0	-41.9	<i>g</i>	20.84 ± 0.18	ZTF
59849.0	-40.4	<i>g</i>	20.50 ± 0.16	ZTF
59849.0	-40.4	<i>r</i>	20.50 ± 0.16	ZTF
59851.0	-38.9	<i>g</i>	20.32 ± 0.13	ZTF
59853.9	-36.6	<i>r</i>	20.25 ± 0.10	ZTF
59854.0	-36.6	<i>g</i>	20.27 ± 0.08	ZTF
59857.0	-34.3	<i>g</i>	19.98 ± 0.09	ZTF
59857.0	-34.3	<i>r</i>	19.87 ± 0.08	ZTF
59857.1	-34.2	<i>c</i>	19.93 ± 0.18	ATLAS
59859.3	-32.5	<i>o</i>	19.58 ± 0.24	ATLAS
59859.9	-32.0	<i>g</i>	19.68 ± 0.13	ZTF
59860.0	-32.0	<i>r</i>	19.82 ± 0.08	ZTF
59860.6	-31.5	<i>o</i>	19.51 ± 0.26	ATLAS
59862.0	-30.5	<i>g</i>	19.41 ± 0.16	ZTF
59862.0	-30.4	<i>r</i>	19.60 ± 0.11	ZTF
59862.6	-30.0	<i>o</i>	19.54 ± 0.23	ATLAS
59864.6	-28.5	<i>o</i>	19.54 ± 0.17	ATLAS
59865.0	-28.2	<i>g</i>	19.68 ± 0.16	ZTF
59865.0	-28.2	<i>r</i>	19.48 ± 0.10	ZTF
59868.0	-25.9	<i>g</i>	19.63 ± 0.13	ZTF
59868.6	-25.4	<i>o</i>	19.44 ± 0.16	ATLAS

Table A.2: continued.

MJD	Phase <sup>d</sup> (days)	Filter	Magnitude (mag)	Instrument
59870.6	-23.9	<i>o</i>	19.59 ± 0.12	ATLAS
59871.3	-23.3	<i>o</i>	19.39 ± 0.13	ATLAS
59871.9	-22.9	<i>r</i>	19.35 ± 0.10	ZTF
59872.0	-22.8	<i>g</i>	19.31 ± 0.08	ZTF
59872.6	-22.4	<i>o</i>	19.38 ± 0.12	ATLAS
59873.1	-22.0	<i>o</i>	19.17 ± 0.25	ATLAS
59874.9	-20.6	<i>g</i>	19.30 ± 0.05	ZTF
59875.0	-20.5	<i>r</i>	19.27 ± 0.05	ZTF
59876.6	-19.3	<i>c</i>	19.11 ± 0.08	ATLAS
59878.6	-17.8	<i>o</i>	19.19 ± 0.11	ATLAS
59878.9	-17.5	<i>g</i>	19.09 ± 0.05	ZTF
59879.4	-17.2	<i>c</i>	19.19 ± 0.07	ATLAS
59880.0	-16.7	<i>g</i>	19.06 ± 0.05	ZTF
59880.9	-16.0	<i>g</i>	19.03 ± 0.04	ZTF
59881.0	-16.0	<i>r</i>	19.08 ± 0.05	ZTF
59881.0	-15.9	<i>o</i>	18.90 ± 0.20	ATLAS
59882.0	-15.2	<i>g</i>	19.04 ± 0.04	ZTF
59882.6	-14.7	<i>o</i>	19.07 ± 0.07	ATLAS
59883.0	-14.4	<i>r</i>	18.86 ± 0.09	ZTF
59883.3	-14.2	<i>c</i>	19.15 ± 0.08	ATLAS
59883.9	-13.7	<i>r</i>	18.96 ± 0.05	ZTF
59884.0	-13.7	<i>g</i>	18.98 ± 0.04	ZTF
59884.6	-13.2	<i>c</i>	19.09 ± 0.07	ATLAS
59887.3	-11.2	<i>o</i>	19.33 ± 0.13	ATLAS
59887.9	-10.7	<i>g</i>	18.90 ± 0.07	ZTF
59888.0	-10.6	<i>r</i>	19.04 ± 0.07	ZTF
59889.9	-9.2	<i>g</i>	18.95 ± 0.09	ZTF
59889.9	-9.1	<i>r</i>	18.90 ± 0.06	ZTF
59890.6	-8.7	<i>o</i>	18.97 ± 0.09	ATLAS
59892.5	-7.1	<i>o</i>	19.12 ± 0.14	ATLAS
59893.4	-6.5	<i>o</i>	19.16 ± 0.17	ATLAS
59894.5	-5.7	<i>o</i>	18.78 ± 0.12	ATLAS
59896.8	-3.9	<i>r</i>	19.01 ± 0.15	ZTF
59896.9	-3.8	<i>g</i>	18.89 ± 0.12	ZTF
59897.5	-3.4	<i>o</i>	18.91 ± 0.14	ATLAS
59898.5	-2.6	<i>o</i>	19.05 ± 0.09	ATLAS
59899.3	-2.0	<i>o</i>	19.15 ± 0.13	ATLAS
59901.0	-0.7	<i>o</i>	18.99 ± 0.11	ATLAS
59901.3	-0.5	<i>r</i>	18.88 ± 0.06	SEDM
59902.0	0.1	<i>g</i>	18.82 ± 0.04	ZTF
59902.0	0.1	<i>r</i>	18.84 ± 0.04	ZTF
59903.3	1.1	<i>o</i>	18.99 ± 0.10	ATLAS
59903.9	1.5	<i>g</i>	18.93 ± 0.05	ZTF
59903.9	1.5	<i>r</i>	18.91 ± 0.04	ZTF
59905.9	3.1	<i>g</i>	18.80 ± 0.04	ZTF
59906.6	3.5	<i>c</i>	18.88 ± 0.05	ATLAS
59907.3	4.1	<i>o</i>	18.87 ± 0.07	ATLAS
59908.5	5.1	<i>o</i>	18.86 ± 0.07	ATLAS
59908.9	5.4	<i>g</i>	18.88 ± 0.04	ZTF
59908.9	5.4	<i>r</i>	18.91 ± 0.05	ZTF
59910.5	6.6	<i>c</i>	18.96 ± 0.08	ATLAS
59910.9	6.9	<i>r</i>	18.84 ± 0.04	ZTF
59910.9	6.9	<i>g</i>	18.93 ± 0.04	ZTF
59910.9	6.9	<i>g</i>	18.91 ± 0.04	ZTF
59911.1	7.0	<i>g</i>	18.91 ± 0.04	LT
59911.1	7.0	<i>i</i>	19.08 ± 0.05	LT
59911.1	7.0	<i>r</i>	18.92 ± 0.06	LT
59911.1	7.0	<i>z</i>	19.22 ± 0.09	LT
59911.3	7.2	<i>o</i>	18.86 ± 0.06	ATLAS
59912.9	8.4	<i>o</i>	18.72 ± 0.14	ATLAS
59913.9	9.2	<i>r</i>	19.00 ± 0.07	ZTF
59914.9	9.9	<i>r</i>	18.96 ± 0.04	ZTF
59915.2	10.2	<i>o</i>	18.92 ± 0.10	ATLAS
59916.6	11.3	<i>o</i>	19.11 ± 0.14	ATLAS
59919.2	13.2	<i>o</i>	18.96 ± 0.17	ATLAS
59920.9	14.5	<i>o</i>	18.75 ± 0.19	ATLAS

Table A.2: continued.

MJD	Phase <sup>d</sup> (days)	Filter	Magnitude (mag)	Instrument
59923.8	16.7	<i>r</i>	18.94 ± 0.11	ZTF
59927.3	19.4	<i>o</i>	19.04 ± 0.14	ATLAS
59928.6	20.4	<i>o</i>	19.25 ± 0.10	ATLAS
59928.8	20.6	<i>r</i>	18.97 ± 0.11	ZTF
59929.0	20.7	<i>g</i>	19.21 ± 0.06	LT
59929.0	20.7	<i>i</i>	19.23 ± 0.06	LT
59929.0	20.7	<i>r</i>	19.01 ± 0.05	LT
59929.0	20.7	<i>z</i>	19.43 ± 0.15	LT
59930.9	22.1	<i>r</i>	18.96 ± 0.04	ZTF
59931.2	22.4	<i>c</i>	19.21 ± 0.07	ATLAS
59932.9	23.7	<i>r</i>	19.10 ± 0.06	ZTF
59932.9	23.7	<i>g</i>	19.25 ± 0.06	ZTF
59934.2	24.7	<i>g</i>	19.31 ± 0.03	SEDM
59934.2	24.7	<i>r</i>	19.14 ± 0.04	SEDM
59934.2	24.7	<i>i</i>	19.19 ± 0.05	SEDM
59934.9	25.2	<i>r</i>	19.12 ± 0.06	ZTF
59934.9	25.2	<i>g</i>	19.40 ± 0.06	ZTF
59935.0	25.3	<i>g</i>	19.33 ± 0.08	LT
59935.0	25.3	<i>i</i>	19.28 ± 0.09	LT
59935.0	25.3	<i>r</i>	19.27 ± 0.09	LT
59935.0	25.3	<i>z</i>	19.21 ± 0.15	LT
59935.3	25.5	<i>c</i>	19.41 ± 0.11	ATLAS
59935.8	25.9	<i>g</i>	19.34 ± 0.06	ZTF
59936.8	26.7	<i>g</i>	19.40 ± 0.05	ZTF
59936.9	26.7	<i>r</i>	19.23 ± 0.06	ZTF
59939.2	28.5	<i>c</i>	19.31 ± 0.10	ATLAS
59940.8	29.7	<i>g</i>	19.54 ± 0.10	ZTF
59941.0	29.8	<i>o</i>	19.39 ± 0.12	ATLAS
59941.0	29.8	<i>o</i>	19.37 ± 0.12	ATLAS
59943.1	31.5	<i>g</i>	19.50 ± 0.09	LT
59943.1	31.5	<i>i</i>	19.32 ± 0.08	LT
59943.1	31.5	<i>r</i>	19.28 ± 0.08	LT
59943.1	31.5	<i>z</i>	19.35 ± 0.15	LT
59943.3	31.6	<i>c</i>	19.42 ± 0.10	ATLAS
59944.9	32.8	<i>o</i>	19.30 ± 0.14	ATLAS
59947.2	34.5	<i>o</i>	19.01 ± 0.18	ATLAS
59955.2	40.7	<i>o</i>	19.56 ± 0.17	ATLAS
59956.2	41.5	<i>r</i>	19.55 ± 0.03	SEDM
59956.2	41.5	<i>g</i>	20.06 ± 0.03	SEDM
59956.2	41.5	<i>i</i>	19.48 ± 0.04	SEDM
59957.0	42.0	<i>g</i>	20.02 ± 0.13	LT
59957.0	42.0	<i>i</i>	19.42 ± 0.09	LT
59957.0	42.0	<i>r</i>	19.55 ± 0.08	LT
59957.0	42.0	<i>z</i>	19.24 ± 0.13	LT
59957.0	42.0	<i>o</i>	19.18 ± 0.12	ATLAS
59957.4	42.4	<i>o</i>	19.36 ± 0.12	ATLAS
59959.2	43.7	<i>o</i>	19.44 ± 0.10	ATLAS
59963.2	46.8	<i>o</i>	19.64 ± 0.19	ATLAS
59964.5	47.8	<i>o</i>	19.67 ± 0.14	ATLAS
59965.0	48.1	<i>c</i>	20.23 ± 0.15	ATLAS
59967.9	50.4	<i>g</i>	20.67 ± 0.29	LT
59967.9	50.4	<i>i</i>	19.71 ± 0.10	LT
59967.9	50.4	<i>r</i>	19.91 ± 0.10	LT
59967.9	50.4	<i>z</i>	19.52 ± 0.14	LT
59968.4	50.7	<i>r</i>	19.84 ± 0.06	SEDM
59968.4	50.8	<i>g</i>	20.50 ± 0.09	SEDM
59968.4	50.8	<i>i</i>	19.60 ± 0.10	SEDM
59968.4	50.8	<i>o</i>	19.57 ± 0.22	ATLAS
59968.8	51.0	<i>g</i>	20.56 ± 0.20	ZTF
59968.9	51.1	<i>c</i>	20.22 ± 0.17	ATLAS
59969.8	51.8	<i>g</i>	20.32 ± 0.16	ZTF
59971.2	52.9	<i>o</i>	19.84 ± 0.14	ATLAS
59971.8	53.3	<i>r</i>	19.74 ± 0.11	ZTF
59971.8	53.4	<i>r</i>	19.78 ± 0.11	ZTF
59975.2	55.9	<i>o</i>	19.30 ± 0.17	ATLAS

Table A.2: continued.

MJD	Phase <sup>d</sup> (days)	Filter	Magnitude (mag)	Instrument
59984.9	63.4	<i>o</i>	19.74 ± 0.20	ATLAS
59987.7	65.5	<i>r</i>	19.80 ± 0.10	ZTF
59987.9	65.6	<i>o</i>	19.99 ± 0.22	ATLAS
59988.9	66.4	<i>o</i>	20.27 ± 0.24	ATLAS
59988.9	66.4	<i>g</i>	20.93 ± 0.13	LT
59988.9	66.4	<i>i</i>	19.97 ± 0.07	LT
59988.9	66.4	<i>r</i>	20.19 ± 0.09	LT
59988.9	66.4	<i>z</i>	20.00 ± 0.12	LT
59989.1	66.6	<i>c</i>	20.36 ± 0.27	ATLAS
59994.1	70.4	<i>c</i>	20.42 ± 0.24	ATLAS
59996.9	72.5	<i>o</i>	19.93 ± 0.16	ATLAS
59999.9	74.8	<i>g</i>	21.02 ± 0.25	LT
59999.9	74.8	<i>i</i>	20.12 ± 0.09	LT
59999.9	74.8	<i>r</i>	20.31 ± 0.13	LT
59999.9	74.8	<i>z</i>	19.92 ± 0.15	LT
60000.3	75.1	<i>o</i>	20.12 ± 0.26	ATLAS
60002.1	76.5	<i>o</i>	19.99 ± 0.21	ATLAS
60012.0	84.0	<i>r</i>	20.69 ± 0.03	NOT
60012.0	84.0	<i>g</i>	21.55 ± 0.08	NOT
60012.2	84.2	<i>r</i>	20.75 ± 0.21	SEDM
60012.2	84.2	<i>i</i>	20.45 ± 0.23	SEDM
60013.7	85.3	<i>r</i>	20.86 ± 0.31	ZTF
60020.8	90.7	<i>r</i>	20.65 ± 0.19	ZTF
60020.8	90.7	<i>c</i>	20.50 ± 0.25	ATLAS
60021.0	90.9	<i>o</i>	20.16 ± 0.27	ATLAS
60030.7	98.3	<i>r</i>	20.53 ± 0.17	ZTF
60045.7	109.7	<i>g</i>	21.40 ± 0.29	ZTF
60045.7	109.8	<i>r</i>	20.70 ± 0.19	ZTF
60065.7	125.0	<i>r</i>	19.97 ± 0.29	ZTF

**Notes.** The photometry is reported on the AB system and is not corrected for reddening. This table is available in machine readable form. Multiple exposures on any given night are averaged to give the values presented here.<sup>(d)</sup> Rest-frame relative to the g-band maximum (MJD 59901.9).

## Appendix B: Spectroscopic data

Table B.1: SN 2020xga spectroscopic observations.

UT date	MJD (days)	Phase <sup>a</sup> (days)	Telescope + Instrument	Exposure (s)	Disperser	Wavelength range (Å)
20201106	59159.6	-9	NTT + EFOSC2	1500	Gr#13	3650 – 9250
20201107	59160.6	-8.3	VLT + X-shooter	3600	–	3000 – 24800
20201116	59169.8	-1.9	NTT + EFOSC2	2700	Gr#11 + Gr#16	3345 – 9995
20201117	59170.7	-1.3	NTT + EFOSC2	2700	Gr#11	3345 – 7470
20201207	59190.6	+12.7	NTT + EFOSC2	5400	Gr#13	3650 – 9250
20201230	59213.6	+28.8	NTT + EFOSC2	5400	Gr#13	3650 – 9250
20210107	59221.2	+34.1	P200 + DBSP	3600	600/316	3500 – 10000
20210110	59224.6	+36.4	VLT + X-shooter	4800	–	3000 – 24800
20210114	59228.6	+39.3	VLT + X-shooter	4800	–	3000 – 24800

Notes. <sup>(a)</sup> Rest-frame relative to the *g*-band maximum (MJD 59172.5).

Table B.2: SN 2022xgc spectroscopic observations.

UT date	MJD (days)	Phase <sup>a</sup>	Telescope + Instrument	Exposure (s)	Disperser	Wavelength range (Å)
20221113	59896.0	-4.5	NOT + ALFOSC	3344	Gr#4	3900 – 9600
20221114	59897.8	-3.7	P60 + SEDm	2250	–	3950 – 9200
20221118	59901.3	-0.7	P60 + SEDm	2250	–	3950 – 9200
20221122	59905.0	+2.4	Lick + KAST	3600	600/4310 + 300/7500	3500 – 10500
20221201	59914.8	+9.8	NTT + EFOSC2	900	Gr#13	3650 – 9250
20221214	59927.0	+19.2	NOT + ALFOSC	3600	Gr#4	3900 – 9600
20221207	59930.6	+21.9	VLT + X-shooter	3600	–	3000 – 24800
20221222	59935.7	+25.8	NTT + EFOSC2	2700	Gr#13	3650 – 9250
20230113	59957.8	+42.6	NTT + EFOSC2	2700	Gr#11 + Gr#16	3345 – 9995
20230117	59961.0	+45.1	NOT + ALFOSC	4000	Gr#4	3900 – 9600
20230129	59973.6	+54.7	NTT + EFOSC2	2700	Gr#11	3345 – 7470
20230209	59987.6	+61.3	NTT + EFOSC2	2700	Gr#11 + Gr#16	3345 – 9995
20230212	59987.6	+65.4	VLT + X-shooter	4800	–	3000 – 24800
20230221	59996.7	+72.3	NTT + EFOSC2	2700	Gr#11 + Gr#16	3345 – 9995
20230319	60022.5	+92.1	VLT + X-shooter	3600	–	3000 – 24800

Notes. <sup>(a)</sup> Rest-frame relative to the rest-frame *g*-band maximum (MJD 59901.9).



### Appendix C: Polarimetry data

The log of the polarimetry obtained on SN 2022xgc using ALFOSC on the NOT discussed in Section 2.5 is presented in Table C.1. The results discussed in Sections 2.5 and 3.5 are given in Table C.2.

Table C.1: Observations log of the imaging polarimetry observations. N.A. means Not Available.

UT Time	Object	Exp. Time [s]	Filter	Seeing [ $''$ ]
2022-12-15 00:00:24	SN 2022xgc	$2 \times (4 \times 420)$	V	N.A.
2022-12-15 01:03:00	SN 2022xgc	$2 \times (4 \times 420)$	R	N.A.
2022-12-14 22:03:00	HD 14069	$2 \times (4 \times 1)$	V	N.A.
2022-12-14 22:05:48	HD 14069	$2 \times (4 \times 1)$	R	N.A.
2022-12-14 22:10:11	HD 251204	$4 \times (4 \times 3)$	V	N.A.
2022-12-14 22:12:44	HD 251204	$4 \times (4 \times 3)$	R	N.A.
2023-01-18 00:57:12	SN 2022xgc	$4 \times (4 \times 200)$	V	1.1
2023-01-18 00:00:02	SN 2022xgc	$4 \times (4 \times 200)$	R	1.0
2023-01-17 19:43:50	HD 14069	$2 \times (4 \times 2)$	V	1.2
2023-01-17 19:46:05	HD 14069	$2 \times (4 \times 2)$	R	1.2
2023-01-17 19:49:44	BD+59 389	$2 \times (4 \times 1.2)$	V	1.2
2023-01-17 19:51:41	BD+59 389	$2 \times (4 \times 1.5)$	R	1.2

Table C.2: Polarimetry results on SN 2022xgc obtained in the R-band and V-band Bessel filters. <sup>(a)</sup>: Stokes parameters,  $\overline{Q}$  and  $\overline{U}$ , directly obtained from the ALFOSC data frames Extraordinary and Ordinary images without applying any further corrections. <sup>(b)</sup>: instrumental polarization corrected. <sup>(c)</sup>: instrumental polarization corrected and polarization angle corrected. <sup>(d)</sup>: instrumental polarization corrected, polarization angle corrected and bias corrected.

Date	Source	filter	$\overline{Q}^{(a)}$	$\overline{U}^{(a)}$	$P[\%]^{(a)}$	$P[\%]^{(b,c)}$	$\theta[^\circ]^{(c)}$	$P_{\text{deb}}[\%]^{(d)}$
2022-12-14	HD 14069	R	0.06	0.12	<b><math>0.13 \pm 0.04</math></b>	–	–	–
2022-12-14	HD 251204	R	-2.53	4.10	$4.82 \pm 0.03$	<b><math>4.75 \pm 0.05</math></b>	–	–
2022-12-14	SN 2022xgc	R	0.11	-0.07	$0.13 \pm 0.10$	$0.19 \pm 0.11$	$46.85 \pm 16.75$	<b><math>0.13 \pm 0.11</math></b>
2022-12-14	HD 14069	V	0.02	0.16	<b><math>0.16 \pm 0.06</math></b>	–	–	–
2022-12-14	HD 251204	V	-3.12	3.89	$4.99 \pm 0.05$	<b><math>4.87 \pm 0.08</math></b>	–	–
2022-12-14	SN 2022xgc	V	0.13	-0.03	$0.14 \pm 0.12$	$0.22 \pm 0.14$	$53.05 \pm 17.63$	<b><math>0.13 \pm 0.14</math></b>
2023-01-17	HD 14069	R	0.09	0.06	<b><math>0.11 \pm 0.05</math></b>	–	–	–
2023-01-17	BD+59 389	R	6.39	1.40	$6.55 \pm 0.04$	<b><math>6.44 \pm 0.06</math></b>	–	–
2023-01-17	SN 2022xgc	R	0.11	0.16	$0.19 \pm 0.10$	$0.10 \pm 0.11$	$132.89 \pm 33.47$	<b><math>0.10 \pm 0.11</math></b>
2023-01-17	HD 14069	V	-0.07	0.16	<b><math>0.17 \pm 0.04</math></b>	–	–	–
2023-01-17	BD+59 389	V	6.23	2.22	$6.62 \pm 0.08$	<b><math>6.63 \pm 0.09</math></b>	–	–
2023-01-17	SN 2022xgc	V	0.34	0.34	$0.48 \pm 0.18$	$0.44 \pm 0.18$	$100.92 \pm 11.95$	<b><math>0.37 \pm 0.18</math></b>

## Appendix D: Redback results

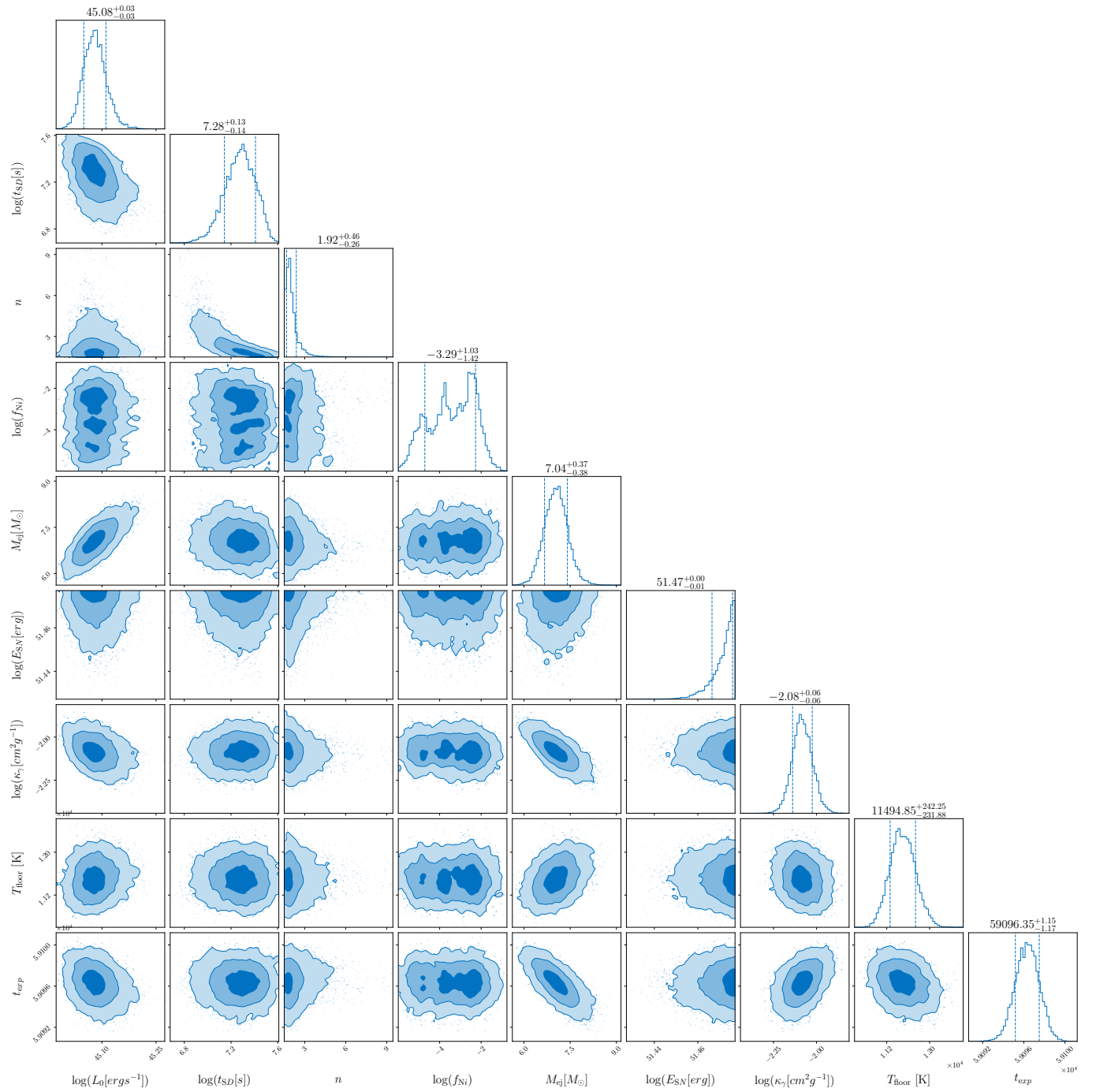


Fig. D.1: 1D and 2D posterior distributions of the general magnetar-driven supernova model parameters from REDBACK for SN 2020xga. Median and  $1\sigma$  of the best fit values are marked and labeled.

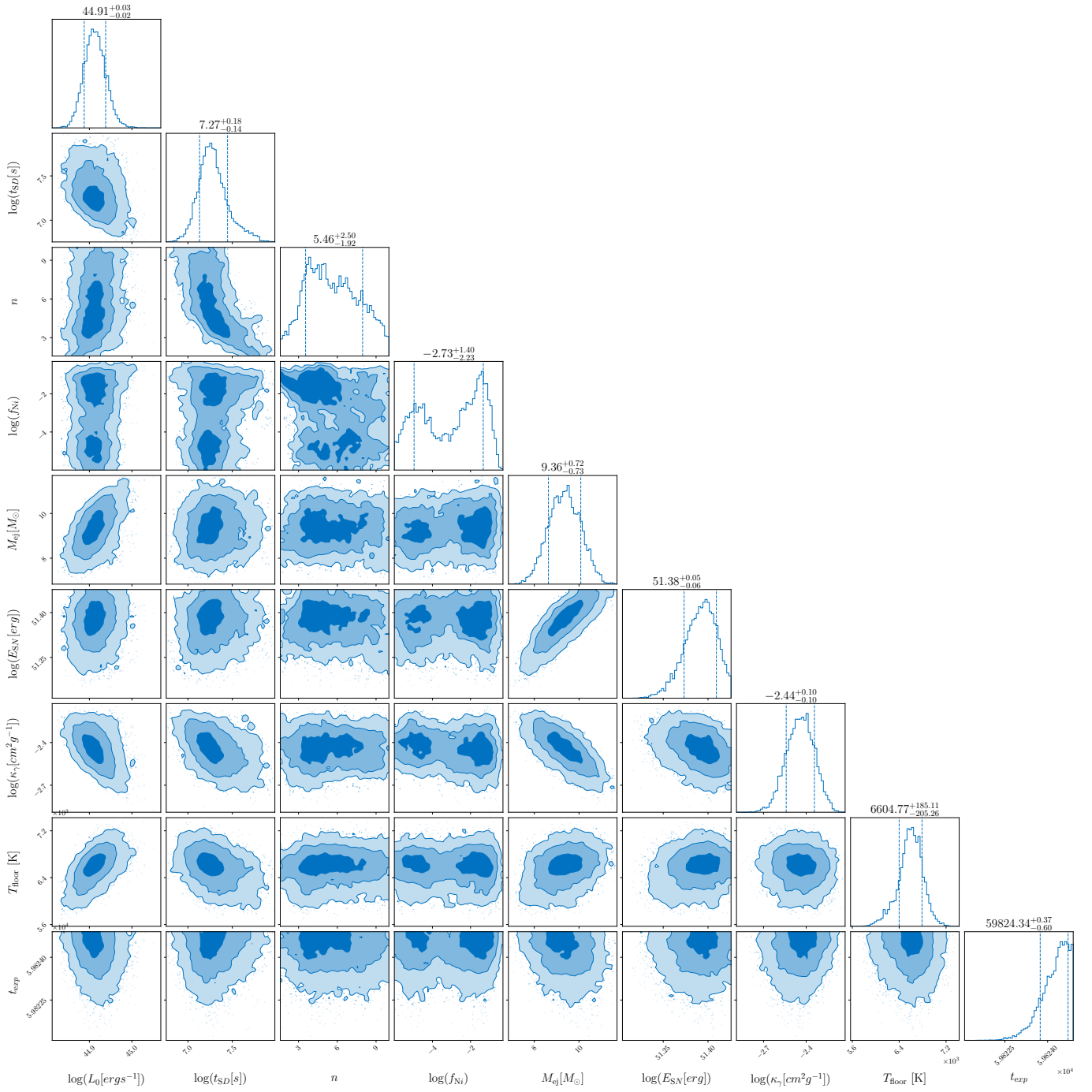


Fig. D.2: 1D and 2D posterior distributions of the general magnetar-driven supernova model parameters from REDBACK for SN 2022xgc. Median and  $1\sigma$  of the best fit values are marked and labeled.



## Appendix E: SYN++ results

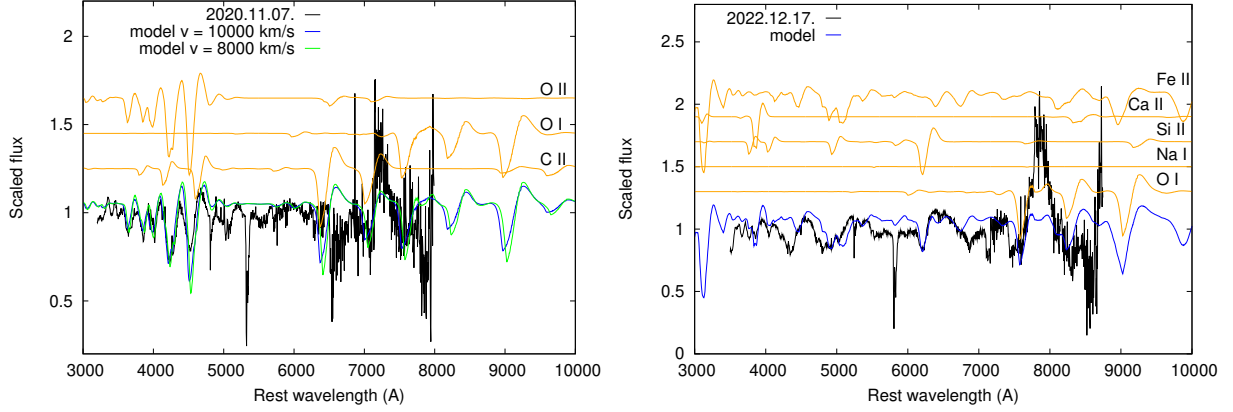


Fig. E.1: The SYN++ modeling of one of the spectra of SN 2020xga (left) and SN 2022xgc (right). The observed spectra (black lines) are corrected for interstellar reddening and redshift, and continuum-normalized for clarification. The best-fit model obtained using SYN++ is shown with blue and green colors, while the contribution of the single ions to the model are plotted with orange, and shifted vertically.

Table E.1: Best-fit parameter values of the SYN++ modeling of the spectra of SN 2020xga and SN 2022xgc. The fitted parameters are the following: the velocity at the photosphere ( $v_{\text{phot}}$  [ $10^3 \text{ km s}^{-1}$ ]), the photospheric temperature ( $T_{\text{phot}}$  [1000 K]), the optical depth of each ion ( $\log \tau$  [-]), the inner velocity of the line forming region ( $v_{\text{min}}$  [ $10^3 \text{ km s}^{-1}$ ]), the outer velocity of the line forming region ( $v_{\text{max}}$  [ $10^3 \text{ km s}^{-1}$ ]), the scale height of the optical depth (aux [ $10^3 \text{ km s}^{-1}$ ]), and the excitation temperature of each ion ( $T_{\text{exc}}$  [1000 K]).

Ions	C II	O I	O II	Na I	Si II	Ca II	Fe II
SN 2020xga (2020.11.07) $v_{\text{phot}} = 8.0$ ; $T_{\text{phot}}=14.0$							
$\log \tau$	-0.4	0.1	-1.2				
$v_{\text{min}}$	8.0	8.0	8.0				
$v_{\text{max}}$	30.0	30.0	30.0				
aux	1.0	1.0	1.0				
$T_{\text{exc}}$	14.0	14.0	14.0				
SN 2022xgc (2022.12.17) $v_{\text{phot}} = 8.0$ ; $T_{\text{phot}}=13.0$							
$\log \tau$		0.2		3.2	0.1	0.2	-0.1
$v_{\text{min}}$		8.0		20.0	8.0	8.0	8.0
$v_{\text{max}}$		30.0		30.0	30.0	30.0	30.0
aux		1.0		1.0	1.0	1.0	1.0
$T_{\text{exc}}$		13.0		13.0	13.0	13.0	13.0